RESPONSE OF ELECTRIFIED MICRO-JETS TO ELECTROHYDRODYNAMIC PERTURBATIONS

by

WEIWEI YANG
B.S. University of Science and Technology of China, Hefei 2009
MS. University of Central Florida, Orlando 2012

A dissertation submitted in partial fulfillment of the requirements
for the degree of Doctor of Philosophy
in the Department of Mechanical and Aerospace Engineering
in the College of Engineering and Computer Science
at the University of Central Florida
Orlando, Florida

Summer Term
2014

Major Professor: Weiwei Deng

© 2014 Weiwei Yang

ABSTRACT

The breakup of liquid jets is ubiquitous with rich underpinning physics and widespread applications. The natural breakup of liquid jets originates from small ambient perturbations, which can grow exponentially until the amplitude as large as the jet radius is reached. For unelectrified inviscid jets, surface energy analysis shows that only the axisymmetric perturbation is possibly unstable, and this mode is referred as varicose instability. For electrified jets, the presence of surface charge enables additional unstable modes, among which the most common one is the whipping (or kink) instability that bends and stretches the charged jet that is responsible for the phenomena of electrospinning. A closer examination of the two instabilities suggests that due to mass conservation, the uneven jet stretching from whipping may translate into radial perturbations and trigger varicose instabilities. Although the varicose and whipping instabilities of electrified micro-jets have both been extensively studied separately, there is little attention paid to the combined effect of these two, which may lead to new jet breakup phenomena. This dissertation investigates the dynamic response of electrified jets under transverse electrohydrodynamic (EHD) perturbations which were introduced by exciters driven by alternating voltage of sweeping frequency. Three different jetting mechanisms are used to generate jets with various ranges of jet diameters: ~150 micrometer inertial jets from liquid pressurized through a small orifice, ~50 micrometer flow focused jets, and ~20 micrometer electrified Taylor-cone jets. The transverse perturbations enable systematic triggering of varicose and whipping

instabilities, and consequently a wide range of remarkable phenomena emerge. For inertial jets with zero or low charge levels, only varicose instability is observable due to suppressed whipping instability. At modest charge levels, inertia jets can respond to the fundamental perturbation frequency as well as the second harmonic of the perturbation frequency. Highly charged jets such as fine jets generated from Taylor cones exhibit distinct behavior for different perturbation wavenumber x. Typical behavior include: whipping jets with superimposed varicose instability at small x, jet bifurcation from crossover of whipping and varicose instabilities at $x \sim 0.5$, Coulombic fission owing to the surge of surface charge density as the slender liquid segments recover spherical shapes at $x \sim 0.7$, and simple varicose mode near wave numbers of unity. The phenomena observed in this work may be explained by a linear model and rationalized by the phase diagram in the space of wave number and dimensionless charge levels. The experimental apparatus used in this dissertation is simple, non-intrusive, and scalable to a linear array of jets. The rich phenomena combined with the versatile apparatus may spawn new research directions such as regulated electrospinning, generating strictly monodisperse micro/nano droplets, and manufacturing of non-spherical particles from drying droplets that undergo controlled Coulombic fissions.

To my family Yan and Kevin

ACKNOWLEDGMENTS

First of all I want to thank my advisor Dr. Weiwei Deng, who trusted and accepted me as his first PHD student during a difficult period of my life. I learned from him not only specific skills, but also principles in research. For example, one thing I learned from him is that we must have "good taste", which means we should set a high standard for our research. Another example is that we should be persistent and find ways to finish tasks we initiated, no matter how challenging they are. These skills and principles will continue to influence me in the future.

Second I want to thank my parents, who gave their best to raise me up and provided me a good environment. No matter what decisions I made, they always gave me their unconditional support. I felt really lucky to have them as my parents and I wished I could have visited them more often.

Third I want to thank Professor Louis Chow, Profess Ranganathan Kumar and Professor Jiyu Fang for serving the committee. I also want to thank all my lab mates for their help to make this dissertation possible, especially Hongxu Duan and Kappy Krudger for their experimental support.

Last but not least, I want to thank Yan Wei, who is my loving wife, my best friend, my inspiring colleague, and the mother of our baby Kevin. Yan and Kevin are true blessings in my life.

TABLE OF CONTENTS

LIST OF FIGURES x

CHAPTER 1. INTRODUCTION 1

1.1 Droplets for advanced manufacturing 3

1.1.1 Thin film fabrication 3

1.1.2 Printing of fine features 4

1.1.3 Application of monodisperse droplets 6

1.2 Liquid jets: a prelude for droplet generation 8

1.2.1 Inertial jet 8

1.2.2 Flow focused jet 9

1.2.3 Taylor cone jet 10

1.3 Electrohydrodynamic (EHD) and other jet perturbation approaches 12

1.3.1 Acoustic perturbation 13

1.3.2 Mechanical perturbation 14

1.3.3 EHD perturbation 15

1.4 Dissertation overview 16

CHAPTER 2. THEORIES ON LIQUID JET INSTABILIT 18

2.1 Temporal Theory of the Instability of a Liquid Jet 18

2.2 Spatial Theory and Nonlinear Effects 23

2.3 Dispersion Relationship for a Charged Inviscid Jet 27

2.4 Dispersion Relationship for uncharged Viscous Jet 29

2.5 Dispersion Relationship for a Charged Viscous Jet in Varicose Mode.....31

2.6 Breakup Length 33

CHAPTER 3. EHD PERTURBATION ON AN INERTIA JET 36

3.1 EHD excitation on uncharged liquid jet with capacitor configuration.....36

3.1.1 Generation of an inertia jet.....36

3.1.2 Experimental Setup 39

3.1.3 Factors affecting perturbation magnitude.....41

3.1.4 Results and discussion 43

3.1.5 Scale-up of the perturbation 48

3.2 EHD excitation on charged liquid jet with in-plane configuration 49

3.2.1 Experimental Setup 49

3.2.2 Theoretical Development 52

3.2.3 Results and discussion 60

CHAPTER 4. EHD PERTURBATION ON A FLOW FOCUSED JET.....69

4.1 Generation of a flow focused jet 69

4.2 Experimental setup of EHD perturbation on a scalable flow focused jet.....72

4.3 Theoretical development 73

4.3.1 Flow field inside the chamber 73

4.3.2 Operation regions 78

4.4 Results and discussion 83

CHAPTER 5. EHD PERTURBATION ON TAYLOR CONE JET 87

5.1 Fundamentals of electrospray 87

5.2 Experimental Setup 91

5.3 Results and discussion 92

5.3.1 Basic phenomenology 92

5.3.2 Jet response under sweeping frequencies 94

5.3.3 Effects of surface charge level 96

5.3.4 Effects of viscosity 100

CHAPTER 6. CONCLUSIONS 102

APPENDIX A: RAYLEIGH DISPERSION RELATIONSHIP (ADAPTED FROM P.G.DRAZIN AND W.H.REID:*HYDRODYNAMIC STABILITY*) 104

APPENDIX B: ELECTRIC FIELD BETWEEN TWO HORIZONTAL BLADES WITH EDGE FACING EACH OTHER 108

REFERENCES 115

LIST OF FIGURES

Figure 1. Application of monodisperse droplets: (a)Lasing droplets (d~30 μm) (Richard Chang,1986) (b) SEM images of monodisperse PLGA microparticles (Q. Xu, 2009)..... 6

Figure 2. Flow focusing jet generator (Ganan-Calvo, 1997) (Left: illustration of device setup; Right: Image of FF in operation).....10

Figure 3. Electrospray setup (book chapter, Gomez and Deng, 2011).....11

Figure 4: Acoustic perturbation on the liquid jet (Donnelly and Glaberson, 1965).....13

Figure 5. Piezoelectric aerosol generator (TSI Model 3450).....14

Figure 6. EHD perturbation (Gonzalez and Garcia, 2009).....15

Figure 7. (a) initial state of the jet (b) the physical shape of instability corresponding to m=0 (c) the physical shape of instability corresponding to m=1. 18

Figure 8: Rayleigh dispersion relationship.....21

Figure 9: Plot of dispersion relation (2.8) for m=0 (a) and m=1(b) at different charge levels.....28

Figure 10: Dispersion relationship for a viscous jet at different Reynolds number for the varicose mode. 30

Figure 11: Dispersion curve for Γ=1 and different oh values.....32

Figure 12: Dispersion curve for oh=0.05 and different Γ values. 33

Figure 13. Experimental setup of the uncharged jet under electro-hydrodynamic perturbation 40

Figure 14. The breakup of ethanol jet at different driving frequencies. The gap b is 43

Figure 15. Jet breakup locations as a function of $V_{p\text{-}p}$ at fixed frequency. Jet radius is 75 μm. f=1.1kHz, v_j=1.49m/s 45

Figure 16. The linear relationship between the magnitude of initial perturbation and the $V_{p\text{-}p}{}^2$ of the driving signal. 46

Figure 17: Monodisperse and quasi monodisperse droplet islands.....48

Figure 18. Multiple jets that experience transverse perturbation by the same capacitor. (a) The manifold of four nozzles (nozzle spacing: 500 μm; nozzle OD=200μm, ID=100μm); (b) breakup after the transverse perturbation is applied. Note the absence of satellite droplets in all four jet breakups. 49

Figure 19. Experimental setup for electrified jet under electrohydrodynamic perturbation 50

Figure 20: Surface charge density vs. jet voltage.....54

Figure 21: (a)Surface charge density vs. EHD frequency (Q=120ml/hr, V_{jet}=512V, $V_{p\text{-}p}$=500V, R=75μm) and (b) Surface charge density vs. $V_{p\text{-}p}$ (V_{jet}=300V, Q=120ml/hr, f=2400Hz, R=75μm) 54

Figure 22: (a) Surface charge density vs. blade-jet separation ($V_{p\text{-}p}$=538V, V_{jet}=464V, Q=120ml/hr, R=75μm) and (b) surface charge density vs. jet voltage for two different liquids. (Q=120ml/hr).....55

Figure 23. Measurement of the jet initial whipping magnitude δx.....57

Figure 24: Initial perturbation magnitude vs. perturbation frequency (Vpp=300V, σ =4.37x10-5C/m2, R=75μm, vj=1.52m/s, a=1494μm, ρ=800kg/m3). 60

Figure 25: Jet breakup length difference when changing V_{pp}: (a) V_{pp}=204V, (b) V_{pp}=660V; Changing blade separation (c) 3.90mm (d) 0.48mm and changing blade height (e) blade at the beginning of the jet (f) blade at the midway of the jet. Q=120ml/hr, f=2320Hz, V_{jet}=500V, V_{pp}=744V.....61

Figure 26: Frequency response of charged jet at different charge levels and perturbation wave numbers. The dimensionless charge level Γ is defined as the ratio of electric stress to surface tension of the jet, i.e. $\Gamma=\sigma^2 R/\varepsilon_0\gamma$, with ε_0 being vacuum permittivity.....63

Figure 27: breaking up details.(Upper row: Rayleigh mode, interval between images: 62.5 μs. Lower row: Shearing mode, interval between images: 61.68 μs.) 67

Figure 28: (a) Schematic of the flowing focusing device. (b) Jet formation inside the chamber (c) Overall view of jet formation.....70

Figure 29: Experimental setup for flow focused jet EHD perturbation.....72

Figure 30. The simplified flow problem in flow focusing device.....74

Figure 31: Equal pressure lines inside the chamber, values are non-dimensionalized by $\rho Q^2/2a^2\pi^2$ 75

Figure 32: Streamlines, the stream function values are nondimensionalized by Q/π 76

Figure 33: Pressure drop along the y axis.....77

Figure 34: Operation regions for flow focusing device using water as working fluid. (Si, 2009). (a) Operation region in Q_l - Δp_g plane. (b) cone-shaking mode in region (I), (c) cone-adhering mode in region (II), (d) helical-jetting mode in region (III), (e) coexisting-jetting mode in region(IV), (f) Axisymmetric jetting mode in region (V), (g) dripping

mode in region (VI), (h) dripping faucet, close to dripping mode, only observed occasionally.....79

Figure 35: Generation of a flow focused jet through a slit.....83

Figure 36: Jet size experimental vs. theoretical (Equation (4.1)) 84

Figure 37: Jet breakup before(a) and after(b)introduction of EHD perturbation.....85

Figure 38: Typical electrospray (ES) setup (Gomez and Deng, 2008) 88

Figure 39. Taylor cone jet under EHD perturbation. The jet radius is 10 μm. 91

Figure 40: Jet swing images from a half cycle at low frequency (250 Hz).....92

Figure 41. The effect of electrode configuration on the initial perturbation magnitude. All perturbation frequency is 80kHz, corresponding to a wavelength 125 μm. (a) gap 2a=125 μm; (b) gap 2a=79 μm; (c) same gap with case (b), but the blades are 300 μm further away from the Taylor cone.....93

Figure 42: Typical response of the electrified jet to external EHD perturbation introduced by the AC electric field between the narrow gap of two in-plane blade electrodes.....94

Figure 43: Representative images for x-Γ diagram (a) varicose mode, Q=16 ml/h, E_d=2 kV/cm, x=0.98; (b) whipping assisted bifurcation, Q=12 ml/h, E_d=2.5 kV/cm, x=0.69, Γ=1.32; (c) overcharged whipping assisted bifurcation, Q=16 ml/h, E_d=1.25 kV/cm, x=0.69, Γ=1.74; (d) overcharged varicose mode, Q=12 ml/h, E_d=1 kV/cm, x=1.21, Γ=1.63; (e) varicose assisted bifurcation, Q=14 ml/h, E_d=2.5kV/cm, x=0.45, Γ=0.56 .97

Figure 44: Jet response phenomenon mapped in the x-Γ diagram. Scattered data points are experimental data.....99

Figure 45: Perturbation response of more viscous liquid (75% ethanol + 25% glycerol, 8ml/h). 100

Figure 46: 2D problem of electric field for the experiment setup 109

Figure 47: 2D problem of electric field after non-dimensionalizing 110

Figure 48: Conformal mapping of z domain (a) to w domain (b), where the geometry has been transformed to a strip. 111

Figure 49: COMSOL simulation for the dimensionless electric potential for a problem shown in Figure 48(a) 112

Figure 50: Analytical (top) and numerical (bottom) solutions for Ex at x=0 and x=1/2 (for problem shown in Figure 48(a)) 113

CHAPTER 1. INTRODUCTION

Liquid droplets are ubiquitous in our daily lives, naturally or artificially generated by human. They are widely used in many industry processes such as fuel injection, spray drying and spray painting. Small droplets at the range of micrometer to nanometer size can be used as building blocks to manufacture complicated functional materials. Deposition of micro/nano droplets can form 2D films (Jaworek, 2007), 1D wires (Duan et al., 2013) or simply be dried to form nano particles (Jaworek, 2007). Those process examples were conducted at ambient pressure, therefore micro/nano droplets opens the door of low cost additive manufacturing of high-value added thin film devices, which conventionally requires expensive film deposition processes such as chemical vapor deposition (CVD) or physical vapor deposition (PVD) in vacuum. Such droplet deposition techniques have already found emerging applications in solar cells (Zhao, 2012), LED displays (Shimoda, 2003) and lithium-ion batteries(Yin, 2011). Due to their large surface area to mass ratio, small droplets also have found various application in areas such as combustion (Kyritsis et al., 2004), microelectronics device cooling (Deng and Gomez, 2011) and air purification (Tepper, 2007). Typically, the droplets used in industry (such as the ones generated by a pneumatic spray device) are polydisperse. Monodisperse droplets have attracted increasing attention and found applications in areas such as polymer electronic device printing (de Gans, 2004), lasing droplets (Qian,

1986), drug delivery(Xu, 2009), additive manufacturing (Jaworek, 2007) and aerosol instrumentation calibration (Berglund, 1973) due to its narrow size distribution. In manufacturing, droplet size and size distribution (monodispersity) are usually two key factors that decide the quality of the final product. For example, in ink jet printing, the finest line width and its variation are mainly determined by these two factors. In film deposition process, the film thickness and roughness also depends heavily on the droplet size and size distribution.

Monodisperse droplets are commonly generated through the breakup of liquid jets. A liquid jet can automatically breakup into droplets due to the development of unstable surface perturbation from the environment. Droplets produced this way generally are not strictly monodisperse due to the random environmental perturbations and the generation of satellite droplets between primary ones. One typical way to generate monodisperse droplets is to give liquid jet a prescribed perturbation with adequate frequency so that the perturbation outgrows the natural perturbation and dominates the jet break up process. The purpose of this dissertation is to use electrohydrodynamic (EHD) perturbation to control the jet break up process, thus generate droplets with controlled size and size distribution. We aim to reveal the physics behind EHD perturbation on jets generated by different methods with size from hundreds of microns down to a few microns. Perturbations can be introduced by several different ways, including mechanical, acoustic, and EHD stress. This dissertation uses EHD perturbation due to several advantages: first, EHD perturbation is not in contact with working liquids hence contamination will be eliminated; second, the magnitude and

waveforms of perturbation can be conveniently prescribed and controlled; third, the EHD perturbation may induce additional surface charge of the jet to enhance the jet response. In this chapter, we first review the applications of droplets in advanced manufacturing, then we review the methods for generating a liquid jet and the different jet perturbation methods, finally we provide an overview of this dissertation.

1.1 Droplets for advanced manufacturing

1.1.1 Thin film fabrication

The quality of thin film deposited on the substrate strongly depends on the droplet size and size distribution. Smaller droplet size with narrow distribution will reduce the voids and flaws, and a more uniform film is expected. Also, intuitively, smaller droplets or particles will lead to thinner films.

One actively researched topic of thin film deposition is the fabrication of inorganic and organic solar cells. CdS (Su et al, 2000a), CdSe (Su et al, 2000b) have been deposited for making inorganic solar cells. For organic solar cells, both Dye Sensitized Solar Cells (DSSC) (Fujimoto, 2006 and Zhang, 2009) and Polymer Solar Cells (PSC) (Kim, 2010) have been made using electrospray film deposition method. Most works on droplet deposition fabricated DSSCs reported so far show higher performance compared to cells fabricated by conventional methods, such as screen-printing or doctor-blading (Fujimoto, 2006 and Zhang, 2009). The improved performances of droplet deposition fabricated DSSCs were mostly attributed to the

special morphology of the deposited TiO_2 electrode, which shows semi-self-assembled structure. Another type of organic solar cell - PSC was reported by Kim et al. (2010) by depositing blended P3HT and PCBM as active layers. The efficiency of the solar cell made by Kim was not as high as that using spin coating method, however, droplet deposition fabrication can realize large scale roll-to-roll manufacturing while spin coating is only limited to laboratory scale. With ongoing research, the efficiency of PSC made by droplet deposition method is believed to catch up or even exceed that of spin coating.

1.1.2 Printing of fine features

Efforts to adapt and extend graphic arts printing techniques for demanding devices in electronics, biotechnology and microelectromechanical systems (MEMS) have grown rapidly in recent years. In many applications, small line width is required for the purpose of saving material and miniaturizing the device. Fine patterns can be readily printed with small droplets, for example, ink-jet printing, whose resolution is defined by the narrowest continuous lines or smallest gaps that can be reached, is ~ 20-30 μm. Printing resolution is determined by the combined effect of droplet size that are usually no smaller than ~10-20 μm and placement errors that are typically 10 μm at a standoff distance of 1mm.

Researchers have been seeking various methods for fine pattern printing. Lee et al. (2007) used a fine liquid jet directly to print inductors on polyimide substrate with silver nano particles and reached a resolution of 100 μm. In their setup, a 10 μm jet is generated by charging the liquid and thus forming a Taylor cone jet (Taylor, 1964). The

jet is directly used for printing before it breaks up. As the jet is very difficult to stabilize, they have to use very viscous liquid (ethylene glycol) and high axial electric field to stabilize it. The line width of their printed pattern is on the order of 100 μm due to the slow motion of the substrate (10mm/s). Increasing the substrate velocity will reduce the line width. Wang (2005) used similar method and printed lines with ~ 17 μm in width. Print pattern with even smaller line width is possible as long as small droplets can be generated. Park et al (2007) printed dots and lines with several microns resolution and further developed thin-film transistors (TFT) based on their technique of small droplet generation. In their method, the liquid is fed in through a very small nozzle (~1 μm), the nozzle is held at high potential (several kV) with respect to a nearby substrate on which pattern is printed. Jetting is possible when the combined effect of liquid pressure and Maxwell stress overcomes the surface tension stress. Compared with the direct printing method using the unbroken jet, this method has better resolution and easier control, the disadvantage is that the much smaller nozzle radius greatly increased the possibility of clogging.

From the second factor which contribute to the printing resolution (placement error), it is straightforward to think of focusing the droplets in space before they are used for printing. With proper electric field control, charged droplets can be focused to a certain spot in space. These droplet focusing methods include quadrupole focusing (Yang, 2012) and electric lens focusing (Helmut, 2008). In quadrupole focusing, quadrupole rods and AC field are used to focus the charged droplets to the center line of the linear quadrupole, while in electric lens focusing, ring or plate electrodes with holes

and DC voltage are used, which focuses the droplets to a fixed point. Under proper control, both of these two methods can eliminate the placement error and print patterns with resolution solely determined by the droplet size.

1.1.3 Application of monodisperse droplets

Recently, monodisperse droplets have attracted increasing attention. It has been used in areas such as lasing droplets (Chang, 1986), drug delivery (Xu, 2009), combustion (Correa, 1982), microfluidics (Squires, 2005) and aerosol instrumentation calibration (Berglund, 1973) due to its narrow size distribution.

Figure 1(a) shows the phenomena in lasing droplet experiment (Chang, 1986). In the figure, dye doped ethanol droplet was generated by piezoelectric droplet generator. Through the irradiation of an intense laser bean, the resultant laser emission from inside the droplet highlights the liquid-air interface. The highlighted surface is a result of the standing wave with greatly enhanced field strength confined at the liquid-air interface.

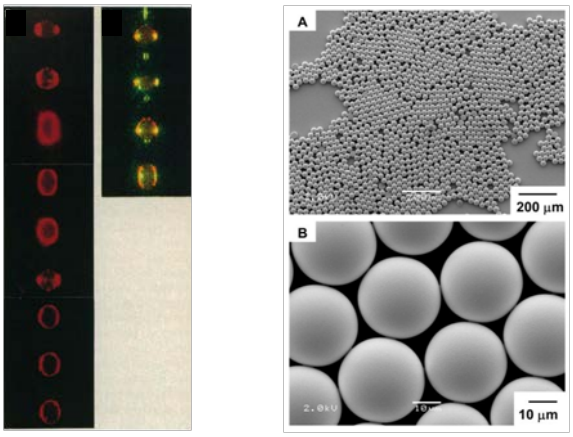

(a) Lasing droplets (b) Drug delivery

Figure 1. Application of monodisperse droplets: (a)Lasing droplets (d~30 μm) (Richard Chang,1986) (b) SEM images of monodisperse PLGA microparticles (Q. Xu, 2009)

Such enhancement of field strength is due to the same phase of light wave upon completing one cycle inside the droplet. The droplet size is one deciding factor of such experiments, as the size will decide the wavelength of the resonant laser emission. For this reason, monodisperse droplets are used to fix the droplet size for controlled experiments.

Biodegradable micro particles is broadly used in drug delivery. One intensely studied biodegradable material is PLGA (poly lactic-co-glycolic acid), which is used as matrix in drug delivery to achieve controlled drug release (Uhrich, 1999). Monodispersity of the drug incorporated PLGA particle is very important in the delivery process as variation in particle size may produce undesirable variation in the rate of degradation, the stability of the drug and the kinetics of drug release (Sansdrap, 1993). Monodisperse drug loaded PLGA particles can be produced by removing the solvent of the monodisperse solvent-solute mixed droplets in a microfluidics flow focusing device (Xu, 2009). The better performance of monodisperse drug load particles is mainly due to the initial kinetics, which exhibits a significantly lower initial burst compared with polydisperse particles (Xu, 2009). Figure 1(b) shows the SEM image of drug loaded PLGA particle fabricated using micro-fluidics flow focusing(FF) method (Xu, 2009). These particles are nearly monodisperse with polydispersity = 3.9%, which has much narrower distribution compared with particles prepared with conventional emulsification method.

1.2 Liquid jets: a prelude for droplet generation

Droplets can be formed automatically through the breakup of a liquid jet without any driving force due to the development of infinitesimal environmental perturbations. The jet is intrinsically unstable due to the effect of surface tension, which tends to break up the jet into droplets to reduce the surface area to achieve lower energy. The natural perturbation from the environment consists of a wide range of frequencies originates from different types of perturbations such as electromagnetic noise, acoustic wave, mechanical vibration, and turbulent air flow. The liquid jet can pick up the appropriate frequencies and amplify them until the magnitude of the perturbation is as large as the jet radius to cause the break up. Typically the perturbation from environment is random, which is one main cause for the polydispersity of droplets from naturally break up jets (another cause is the generation of satellite droplets due to the nonlinear effects). In this study, prescribed periodic perturbation will be added to the jet so the environmental noise is suppressed and the applied perturbation stands out. Monodisperse droplet can be produced this way due to the dominant effect of applied perturbation and the merging of primary and satellite droplets. The liquid jet is a prerequisite, perturbation is added to the jet so its breaking up process can be controlled and studied. To cover a wide range of jet diameter, the following three jetting mechanisms are used in this dissertation.

1.2.1 Inertial jet

The simplest method to generate a jet is to force liquid through a nozzle. The liquid then obtains certain initial velocity and a jet is formed when liquid exits the nozzle. The

fully developed flow inside a uniform circular nozzle is the well known Hagen-Poiseuille (HP) flow whose pressure drop is inversely proportional to nozzle diameter raised to the fourth power. Due to this reason, enormous pressure may build up inside the nozzle when diameter is reduced significantly. The jet diameter is usually the same as the nozzle inner diameter and thus has a lower limit (on the order of tens of microns based on nozzle length) due to the large pressure required for pushing liquid through small nozzles. We term this jetting mechanism as *inertial jet* since it's caused by fluid inertia. Based on the fluid Weber number at the exit of the nozzle, the physical phenomena can be categorized to different regions, typically the dripping region, Rayleigh break up region, first wind-induced region, second wind-induced region and atomization region (Lin, 1998). Among these regions, the Rayleigh break up region produces a jet with negligible air flow effects and will be used in jet EHD perturbation experiment due to its simplicity.

1.2.2 Flow focused jet

The disadvantage of an inertial jet is its size cannot go very small (typically ~ 100 microns) due to huge pressure drop inside small sized nozzles. In many applications we require small jets, which is hard to produce by the inertial jet. The flow focused jet solves this problem by replacing the liquid-solid interface with liquid-gas interface and thus generating a much smaller jet (down to several microns). Such a device was invented by Ganan-Calvo (1997) and is shown in Figure 2.

As shown in Figure 2, the flow focused (FF) jet is generated by placing the liquid meniscus in a converging gas flow, which comes from upstream uniformly and only exits through a small orifice below the meniscus. Due to the pressure gradient and the shear stress exerted on the meniscus, it obtains a cusp shape and a jet is generated along the flow direction. This configuration eliminates the wall friction resistance and thus significantly reduced the achievable jet size.

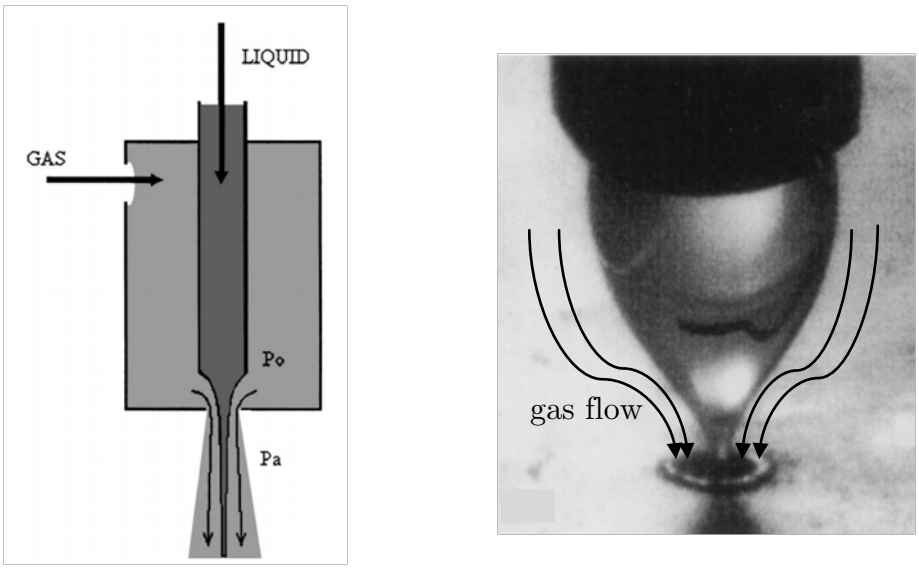

Figure 2. Flow focusing jet generator (Ganan-Calvo, 1997) (Left: illustration of device setup; Right: Image of FF in operation)

1.2.3 Taylor cone jet

The Taylor cone jet, typically known as electrospray when it breaks up to generate droplets, uses the electric force to reshape the meniscus into a cone; a fine jet then erupts the tip of the cone and breaks up into fine droplets. The droplets repel each other due to coulomb force and form a spray. Figure 3 shows a typical electrospray setup.

As shown in Figure 3, to form the Taylor cone jet, the liquid is fed in to a nozzle which is charged to high voltage. Below the nozzle is a grounded collector. Under suitable flow rate and high voltage conditions, a cone (Taylor cone) forms at the nozzle exit. A fine jet is generated at the tip of the cone. The jet size can be tuned from nanometers to hundreds of microns by changing operating parameters.

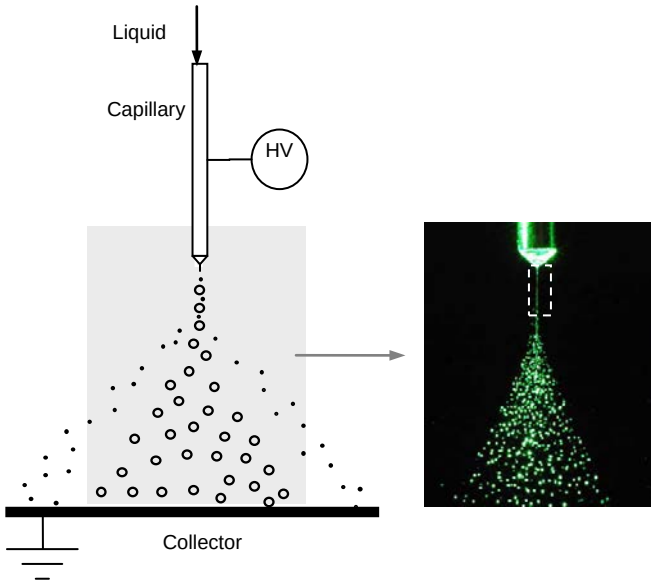

Figure 3. Electrospray setup (book chapter, Gomez and Deng, 2011)

Due to its unmatchable ability of small droplet generation (down to nanometer size), electrospray (Fenn, 1989) is a commonly used technique in complex functional film fabrication. The droplets generated by electrospray disperse themselves homogeneously in space before they reach the substrate due to the electric charge they carry, which is typically a fraction of the Rayleigh limit (Rayleigh, 1882). The droplet charge and size can be controlled to some extent by adjusting the liquid flow rate and conductivity

(through the addition of small amount of acids for example). The droplets' trajectory can be easily controlled by external electric fields. Film thickness can be controlled by either changing deposition time or solute concentration. The morphology of the deposited film can be dense, porous, or cracked, depending on the substrate temperature and solution properties (Khan, 2011). Through the addition of non-volatile liquid and controlling of the substrate temperature, the film morphology can be monitored (Jaworek, 2007).

1.3 Electrohydrodynamic (EHD) and other jet perturbation approaches

A jet is unavoidably perturbed by the white noise (acoustic noise, electromagnetic noise, non uniform air flow) from the environment with a wide frequency range no matter how small the magnitude is; the perturbations at certain wavelength will grow exponentially and eventually cause the jet to break up into droplets. This process is random since the perturbation from the environment is random. We can control the jet break up by applying a perturbation with a prescribed wave number, this perturbation thus stands out from the environmental noise due to its fixed wavelength and much larger initial magnitude. Different perturbations have been applied by researchers to study the jet break up process, such as acoustic perturbation, mechanical perturbation and electrohydrodynamic (EHD) perturbation. Among these methods, EHD perturbation has the advantage of non-intrusiveness to the flow field, the availability of cheap electric devices such as signal generators and power amplifiers and the easiness of control by constructing all kinds of electric fields at will. It uses an alternating current (AC)

electric field to perturb the jet periodically, allowing us to study the jet break up process by controlling the EHD perturbation parameters such as frequency, amplitude and waveform. In this section, we will briefly review the different jet perturbation methods.

1.3.1 Acoustic perturbation

The acoustic perturbation method uses sound wave to perturb the jet and give it an initial vibration with fixed frequency. Such a device was describe by Donnelly and Glaberson (1965) in their experiment to verify Rayleigh's dispersion relationship. Figure 4 shows the setup used by Donnelly and Glaberson (1965).

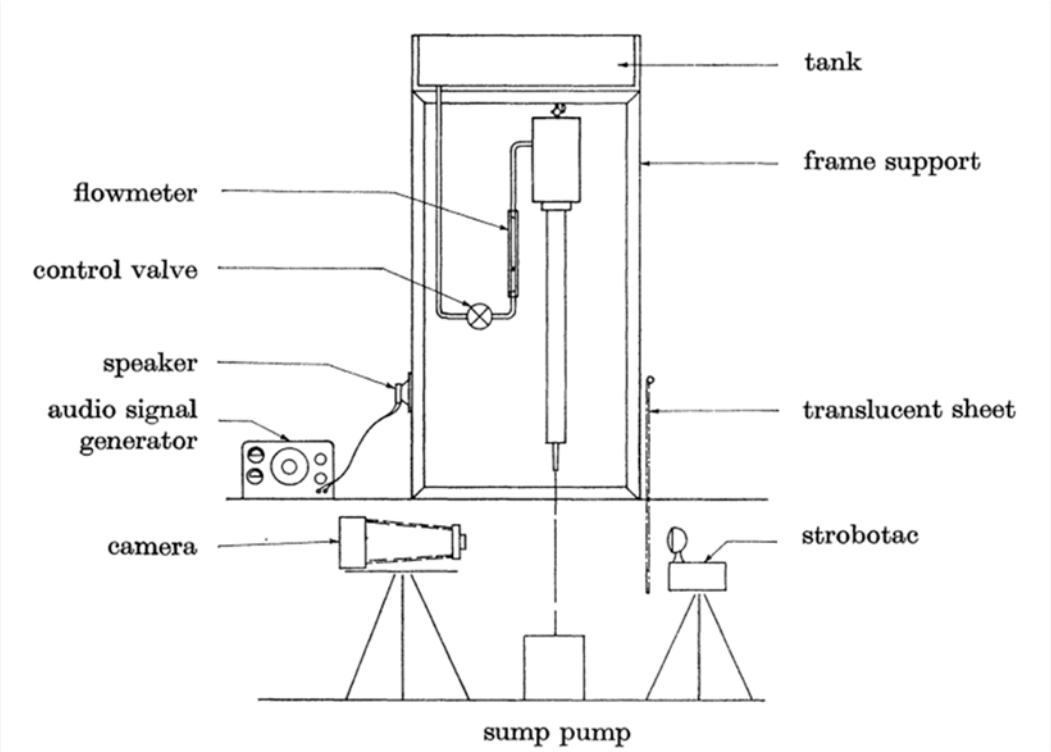

Figure 4: Acoustic perturbation on the liquid jet (Donnelly and Glaberson, 1965)

As shown in figure 4, a speaker is attached to the frame support which encloses the jet generation setup. The speaker generates audio signal which periodically perturbs the jet. Control valve is used to adjust the flow rate of the generated inertia jet, the flow meters reads the flow rate. The strobotac generate light flash to freeze the image taken by camera. Acoustic perturbation has simple setup but is not flexible in control. The perturbation is not focused in space and is hard for perturbing small jets.

1.3.2 Mechanical perturbation

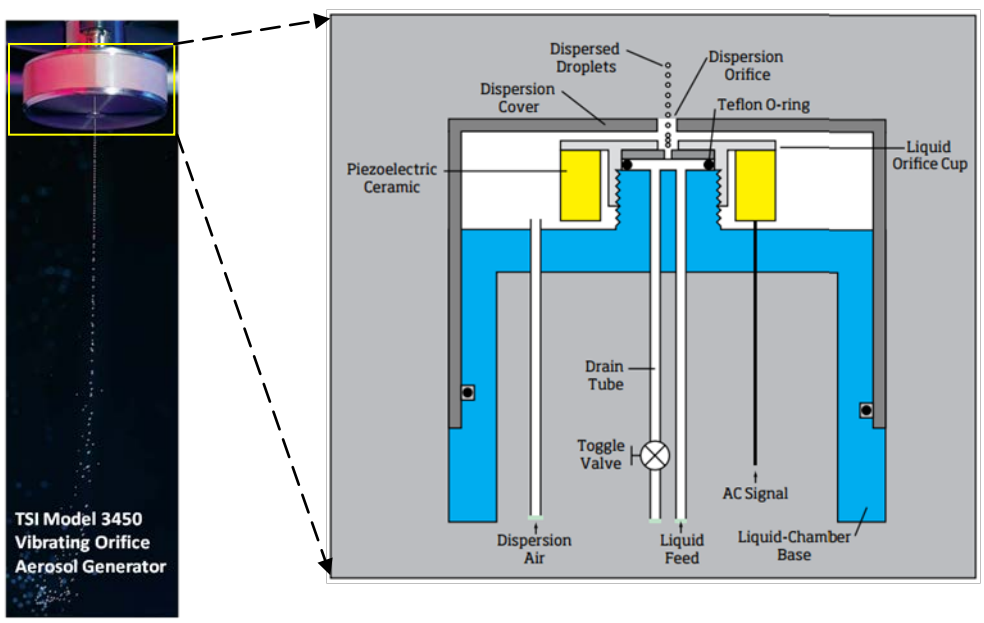

Figure 5. Piezoelectric aerosol generator (TSI Model 3450)

The mechanical perturbation to a liquid jet is introduced by attaching a piezoelectric actuator to the fluid line. Such a device was first invented by Berglund and Liu (1973). Figure 5 shows a commercial piezoelectric monodisperse aerosol generator. Such a

commercialized droplet and particle generator generates monodisperse droplet and particles from 1 to 200um.

Shown in Figure 5, the orifice through which jet forms has a diameters of 10 micron, whose length is made short to reduce the pressure drop, otherwise the pressure required will be too large to form the jet. The generated droplet typically has a size close to the jet size, however, it can be further reduced by using a mixture of two fluids with different evaporation rate. For example, by using mixture of alcohol and oil, after droplet generation, alcohol will be evaporated, leaving only oil with a smaller size determined by the component ratio.

1.3.3 EHD perturbation

In this study, EHD perturbation is chosen due to its easy setup and flexibility. One simplified illustration of an EHD perturbation device is shown in Figure 6.

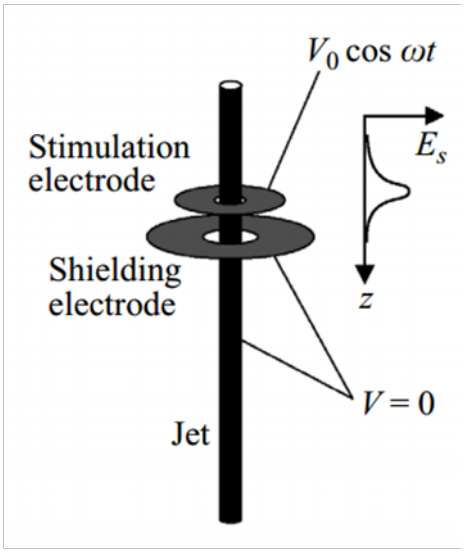

Figure 6. EHD perturbation (Gonzalez and Garcia, 2009)

As shown in Figure 6, in EHD jet perturbation, the electric field is introduced by two circular electrodes which are coaxial. The jet passes through the center of these two electrodes. The upper electrode is connected to a AC power supply which periodically perturbs the jet. The lower electrode has the same potential as the jet and is used to confine the electric field. Such a configuration allows researchers to study the effects of magnitude and frequency of applied perturbation by easily changing the parameters from the AC power supply. In this dissertation, we will use different electrode configurations and their advantages will be discussed.

1.4 Dissertation overview

Briefly, the contents of the ensuing chapters are:

Chapter 2 reviews the theories on the liquid jet instability, which begins with Rayleigh instability theory for uncharged jets, and goes on to cover spatial theory, nonlinear theory, charged and viscous jets and the break up length.

Chapter 3 explores the EHD perturbation on an inertia jet, in which two designs of EHD exciter are discussed in detail. The first EHD exciter design only works on uncharged jet and the second design works on both charged and uncharged jet, which also serves as a benchmark study for later experiments on flow focusing jet and Taylor cone jet EHD perturbation.

Chapter 4 focuses on the construction and EHD perturbation of a flow focused free jet. We designed and built the first slit flow focusing device that is different from previous orifice flow focusing free jet because the slit design is scalable and compatible

with EHD excitation. We demonstrated that the EHD perturbation on four linear jets with a single exciter.

Chapter 5 studies the EHD perturbation on Taylor cone jets. For the first time, a jet as small as ~10 micrometers was excited by transverse electric field. We discovered a range of remarkable phenomena which can be subsequently explained by linear perturbation model.

Chapter 6 summarizes the major findings in this work.

CHAPTER 2. THEORIES ON LIQUID JET INSTABILIT

2.1 Temporal Theory of the Instability of a Liquid Jet

The temporal theory is the first theory that successfully describes the unstable perturbations on a liquid jet. In the temporal theory, the liquid jet is assumed to be stationary in space and the initial perturbation grows with time.

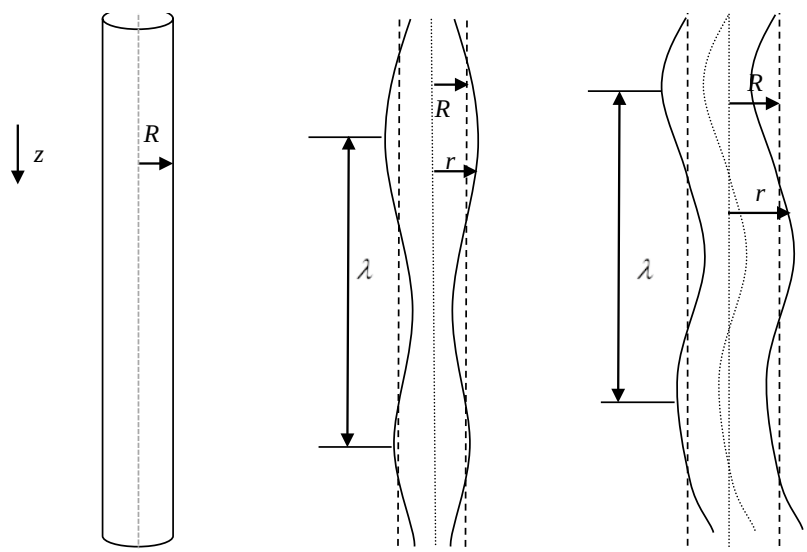

(a) initial status of a jet (b) m=0 (c) m=1

Figure 7. (a) initial state of the jet (b) the physical shape of instability corresponding to m=0 (c) the physical shape of instability corresponding to m=1.

Consider an infinitely long stationary liquid jet shown in Figure 7(a), the jet has a radius R, surface tension γ and density ρ, viscosity is neglected for the case considered

here. This liquid jet is intrinsically unstable due to surface tension. Any change in the surface shape which reduces the surface area is energetically favorable.

The kinematic treatment of this problem is first provided by Plateau (1849) and can also be found in the recent review by Eggers (1997). In the cylindrical system (r, φ, z) the jet surface shape can be written as $r = r(\varphi, z)$. Imagine an initial small perturbation is super-imposed on the stationary jet, which could be the acoustic or electromagnetic perturbations from the environment. Any perturbation can be decomposed into periodic waves through Fourier transform. The jet profile with a periodic perturbation super-imposed on it is written as:

$$r / R = 1 + \varepsilon(t)\cos(m\varphi)\cos(x\zeta) \tag{2.1}$$

where $\varepsilon(t)$ is a small value initially (at t=0) but can evolve with time, m is an integer which takes the value of 0,1,2..., x is the wave number defined as $x = 2\pi R / \lambda$ with λ being the axial wave length, ζ is the axial position non-dimensionalized by R, $\zeta = z / R$. Equation (2.1) ensures that along the circumference of the jet, the wave amplitude repeat itself every 2π and along the axial direction, the wave is periodic with a wavelength λ. Figure 7(b)(c) show the physical shapes of instability modes with m=0 and m=1. The m=0 mode is called the varicose mode which is the reason for jet to break up into droplets; the m=1 mode is called whipping mode where the jet swings and is often seen in electrospinning (Hohman, 2001). Other modes corresponding to higher m values are not discussed here. The surface area A in one wavelength (derivation can be found in Eggers' (1997) review paper) is expressed as:

$$A = 2\pi R\lambda[1 + \frac{\varepsilon(t)^2}{8}(1+\delta_{m0})(x^2 + m^2 - 1)] \tag{2.2}$$

where δ_{m0} is the delta function whose value is 1 when m=0 and 0 for all other cases. Any perturbation will grow if it reduces the surface area A. Equation (2.2) shows that the only possible combination for a reduction of A is m=0 and x<1. In other words, only the varicose mode is unstable for the inviscid uncharged jet and the wavelength of the unstable perturbation is larger than the circumference of the jet.

From equation (2.2) it seems that the perturbation of smaller x or larger wavelengths are the more rapidly growing ones since they reduce the surface area more. However, this is not the case because equation (2.2) is derived simply from the kinematic point of view. Rayleigh (1879) first considered the dynamics of an inviscid jet and obtained a relationship between the perturbation wave number and growth rate. In Rayleigh's theory, the jet profile is written as:

$$r = R + \varepsilon \exp[\omega t + i(x\zeta + m\varphi)] \tag{2.3}$$

where ε is the magnitude of the initial natural perturbation and its value is experimentally determined to be around $e^{-12}R$ (Lin,1998), (x,m) defines the wavenumber and mode of the perturbation. The real perturbation is a superposition of all kinds of (x, m) combinations. Assuming the perturbation is small, linearization can be applied where each (x,m) combination can be treated individually and independently. A detailed derivation for Rayleigh's dispersion relationship can be found in Appendix A, and the final solution takes the following form:

$$\omega^2 = \omega_0^2 \frac{xI_m^{'}(x)}{I_m(x)}(1 - x^2 - m^2) \tag{2.4}$$

where ω_0 is the characteristic growth rate defined as $\omega_0 = \sqrt{\gamma / \rho R^3}$, which is also the characteristic frequency of free oscillating droplets. It's inverse $t_c = 1/\omega_0 = \sqrt{\rho R^3 / \gamma}$ is called capillary time which is the time scale of the jet evolution. $I_m(x)$ is modified Bessel function of the first kind of order m.

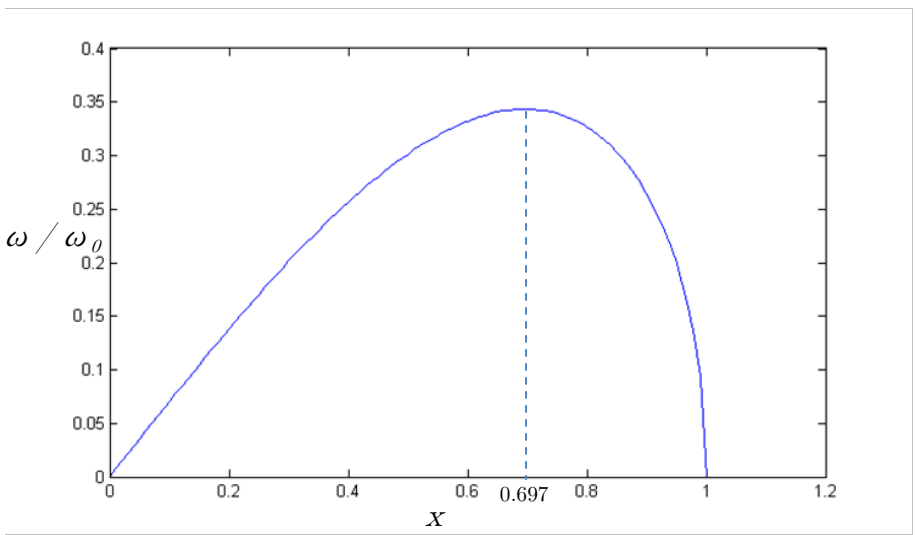

Figure 8: Rayleigh dispersion relationship

Equation (2.3) suggests that a positive real ω corresponds an unstable perturbation where its magnitude grows exponentially in time, while a negative ω corresponds to a stable perturbation where the magnitude decreases exponentially in time, and an imaginary ω corresponds to the surface oscillation whose magnitude does not change with time. According to Rayleigh dispersion relationship (2.4), the only combination corresponding to a positive ω or unstable perturbation is m=0 and x<1. In other words,

only the varicose mode is unstable and the wavelength is larger than the circumference of the unperturbed jet, in accordance with Plateau's conclusion. Equation (2.4) is plotted in Figure 8, and the highest growth rate (or the most unstable mode) appears at x_R=0.697.

The dispersion relationship found by Rayleigh has been verified by various researchers experimentally. Donnelly and Glaberson (1965) were the first ones to experimentally verify this relationship. They attached a speaker to the frame support of jet generation setup and used audio frequency to excite the jet. Jet profile was observed by taking photographs and the magnitude of the perturbation was taken as half of the difference between adjacent swells and necks. They found experimental data were consistent with the equation of exponential growth to within one wavelength of the disengagement of the droplet from jet and concluded nonlinear effects does not come to play at that period. Goedde and Yuen (1969) pointed out instead that nonlinear effects dominate the perturbation growing process, that Donnelly and Glaberson's result was due to their experimental method. The growth of the swell and neck are non-linear, the difference between the swell and neck are linear and agree well with Rayleigh's theory because of the nonlinear effects cancel out when taking the difference between the swell and neck. The nonlinear effect will be reviewed to some extent in section 2.2. Cline and Anthony (1978) studied the effect of harmonics on the liquid jet by applying various waveforms on the oscillating speaker used as a perturbation source and extended Rayleigh's analysis to nonlinear region. Other experimental works that verified

Rayleigh's theory can be found in papers by Wetsel (1980), Collicott (1994), Chauhan (2003), Kalaaji (2003) and Gonzales (2009).

2.2 Spatial Theory and Nonlinear Effects

The temporal theory found by Rayleigh, though simple, cannot be directly applied to a jet in the experiment, which usually has certain initial velocity. In Rayleigh's theory, the jet is stationary and instability develops with time everywhere in space. To apply the temporal theory, the jet velocity can be reduced to zero by a simple linear transformation in the coordinate system; however, Rayleigh's theory predicts that instability will grow at the beginning of the jet where it exits the nozzle, which is not observed in experiment. When a real jet exits the nozzle, it is always stable at the nozzle exit where the jet diameter is kept as R. Keller et al (1973) developed the spatial theory which fills up the gap between Rayleigh's theory and a real jet in experiment. In Keller's spatial instability theory, the perturbation grows with the axial distance instead of time. This is what we observe in a real experiment: the perturbation grows downstream of the jet and eventually causes it to break up. In a fixed spatial position before break up, the phenomena is periodic oscillation of the jet surface which never grows in amplitude. In the spatial theory, the perturbation is written as:

$$r = R + \varepsilon \exp[i(\omega t + x\zeta + m\varphi)] \tag{2.5}$$

Here ω is real and x is complex, corresponding to a perturbation which is oscillatory in time and grows in space, in contrast to Rayleigh's theory where perturbation is oscillatory in space and grows with time. The spatial growth rate is $Im(x)/R$ and the

wavelength is *2πR/Re(x)*. The dispersion relationship obtained by Keller (1973) takes the following form:

$$\beta^2(\Omega - x)^2 I_m(x) = xI_m^{'}(x)(x^2 + m^2 - 1) \tag{2.6}$$

where β, Ω are defined as:

$$\beta^2 = We = \frac{\rho v_{jet}^2}{\gamma / R} \quad , \qquad \Omega = \frac{\omega R}{v_{jet}} \tag{2.7}$$

In expression (2.7) v_{jet} is the velocity of the jet which does not appear in Rayleigh's dispersion relationship, *We* is the Weber number which compares the relative importance between jet inertia and surface tension, Ω is the dimensionless frequency and is a real number since the frequency ω is real in the spatial theory. Now we need to solve the implicit equation (2.6) for x when β and Ω are given (whose values can be obtained from v_{jet}, R and ω), the real part of x is related to the wavelength and the imaginary part of x is related to the growth rate. The solution can be read from a plot in the *Re(x)* and *Im(x)* plane where the solution curves for fixed β and Ω are plotted. Such a plot for m=0 can be found in (Keller, 1973) on spatial instability theory, which shows that the contours for large β are very close to the Rayleigh dispersion relationship curve. Take $\beta = 10$ for example: the real x value for the unstable perturbation happens at $0 < \mathrm{Re}(x) < 1$, since the wavelength and *Re(x)* is related by $\lambda = 2\pi R / \mathrm{Re}(x)$, this corresponds to $0<x<1$ in Rayleigh's theory. The most unstable mode corresponds to the largest values of $|Im(x)|$, or the lowest points in the constant β contour, Keller's spatial theory shows this happens at approximately $\Omega = 0.7$, which

is close to Rayleigh's predicted value of $x = 0.697$ by noticing that the perturbation is convected downstream by the jet velocity, so $\lambda = v \cdot \frac{2\pi}{w}$, or $x = \frac{2\pi R}{\lambda} = \frac{wR}{v} = \Omega = 0.7$. Thus the spatial theory is very close to the temporal theory for high β values. For small values of β, the dispersion relationship deviates from Rayleigh's theory. Below a critical value of $\beta = \beta_c = 1.77$, another region of instability called absolute instability is found by Leib and Goldstein (1986), as opposed to the convective instability studied here. In the absolute instability, the surface wave develops both downstream and upstream, which is the reason for dripping instead of jetting under low flow rates. In this study, the jet Weber number is always large, so the temporal theory can be safely applied.

Rayleigh's dispersion relationship is derived from a linear assumption (Appendix A) in which the products of perturbations are ignored. The linear theory predicts sinusoidal surface profile during the development of a perturbation and no satellite droplet formation during breakup; however this is usually not the case as observed in experiment. It is because in the linear theory, one crucial assumption is "small perturbation", so that the products of the perturbations can be neglected as higher order terms in analysis. As the perturbation develops, its magnitude becomes larger and larger and eventually the product term cannot be ignored. To explain the phenomena of deviation from sinusoidal jet profile and satellite formation during breakup, one has to turn to nonlinear theory. These nonlinear analyses include Wang (1968), Yuen (1968), Nayfeh (1970), Lafrance (1975) and Chaudhary (1980), with Rayleigh's linear theory

being the first order approximation. A review of the nonlinear theory and jet breakup process can be found in Bogy (1979). The nonlinear analysis of a jet is a difficult problem, with different researchers reaching different conclusions in the above listed references, mainly due to the different mathematical method used. However the experimental results of the nonlinear behavior of a liquid jet breakup by different researchers shares much more in common. Goedde and Yuen (1970) published the first experimental paper on nonlinear liquid jet breakup, in which they observed the non-sinusoidal jet profile and satellite formation. Their experiment shows "the first break-up point to form a separated ligament always occurs on the downstream end of the ligament. This is because the downstream end has had more time to contract." They also discovered the satellite droplet size decreases with increasing wavenumber. Goedde and Yuen's results corresponds to a situation when the initial perturbation is small, when the initial perturbation magnitude increases, the satellite formation passes different regions as observed by Pimbley and Lee (1977). Their results showed that at small initial perturbation, the satellite formation falls in the "Rear-merging" zone, where the ligament first breaks up on the downstream and merges with its rear main droplet; as the initial perturbation increases, it reaches "Infinity condition", where the ligament breaks up symmetrically on the downstream and upstream, forming a satellite droplet which never merges with the main droplet; further increasing the perturbation magnitude causes the satellite to fall in the "Forward-merging zone", where the ligament breaks up on the upstream first, forming a satellite droplet which merges with its forward main droplet; finally when the initial perturbation is large enough, no satellite

will form during the break up, the break up is called "No satellite formation" zone. EHD perturbation typically falls in the "Rear-merging" zone.

In this work, the linear temporal theory is chosen to analyze the results since the Weber number concerned here is large so that the temporal theory is very close to spatial theory. Nonlinear effects usually dominate at the break up points and does not affect the overall surface wave growing process, so it is not the central focus of this study.

2.3 Dispersion Relationship for a Charged Inviscid Jet

In section 2.1 and 2.2 the dispersion relationships for uncharged inviscid jet are discussed. For the charge neutral inviscid jet, only fluid inertia and surface tension are considered in obtaining the dispersion curve. However, when the jet is charged, the Coulomb force on a liquid segment from the rest of the jet must be considered. The spatial treatment of the dispersion relationship for a charged inviscid jet was worked out by Melcher (1963) and Crowley (1965). When the jet Weber number is high (>10, which holds true for most cases), the temporal theory is very close to the spatial theory under a simple coordinate transformation. We will follow the temporal theory since it is much simpler to implement. The temporal dispersion relationship was derived by Huebner and Chu (1970) through a detailed energy analysis. Jet surface charge is related to the radius (b) of an imaginary grounded cylinder which is coaxial with the jet. It is convenient to assume this radius is fixed by setting $\ln(b/R)=1$ without losing generality, as is adopted by Eggers (2008). The dispersion curve thus takes the following form:

$$\omega^2 = \frac{\gamma}{\rho R^3} x \frac{I_m^{'}(x)}{I_m(x)} \cdot [(1 - m^2 - x^2) - \Gamma(1 + x\frac{K_m^{'}(x)}{K_m(x)})] \tag{2.8}$$

In dispersion relation (2.8), ω is the growth rate (the development of perturbation scales with $e^{\omega t}$), $I_m(x)$ and $K_m(x)$ are modified Bessel function of the first and second kind, m is an integer which takes the value of 0,1,2... We will deal with m=0 and 1 only which corresponds to the varicose instability and whipping instability. Dimensionless charge level Γ is the ratio between the electric stress and surface tension stress which takes the form:

$$\Gamma = \frac{\sigma^2 / \varepsilon_0}{\gamma / R} \tag{2.9}$$

where σ is the surface charge density on the jet surface, ε_0 is vacuum permittivity. Equation (2.8) is plotted for m=0 and m=1 in Figure 9 for different charge levels.

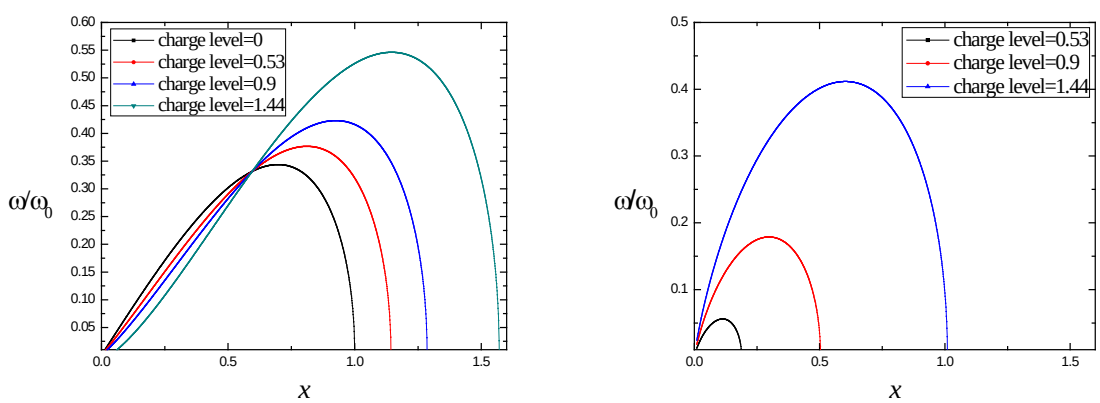

(a) m=0 (b) m=1

Figure 9: Plot of dispersion relation (2.8) for m=0 (a) and m=1(b) at different charge levels.

Figure 9(b) shows that the whipping mode is stable for small charge levels because the dispersion curve for small Γ is non-exist, numerical calculation of equation (2.8) shows the dispersion curve for m=1 only exists for a charge level larger than 0.21. For varicose instability, when $0 < x \leq 0.6$, the charge reduces the growth rate due to the stabilizing effect of surface charge at this range (Eggers, 2008). When x > 0.6, the destabilizing effect of the surface charge becomes significant which increases the growth rate. As the charge level increases, both growth rate for varicose (for cases when x>0.6) and whipping instability will increase, with the most unstable wave number moving to a larger value. There are cutoff wave numbers above which the varicose and whipping perturbations are both stable, with varicose cutoff wave number always larger than that of whipping.

2.4 Dispersion Relationship for uncharged Viscous Jet

Rayleigh and Huebner's dispersion relationship only applies to inviscid jets. Weber (1931) first obtained the dispersion relationship for a viscous jet in the varicose mode, which takes the following form:

$$\omega = \omega_0 \{ [\frac{1}{2} x^2 (1 - x^2) + \frac{9}{4} \mathrm{Re}^{-2} x^4]^{1/2} - \frac{3}{2} \mathrm{Re}^{-1} x^2 \} \tag{2.10}$$

where Re is the Reynolds' number defined as $\mathrm{Re} = \frac{v_{jet} R}{\upsilon}$ with υ being the kinematic viscosity of the liquid. This dispersion curve can also obtained by expanding Chandrasekhar's complicated implicit equation (Chandrasekhar, 1961) for small x. The

above dispersion relation shows that the growth rate is now a function of both wave number and Reynolds' number. According to this dispersion relationship, the fastest growing wave number is determined by:

$$x^2 = \frac{1}{2 + \sqrt{18} / \mathrm{Re}} \tag{2.11}$$

When Re~∞, as for the inviscid jet, we get x=0.707, which is close to Rayleigh's prediction of x_R=0.697. An increase in viscosity reduces Re, and subsequently reduces the most unstable x value, causing the jet to break up at longer wave lengths. The dispersion relation (2.11) is plotted in Figure 10.

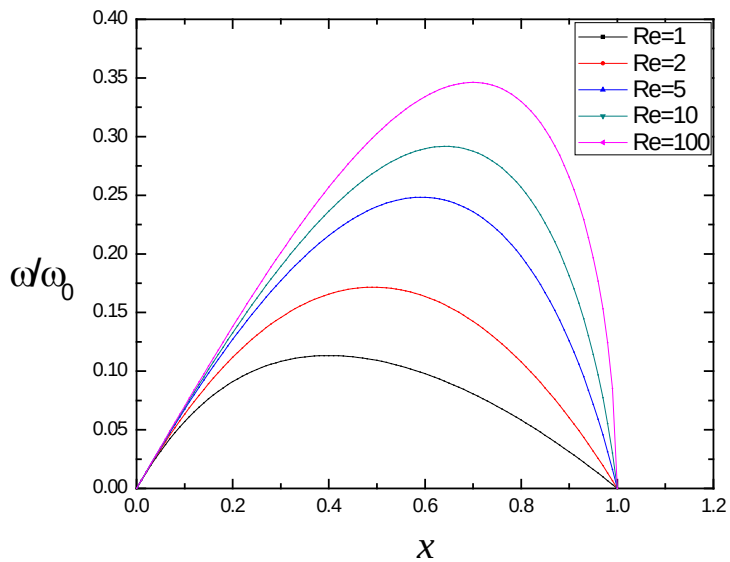

Figure 10: Dispersion relationship for a viscous jet at different Reynolds number for the varicose mode.

From Figure 10 it is concluded that at lower Reynolds number, or higher viscosity, the growth rate reduces, the most unstable perturbation moves to a smaller

wave number. As the Reynolds number gets higher, the dispersion curve gets closer to the Rayleigh dispersion curve. From the expression of the Reynolds number it is also concluded that low jet velocity and small jet diameter are also reasons for the dispersion curve to deviate from Rayleigh's prediction.

The dispersion relationship for a viscous jet considering all perturbation modes are done by Saville (1970), which takes a complicated implicit form and needs to be solved numerically. Saville's results show that viscosity dampens the varicose mode more than the whipping mode so that the whipping mode can be dominant in many situations, such as electrospinning for polymer solution or melts (Reneker, 2007).

2.5 Dispersion Relationship for a Charged Viscous Jet in Varicose Mode

Things get more complicated when fluid inertia, surface tension, surface charge and viscous dissipation all needs to be considered. Hartman (1999) obtained a dispersion relationship for a charged jet considering all these factors for the varicose mode, which takes the following form:

$$(\frac{\omega}{\omega_0})^2 + oh \cdot x^2 (\frac{24 + x^2}{8 + x^2}) \frac{\omega}{\omega_0} = \frac{4x^2}{8 + x^2} \{1 - x^2 - \Gamma[1 + x \frac{K_0^{'}(x)}{K_0(x)}]\} \tag{2.13}$$

Where oh is the Ohnesorge number defined as $oh = \mu / \sqrt{2\gamma\rho R}$ with μ being the dynamic viscosity of the liquid. The Ohnesorge number describes the ratio of energy loss due to viscosity and potential energy of the jet due to surface tension.

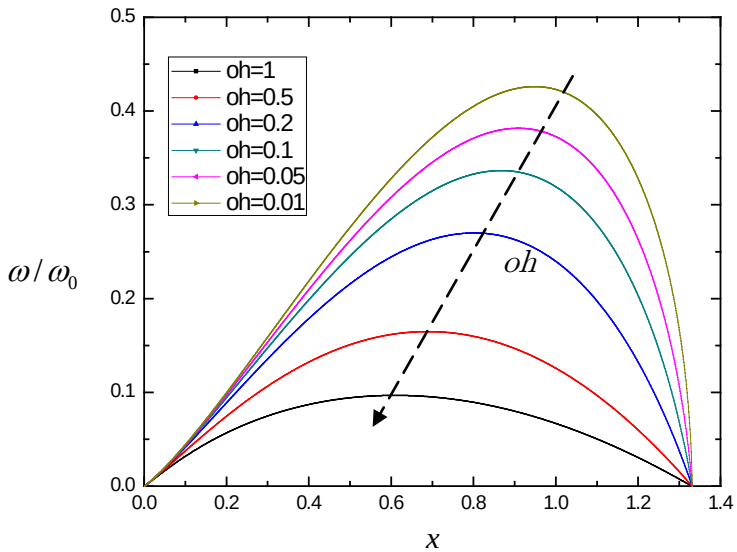

Figure 11: Dispersion curve for Γ=1 and different oh values.

Hartman's dispersion relationship (Equation 2.13) is plotted in Figure 11 for fixed charge level with varying oh value and Figure 12 for fixed oh value with varying charge levels. From the dispersion curves (Figure 11,12) one concludes that surface charge moves the most unstable wave number to a larger value while viscosity moves it to a smaller value. Surface charge expands the unstable wave number range while viscosity does not affect the unstable wave number range.

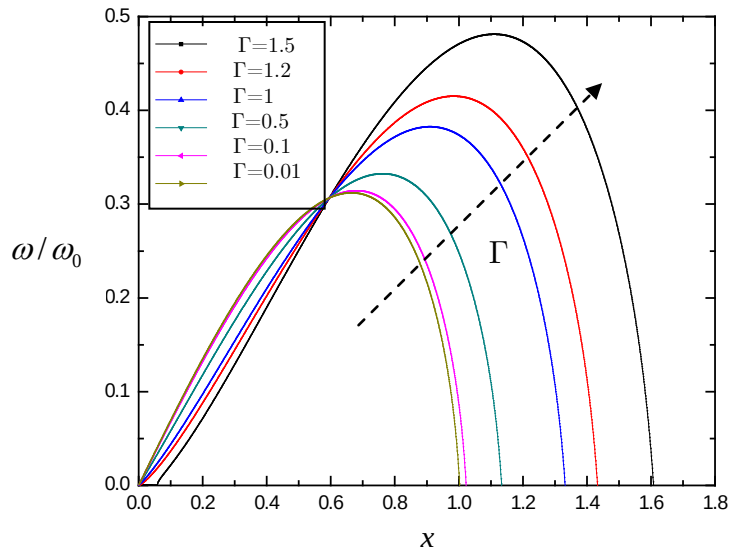

Figure 12: Dispersion curve for oh=0.05 and different Γ values.

2.6 Breakup Length

In this section, the breakup length is derived based on the AC voltage and frequency. Results obtained here will be used in ensuring chapters. For small initial perturbation, the magnitude is supposed to be proportional to the electric pressure (Gonzalez, 2009). Following Gonzales, we can get the break up length as a function of initial perturbation and the growth rate.

For a neutral jet, the electric pressure is proportional to the electric field square which has the form $\frac{1}{2}\varepsilon_0 E^2$, since the electric field is also proportional to the EHD voltage V_0, we can write the initial perturbation as:

$$f_0 = AV_0^2 \tag{2.14}$$

This initial perturbation grows exponentially if the EHD perturbation wave number is at the unstable wave number range. The perturbation magnitude as a function of z, the vertical distance from where the perturbation is applied, can be expressed as:

$$f(z) = AV_0^2 \exp(kz) \tag{2.15}$$

where k is the spatial growth rate, which is related to the temporal growth rate by $k = \omega / v_{jet}$.

At the position of jet break up, the perturbation has a magnitude equal to the jet radius. The distance from the position of initial perturbation (typically at beginning of the jet) and the break up point is called break up length L_b. At break up point, the perturbation grows to a magnitude as large as the jet radius, we have:

$$AV_0^2 \exp(kL_b) = R \tag{2.16}$$

Take the natural log of both side in the above equation and rearranging, we get:

$$L_b = a - b \ln V_0 \tag{2.17}$$

where $a = \frac{\ln(R/A)}{k}$ and $b = \frac{2}{k}$. If we plot L_b as a function of $\ln V_0$, the slope will allow us to calculate the spatial growth rate k, and the intercept will give us information about the constant A.

As for a charged jet, and under the condition of small initial perturbation, the initial perturbation magnitude should be proportional to both the applied AC voltage and jet charge density σ. We can write the initial perturbation as:

$$f_0 = AV_0\sigma \tag{2.18}$$

Applying the same method we arrive at:

$$L_b = \frac{\ln(R/A)}{k} - \frac{\ln(V_0\sigma)}{k} \tag{2.19}$$

The surface charge density can be obtained by measuring the current (Chapter 3 experimental section). If we plot L_b and $\ln(V_0\sigma)$ in the same graph, from the slope and intercept, we can also get the perturbation growth rate and the constant A.

CHAPTER 3. EHD PERTURBATION ON AN INERTIA JET

In this chapter, we focus on EHD perturbation on an inertia jet pressurized from a small nozzle (ID 150µm, OD 300µm). The inertia jet is easy to generate and the jet size is large enough to allow high resolution imaging and temporal analysis. The result obtained from this chapter serves as a benchmark for following chapters, in which substantially smaller jets will be investigated. Two types of EHD exciters are developed and analyzed. The first EHD exciter uses the fringe electric field of a capacitor as perturbation source, which has the simplest electrode configuration and is only useful for uncharged jets, because charged jets may be attracted to the asymmetric electrode and interrupt the jet generation. The second design of EHD exciter uses the electric field between two sharp blades which are placed horizontally and symmetrically on both sides of the jet. Due to the symmetry of the two electrodes, the charged jet can keep straight at its initial stage before perturbation develops. Such a configuration works for both uncharged and charged jets and is also used in the flow focused jet perturbation in Chapter 4 and Taylor cone jet perturbation in Chapter 5.

3.1 EHD excitation on uncharged liquid jet with capacitor configuration

3.1.1 Generation of an inertia jet

In inertia jet EHD perturbation, the first step is to generate a liquid jet before applying perturbation on it. In this chapter, the inertia jet is produced by forcing liquid through a 30 gauge needle (ID 150µm, OD 300µm). At adequate conditions, the liquid at the

needle exit forms a uniform jet with diameter very close to the needle inner diameter. The physical outcome at the exit of the nozzle when liquid is forced through it depends on large amount of parameters, such as nozzle internal flow effects, jet velocity profile, turbulence at the nozzle exit, the physical and thermodynamic state of both liquid and gas (Lin, 1998). In our case, the nozzle is uniform and has no complicated internal structure. It is long enough so the flow can be fully developed to HP flow. The most important factor here is the liquid and gas Weber number, which are defined as:

Liquid Weber number:

$$We_L = \rho_L U^2 R / \gamma \tag{3.1}$$

Gas Weber number:

$$We_g = \rho_g U^2 R / \gamma \tag{3.2}$$

where ρ_L and ρ_g stands for liquid and gas density respectively, U and R are the jet velocity and radius, γ is the liquid surface tension. The liquid and gas Weber number compares the liquid and gas inertia force with the surface tension force respectively. Briefly, the different physical phenomena under different Weber numbers are described below. A more detailed description can be found in Lin (1998).

(1) Dripping zone: $We_L < 8$

For $We_L < 8$, the liquid inertia force is not strong enough the overcome the surface tension force. Under such a situation, absolute instability (Leib, 1986) develops and propagates upstream to interrupt the formation of a jet. Droplets form and fall

under the balance between gravity and surface tension. Droplets generated this way are uniform but have large size (a few millimeters).

(2) Rayleigh breakup zone: $We_L > 8$ and $We_g < 0.4$ or $1.2+3.41Z_1^{0.9}$

Where $Z_1 = We_L^{0.5}/Re_L$, $Re_L = 2UR/\mu_L$ is the Reynolds number which compares inertia force to viscous force, μ_L is dynamic viscosity of the liquid. In Raleigh breakup zone a steady jet is formed and the effect of surrounding gas can be ignored. Under a moving coordinate system fixed on the jet, the jet is stationary and the growth of perturbation can be described by Rayleigh dispersion relationship, hence the name Rayleigh breakup zone. $We_L > 8$ ensures that a jet can be formed while $We_g < 0.4$ is suggested by Ranz (1956) which corresponds to the inertia force of surrounding gas reaching 10% of the surface tension force. Above this threshold the gas effect is assumed to be not negligible. Another indication for the importance of gas inertia is the maximum length of jet break up length. As the jet velocity increases, the jet break up length first increase linearly, reaches a maximum and started to decrease (Lin, 1998). Numerical results of Sterling & Sleicher (1975) indicated the maximum break up length is reached when $We_g = 1.2+3.41Z_1^{0.9}$, above this value, the influence of the surrounding air inertia force cannot be ignored.

(3) First wind-induced zone : 0.4 or $1.2+3.41Z_1^{0.9} < We_g < 13$

At this zone, the air inertia cannot be ignored, which causes the jet to breakup earlier when the jet velocity is further increased. The droplet size formed in this zone is close to the jet size. The value 13 is determined by Ranz (1956) where he argued that the gas inertia force is of the same order as the surface tension force when $We_g = 13$.

(4) Second wind-induced zone: $13 < We_g < 40.3$

At this zone, the interaction between the jet and surrounding gas is dominant, the droplet generated is smaller than the jet diameter and break up happens some distance downstream of the nozzle. The value of 40.3 is suggested by Miesse (1955); above that value the breakup falls in atomization zone.

(5) Atomization zone: $We_g > 40.3$.

It is suggested by Miesse (1955) that when $We_g > 40.3$, the break up falls in the atomization zone, where the breakup appears to start at the nozzle exit and the droplet generated is orders of magnitude smaller than the jet size.

Among these operation zones, the Rayleigh break up zone is the only one which ensures the formation of a steady jet and ignores interaction with surrounding gas. To simplify the problem and make it manageable, our experiments of EHD perturbation are based on jets in the Rayleigh breakup zone.

3.1.2 Experimental Setup

EHD perturbation on an uncharged inertia jet uses the fringe electric field of a capacitor as a perturbation source, we call it the 1st generation EHD exciter as opposed to the 2nd generation to be described later. Figure 13 shows the experimental setup. The liquid jet is generated by forcing ethanol through a gauge 30 nozzle (inner diameter 150 µm) using a high pressure syringe pump (not shown in Figure 13). The flow rate used in this experiment is 100~200 ml/hr to ensure the jet is operating in the Rayleigh break up zone. At this range, a stable jet with negligible surrounding air effect can be produced.

The jet Weber number is of order 10, indicating inertia is dominant compared with surface tension. The jet Reynolds number is of order 100, so the jet is approximately inviscid. The perturbation is introduced by placing two parallel electrodes (capacitor) close to the jet. The two electrodes of the capacitor is connected to amplified AC voltage. The capacitor is mounted to a 3D stage so its position can be precisely adjusted. The distance between the two electrodes 2a is about 400 um. The frequency of the applied AC field can be changed from 0 to hundreds of kHz. The peak to peak voltage $V_{p\text{-}p}$ can be tuned from 0 to 400V. Once AC is on, charge is induced on the jet surface due to the fringe electric field of the capacitor. The fringe electric field then interacts with the induced surface charge to give the jet a periodic perturbation.

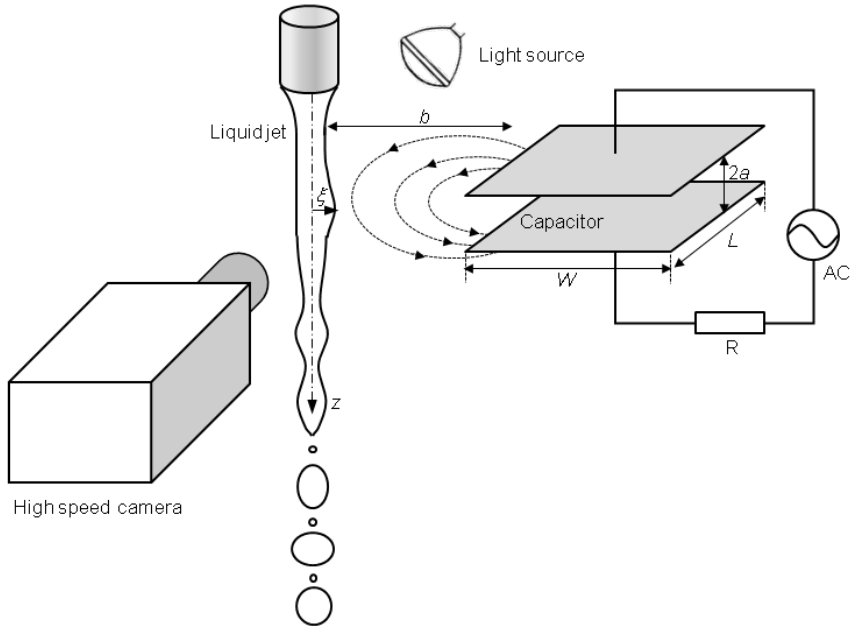

Figure 13. Experimental setup of the uncharged jet under electro-hydrodynamic perturbation

A light source is placed behind the jet to provide illumination for the high speed camera, forming shadow graph of the jet on the camera sensor. The high speed camera (Phantom v12.1, Vision Research) has a full resolution of 1280 x 800 pixels with pixel

size of 20 µm. Upon coupling with 2x or 4x magnification lens, the camera provides a resolution up to 5 microns per pixel. In this experiment, the typical resolution used is 512 x 256, with a frequency of 22,000 frames per second and a shutter speed of 10 µs.

3.1.3 Factors affecting perturbation magnitude

Based on Rayleigh's theory (Chapter 2.1) and Donnelly and Glaberson's (1965) experimental results, the general breakup behavior of an inviscid jet can be predicted once the perturbation growth rate and initial perturbation magnitude are known. According to Rayleigh's dispersion relationship, the growth rate can be obtained from wave number $x = 2\pi R/\lambda = 2\pi Rf/v_j$, where f is the perturbation frequency and v_j is jet velocity. Thus the growth rate is known once the jet velocity and perturbation frequency are known, we are left with the initial perturbation magnitude to determine. In the experiment setup (Fig. 13), various parameters can be controlled, such as the AC magnitude $V_{p\text{-}p}$, the separation between the jet and capacitor b, the separation of the capacitor electrodes 2a. To get a better understanding of how these parameters affect the initial perturbation magnitude, we set up a model following Canan-Calvo (1998). According to Canan-Calvo (1998), the momentum equation on the jet can be written as:

$$\frac{d}{dz}[P_g + \frac{\gamma}{\xi} - \frac{1}{2}\varepsilon_0 E^2 + \frac{\rho_l Q^2}{2\pi^2 \xi^4}] = 0 \tag{3.3}$$

where P_g is the atmosphere pressure, ξ is the jet radius under the influence of external perturbation, E is the normal electric field magnitude at the jet surface, ρ_l is the liquid mass density, and Q is the liquid volumetric flow rate. In equation (3.3), we have

assumed that the liquid is inviscid and the shear stress on the liquid- air interface can be neglected. Using $Q=\pi\,\xi^2 v_j$ and $\beta^2=\rho\xi\, v_j^2/\gamma$, equation (3.3) can be rewritten as:

$$\frac{d\xi}{\xi}=-\frac{\varepsilon_0 E\cdot(\partial E/\partial z)}{(2\beta^2+1)\gamma/\xi}dz \tag{3.4}$$

From equation (3.4) it can be see that the initial perturbation magnitude not only depends on the electric field, but also depends on the gradient of the electric field along the z direction. The electric field gradient along the z direction can be seen as the sharpness of electric field. Thus the effect of EHD perturbation depends on both the magnitude and sharpness of the electric field. The fringe electric field of a capacitor can be analytical determined (Parker, 2002) under the assumption that $2a << W << L$ (where W is the width of the capacitor and L is the length). The solution can be written as:

$$E=\frac{Vz}{2\pi(z^2+b^2)} \tag{3.5}$$

In equation (3.5), z is the vertical distance from the jet surface to the upper electrode since we only consider the initial perturbation before the jet passes through the capacitor plane. Combining equation (3.4) and (3.5) gives:

$$\tilde{\xi}=\frac{d\xi}{\xi}\propto\frac{V^2 z(b^2-z^2)}{(z^2+b^2)^3} \tag{3.6}$$

Equation (3.6) suggests that the initial perturbation magnitude is proportional to V^2. Since V is periodic $V=V_{p\text{-}p}cos(wt)$, then $V^2=V_{p\text{-}p}^2(1+cos2wt)/2$. This expression effectively cause the EHD perturbation frequency to be twice the applied AC frequency. If the applied AC frequency is f, the perturbation on the jet becomes $2f$, the

perturbation wavelength becomes $\lambda = v_j/2f$. From equation (3.6) it can also be deduced that the maximum value for $\tilde{\xi}$ is reached at z/b=0.36. At this ratio, the dimensionless perturbation magnitude scales with b^{-3}, indicating that the effectiveness of the exciter decrease rapidly as b increases. When b approaches zero, the position for maximum perturbation z also approaches zero, which means the perturbation is maximum when it is close to the blade electrode.

3.1.4 Results and discussion

Figure (14) shows the break up phenomena at different AC frequencies. In this set of images, both the nozzle and camera positions are fixed. As the frequency is swept from low to high, the effect of the perturbation on the jet break up reaches maximum at around 1.1kHz and gradually diminishes towards both ends.

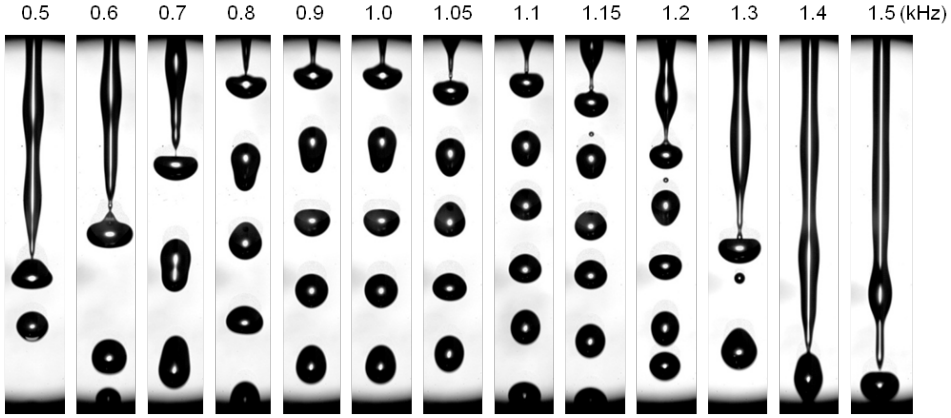

Figure 14. The breakup of ethanol jet at different driving frequencies. The gap b is 400 μm. Vp-p=330V. Jet radius is ~75 μm. Jet velocity v_j is 1.49m/s

The phenomena (Figure 14) for different perturbation freuquencies can be explanied by using Rayleigh dispersion relationship. Assume the initial perturbation magnitude is $\Delta\xi$, which is obtained from the electric field when the jet passes the excitor,

the jet surface profile as a function of vertical distance (starting from the center of the excitor) is $\xi(z)$. The evolution of the jet surface profile as a function of vertical position or time (Gonzales, 2009) is:

$$\tilde{\xi}(z) = \tilde{\xi}(v_j t) = \tilde{\xi}_0 \exp(\overline{\omega}\omega_0 t) \tag{3.7}$$

where $\tilde{\xi}(z)$ is dimensionless jet profile $\xi(z)/R$, $\tilde{\xi}_0$ is the dimensionless initial perturbation magnitude $\Delta\xi/R$, $\overline{\omega}$ is the dimensionless growth rate (as the value ω/ω_0 in the Rayleigh dispersion relationship), ω_0 is the a characteristic frequency which is defined as $\omega_0 = \sqrt{\gamma/(\rho R^3)}$, for the parameters used in this experiment, ω_0=8145 Hz. According to Rayleigh's dispersion curve, the maximum $\overline{\omega}$ is reached when the perturbation wave number $x=2\pi R/\lambda$ is close to 0.697, by setting x equal to this value, and noticing that the perturbation wavelength is related to AC frequency through $\lambda=v_j/2f$, the frequency for maximum growth rate obtained is around 1.1kHz. At this frequency, the applied perturbation will dominate the break up process. The break up point is fixed in space, one droplets are generated every half AC cycle, giving them a uniform size. To determine the droplet size distribution, we analyzed 2000 droplet from about 100 images of the high speed camera, the relative standard deviation of the droplets generated at this frequency is smaller than 1%.

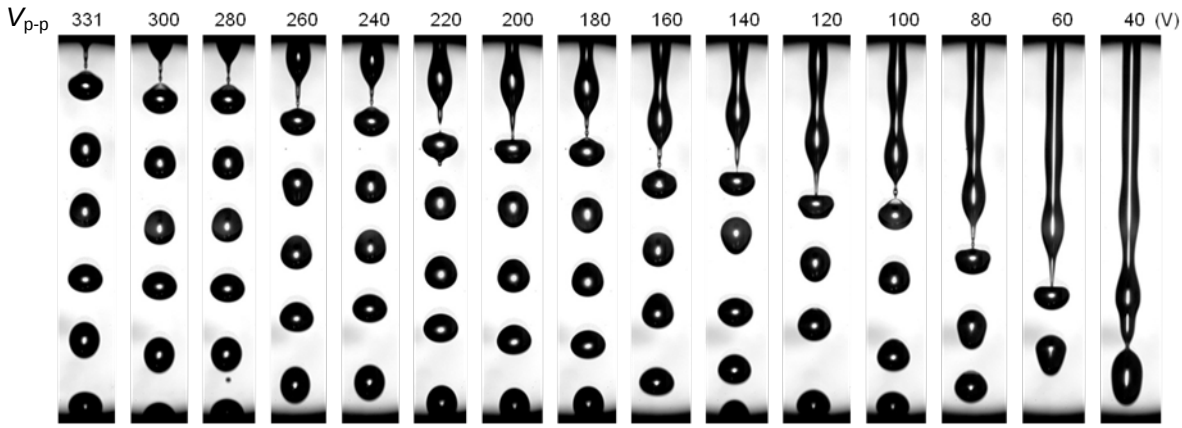

Figure 15. Jet breakup locations as a function of $V_{p\text{-}p}$ at fixed frequency. Jet radius is 75 μm. f=1.1kHz, v_j=1.49m/s

Next we investigate the perturbation effect when the AC magnitude is changed. The perturbation frequency is fixed at Rayleigh frequency (in this case 1.1kHz) where the growth rate is at its maximum. Figure 15 shows the break up position when $V_{p\text{-}p}$ is change from 331V to 40V.

As can be seen from Figure 15, the break up length increases when the AC magnitude decreases at a fixed frequency. The AC magnitude affects initial perturbation magnitude only, which is usually too small to be directly measured. The force that causes the perturbation is the norm component of the Maxwell stress at the liquid/gas interface, $\tau_e=\varepsilon_0 E^2/2$, where ε_0 is the permittivity of the vacuum, and E is the norm electric field at the interface. When electric field is present, charge will be induced on the jet surface. The charge induction and relaxation is a dynamic process, however, since the charge relaxation time (Melcher and Taylor, 1969) ($t_e=\varepsilon/K$ ~ 1 μs, where $K=10^{-4}$ S/m is the electric conductivity of the ethanol used in this work) is much shorter than the period (~1ms) of the AC electric field, the electric charge has enough time to

reach equilibrium in each cycle, the jet can be assumed to have equal potential all the time. From equation (3.7) the initial perturbation magnitude can be calculated through the break up time t, while this time can be obtained from break up length: $t = L/v_j$. The initial perturbation magnitude is then expressed as $\Delta\xi_0 = R/\exp(\omega\omega_0 L/v_j)$. Using the parameters in this experiment, R=75μm, $\overline{\omega} = \omega/\omega_0 = 0.366$, L measured from experiment, v_j calculated from the flow rate $v_j = Q/(\pi R^2)$, the initial perturbation magnitude as a function of $V_{p\text{-}p}^{\ 2}$ is plotted in Figure 16. From Figure 16 it can be seen that the initial perturbation magnitude is 4nm at $V_{p\text{-}p} = 40\,V$ and 80 nm at $V_{p\text{-}p} = 330\,V$, which are much larger than the natural initial perturbations (Lin,1998) $\Delta\xi_0/r_0 \sim e^{-12}$ ~10^{-5}, or $\Delta\xi_0$ ~1 nm. Figure 16 also verifies that the initial perturbation magnitude is proportional to $V_{p\text{-}p}^{\ 2}$.

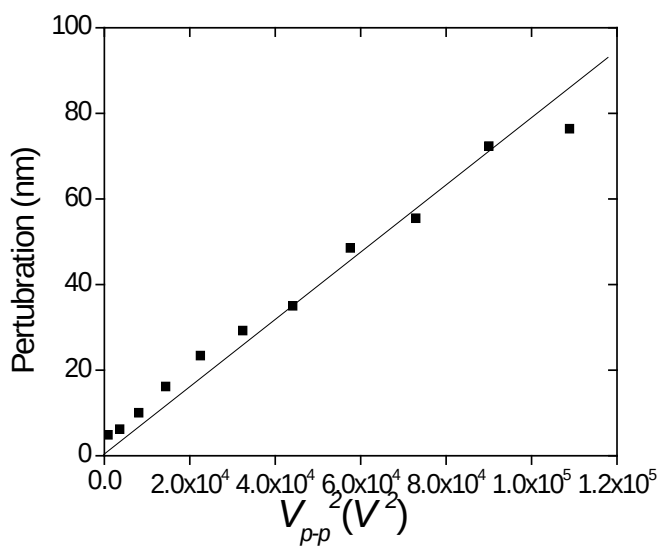

Figure 16. The linear relationship between the magnitude of initial perturbation and the $V_{p\text{-}p}^{\ 2}$ of the driving signal.

It is intuitive to expect that more intense electric fields may lead to wider range of wave number exhibiting monodispersity, because the stronger externally imposed perturbation has better opportunity to overwhelm any frequency from the background noise. To visually describe this relationship, we can plot the monodispersity islands, which is the domain of monodisperse droplet generation in the electric stress-perturbation frequency plane. Defining the Rayleigh frequency f_r as:

$$f_r = 0.697 v_j / 2\pi R \tag{3.8}$$

Under this definition, f_r corresponds to the AC frequency with highest growth rate for a charged jet and half of f_r corresponds to that for an uncharged jet. Since our jet has a floating potential, the jet surface charge is not defined. Normally the jet is uncharged, however, charge can accumulate occasionally during the operation of EHD excitation. We notice two regions that show different behaviors: near half of the Rayleigh frequency, $f/f_r \sim 0.5$, the droplets from the jet breakup are consistently and strictly monodisperse; however, near the Rayleigh frequency, $f/f_r \sim 1$, the phenomena switch between ordered breakup and random or natural breakups. Therefore, we use two different criteria for these two regions: for $f/f_r \sim 0.5$, monodispersity is defined as the possibility for droplets being the same size greater than 99.8%; for $f/f_r \sim 1$, the standard is relaxed to 95% due to the switching between ordered and random breakup. Figure 17 shows the monodispersity islands for a typical experimental configuration ($2a$= 655 µm, b= 124 µm, flow rate = 120 mL/h, and f_r=2320 Hz.). The horizontal axis in Fig.17 is normalized frequency, while vertical axis is the electric Bond number $Bo=\varepsilon_0 E^2/(\gamma/R)$, which is the ratio of electric stress to the surface tension stress. The electric field is

obtained through numerical simulations. The monodisperse islands (shadowed area in Fig.17) appear to be approximately V-shaped in the log-linear scale. The monodisperse domain starts at Bo~10^{-3} for f/f_R~0.5. When the Bo is raised to 10^{-2}, the range of wave number is increased from 0.35 to 0.6. This corresponds to 1.7× change of droplet diameter, and 5× in terms of droplet volume. The plot suggests that with the same jet diameter, the EHD exciter can effectively generate monodisperse droplets in a wide size range. Since the jet electrically floating, there is a possibility for it to obtain some charge. This charge is low and requires high external perturbation to pick it up. Due to this reason, similar trend is found for f/f_R~1, but with a smaller area of the stability island area.

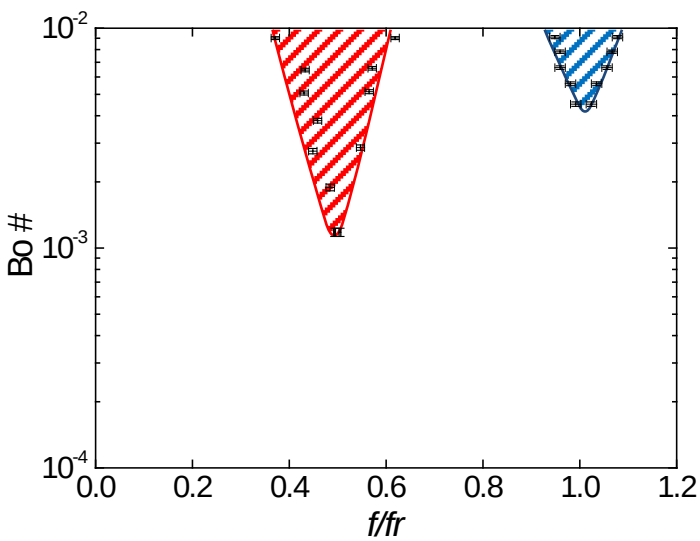

Figure 17: Monodisperse and quasi monodisperse droplet islands

3.1.5 Scale-up of the perturbation

Since the fringe field of the chopper is essentially two dimensional, the same chopper can

be applied to multiple jets. We machined a four-nozzle linear array using a precision drilling and milling process out of aluminum (Lojewski *et al.*, 2013) (Fig.18a). The nozzles have equal spacing of 500 μm and produce four nearly identical jets (Fig. 18b). The exciter is placed near the exit of nozzles, with the exciter plane perpendicular to the linear array and the edge parallel to the jet array. This demonstrates that the EHD exciter is a scalable device that can operate on multiple jets for generating strictly monodisperse micro droplets at high throughput.

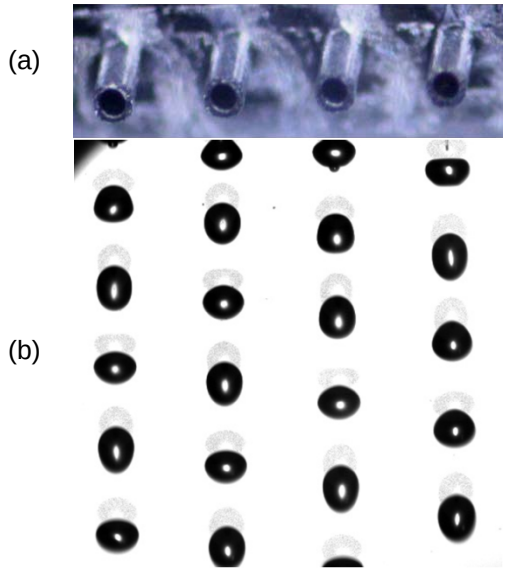

Figure 18. Multiple jets that experience transverse perturbation by the same capacitor. (a) The manifold of four nozzles (nozzle spacing: 500 μm; nozzle OD=200μm, ID=100μm); (b) breakup after the transverse perturbation is applied. Note the absence of satellite droplets in all four jet breakups.

3.2 EHD excitation on charged liquid jet with in-plane configuration

3.2.1 Experimental Setup

For charged jet perturbation, the 1st generation EHD exciter (Figure 13) has its limitations. The jet will either skew to one side which brings complexity to analysis or

be interrupted entirely if it touches the capacitor. The experimental setup for EHD perturbation on a charged inertia jet (2nd generation EHD exciter) is shown in Figure 19. The liquid used in the experiment is pure ethanol. Liquid is pressurized from a 30 gauge stainless steel needle (inner diameter 150µm, outer diameter 300µm) using a high pressure syringe pump (ME-300, New Era Pump Systems, Inc., not shown in Figure) which is capable to operate under a constant flow rate from less than 1ml/hr to hundreds of ml/hr.

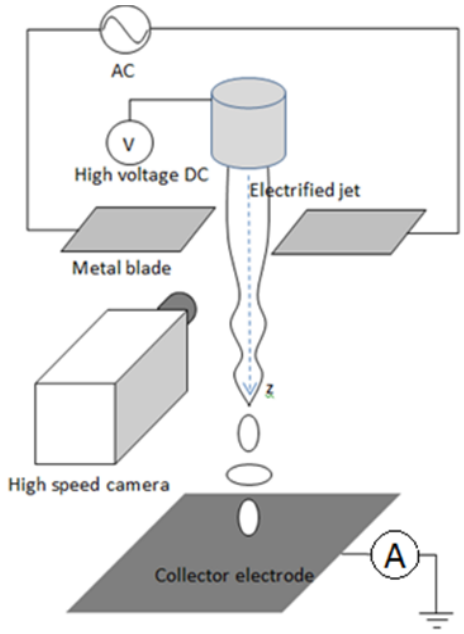

Figure 19. Experimental setup for electrified jet under electrohydrodynamic perturbation

The syringe needle is connected to a high voltage power supply (Acopian, USA) which has continuous output from 0 to 15kV. Jet surface charge can be tuned by adjusting the applied voltage (typical voltage used is from zero to a few hundred volts).

The perturbation is introduced by the electric field in a small gap between two sharp razor blades on the same plane. We place the two blades symmetrically at both sides of the jet to keep it straight as the jet passes through them. Each blade is mounted on an *x-y-z* linear stage for precise gap adjustment. The two blade electrodes are connected to an amplified AC signal source (ATF 20B, ATTEN Instruments) with adjustable $V_{p\text{-}p}$ from 0 to 300V. At 15 mm below the blade electrodes, a grounded electrode is used to collect the generated droplets. An ampere meter is connected between the collector electrode and ground for current measurement, which will reveal the information of jet surface charge density. The phenomena were recorded with a high speed camera (Phantom v12.1, Vision Research) coupled with a microscope with 1×, 2× or 4× magnification. The camera has a maximum speed of 1,000,000 pictures-per-second and resolution 5 microns/pixel. A collimated LED light source (not shown in Figure) is placed behind the jet and pointing to the camera to form a shadowgraph configuration.

Plenty of parameters can be adjusted in the jet EHD perturbation experiment based on the current setup. From the jet point of view, these parameters include flow rate, liquid viscosity, surface tension, conductivity and surface charge density; from the perturbation point of view, they include the perturbation magnitude, perturbation waveform and frequency. It is found that the most important parameters are jet charge level and perturbation frequency; these two parameters determine the initial perturbation magnitude and growth rate. The experiment is first conducted at a fixed jet charge level and sweeping the perturbation frequency from 0 to a value high enough that the perturbation loses effect, the charge level is then changed for next round of

frequency sweeping. The charge level on a jet cannot be increased infinitely, above a certain charge level ($\Gamma > 1.5$), which corresponds to Rayleigh limit (Rayleigh, 1882), a steady initial jet cannot be maintained, the charge level in our experiment thus stops at that value.

3.2.2 Theoretical Development

3.2.2.1 Surface Charge Density on the Jet

The jet surface charge plays an important role in the EHD perturbation, which not only determines the dispersion relationship but also affects the initial perturbation magnitude; it is directly related to the potential applied to the needle. The problem of electric field inside a coaxial cable is very similar to the problem considered here. Consider the coaxial configuration where the jet has a potential V_0 and the outer cylindrical wall with radius R_0 has potential 0, and assume both the jet and the cylindrical wall are infinitely long. Between the jet and the cylindrical wall the potential is described by Laplace equation:

$$\begin{aligned} &\Delta V = 0 \\ &V(r = R) = V_0 \\ &V(r = R_0) = 0 \end{aligned} \tag{3.9}$$

The solution of the electric potential inside the coaxial configuration is:

$$V = \frac{V_0 \ln \frac{r}{R_0}}{\ln \frac{R}{R_0}} \tag{3.10}$$

The surface charge density can be found according to Gauss's law:

$$\sigma = -\varepsilon_0 \frac{\partial V}{\partial r}|_{r=R} = -\frac{\varepsilon_0 V_0}{R \ln \frac{R}{R_0}} \tag{3.11}$$

According to equation (3.11), the surface charge density is proportional to the potential applied to the jet. In our problem, we assume the jet surface charge can be expressed as $\sigma = CV_0$, where C is a geometrical factor related to the electrode configuration around the jet. Figure 20 shows the voltage and surface charge relationship measured in a typical experiment, the surface charge density is obtained by measuring the current carried by the jet, which are related through:

$$\sigma = I / 2\pi R v_j \tag{3.12}$$

In Figure 20, the theoretical prediction using $\sigma = CV_0$ is also plotted, where C is chosen to best fit the data. Figure 20 shows that the existence of the EHD perturbation has negligible effect on the surface charge density on the jet. Experiment verified that the change of EHD frequency and magnitude has negligible influence on the surface charge density as well (Figure 21).

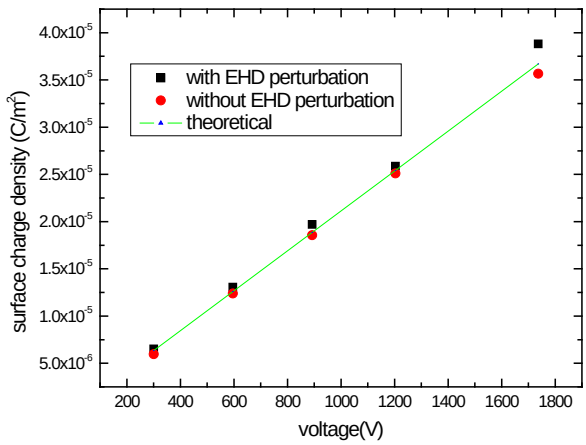

Figure 20: Surface charge density vs. jet voltage

Keep increasing the jet potential, the charge density eventually becomes too high and reaches Rayleigh limit (Rayleigh, 1882), which is characterized by much thinner jet eruption from the main jet. In this case, the current measured could be much higher than the linear prediction due to the thinner jet eruption; such a process is similar to the Taylor cone-jet generation and is a separate subject of study.

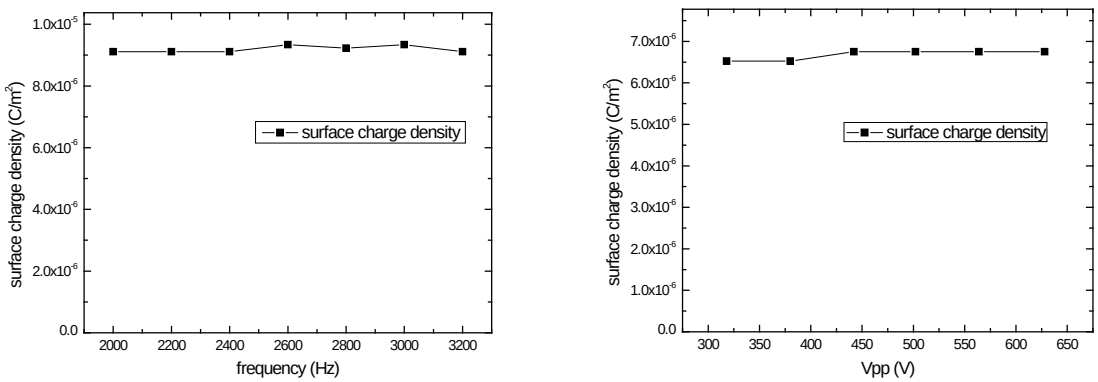

(a) (b)

Figure 21: (a)Surface charge density vs. EHD frequency (Q=120ml/hr, V_{jet}=512V, $V_{p\text{-}p}$=500V, R=75μm) and (b) Surface charge density vs. $V_{p\text{-}p}$ (V_{jet}=300V, Q=120ml/hr, f=2400Hz, R=75μm)

Equation (3.11) suggests that the surface charge density is only dependent on the jet potential, jet radius and the outer cylindrical wall radius (or geometric factor C). The parameters from the EHD perturbation do not affect the surface charge density, which is verified in Figure 21 and Figure 22, where the surface charge density is not affected by the EHD frequency and voltage. As the blade approaches the jet surface, the jet experiences a larger perturbation and the break up length is reduced, the surface charge density will increase at the same time due to the increase of geometric factor C. However this increase is not significant, and can be neglected unless the blade is very close to the jet surface. Figure 22(b) shows the surface charge density change when the jet-blade distance is changed.

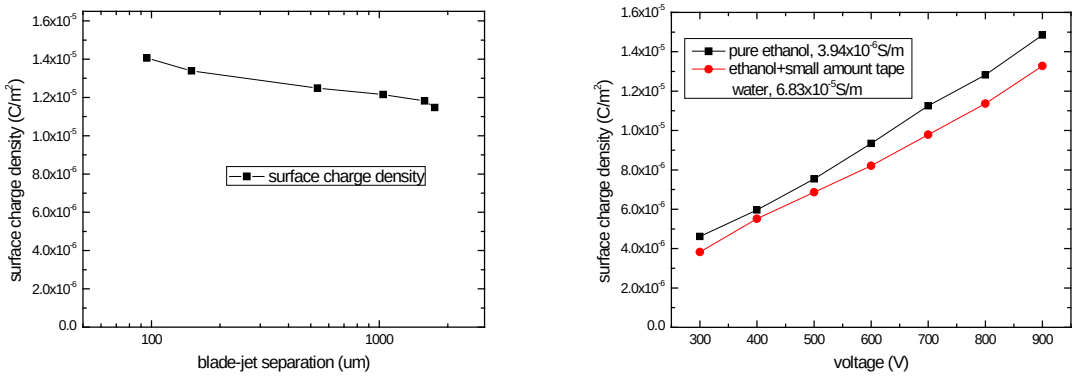

Figure 22: (a) Surface charge density vs. blade-jet separation ($V_{p\text{-}p}$=538V, V_{jet}=464V, Q=120ml/hr, R=75μm) and (b) surface charge density vs. jet voltage for two different liquids. (Q=120ml/hr)

To further test the validity of equation (3.11), liquids with different conductivity is also used. Based on equation (3.11), the conductivity should not affect the surface charge density. Small amount of tape water is added to pure ethanol in order to change the conductivity and keep other liquid properties relatively unchanged. The tape water

added ethanol has a measured conductivity of 6.83×10^{-5} S/m while the pure ethanol has a conductivity of 3.49×10^{-6}S/m. The jet voltage-surface charge relationship is plotted in Figure 22(b). After adding tape water, the conductivity of ethanol is increased by 20 times, but the surface charge density has a change smaller than 10%. The reduced surface charge density is probably due to the faster charge relaxation at higher conductivity; however this reduction is not significant even when the conductivity has 20 times increment. To sum up, the linear prediction of equation (3.11) can be safely applied for a wide range of liquid conductivity.

3.2.2.2 Initial Whipping Magnitude

Unlike the uncharged jet, the initial whipping perturbation for a charged jet can be directly measured for low perturbation frequencies due to its large magnitude. Figure 23 shows the measurement of the initial whipping magnitude in experiment, which is taken as the jet position deviation from the jet's initial center line in half the AC cycle.

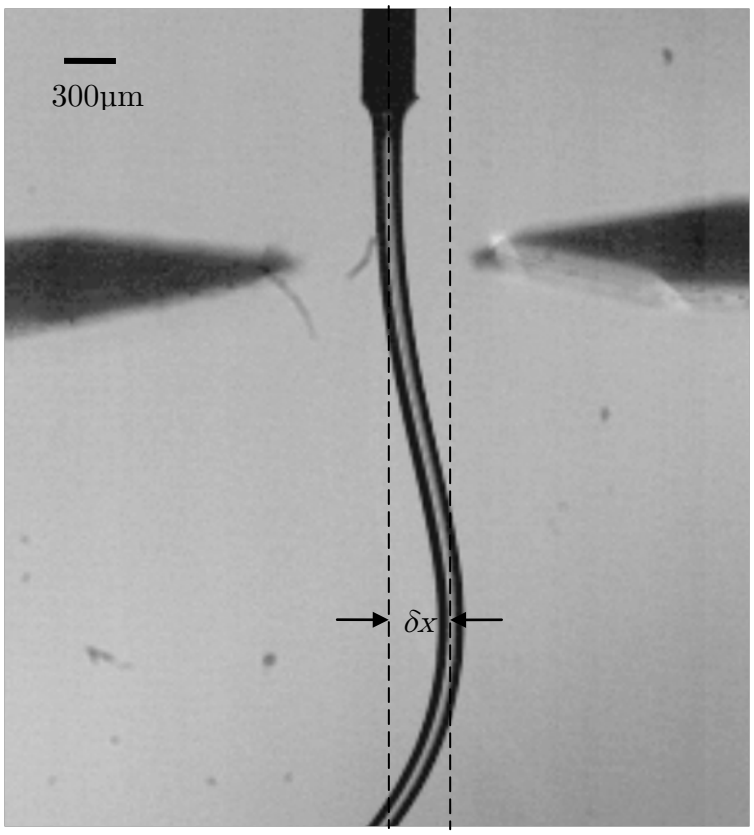

Figure 23. Measurement of the jet initial whipping magnitude δx

The initial whipping magnitude of the jet is approximated by the displacement of a circular liquid segment under half a cycle of the accelerating AC field and compared with experiment. As will be shown, such an approximation proves to be acceptable. Without the jet, the horizontal electric field at the center vertical line of the gap is (full derivation can be found in Appendix B):

$$E_x = 2V_{ac} / \pi a \sqrt{1 + (\frac{z}{a})^2} \tag{3.13}$$

The electric force per unit length is expressed as: $F_x = 2\pi R \sigma E_x$. Consider a differential liquid cylinder with radius R and length dy passing through the blade gap, its mass

$dm = \rho\pi R^2 dy$ and electrical force $F_x \cdot dy$, this cylinder will be accelerated horizontally. Other forces are the surface tension force, which tries to stabilize the jet and counteract the swinging, and the Coulomb repelling force from other parts of the jet. According to Reneker (2007), the surface tension force per unit length on the differential cylinder is:

$$F_s = -\pi R\gamma \,|\, k \,|\, \hat{n} \tag{3.14}$$

where k is the curvature of the bending jet, $\hat{n}$ denotes the direction which is normal to the unbent jet axis and points to the direction of bending, the negative sign here means surface tension acts in the opposite direction of bending. The Coulomb repelling force from other parts of the jet on the liquid element (Reneker, 2007) is:

$$F_c = \frac{\pi R^2 \sigma^2}{\varepsilon_0} \ln \frac{L}{R} \,|\, k \,|\, \hat{n} \tag{3.15}$$

where L is the cut-off length for integral which is of the same order of R.

Noticing that the surface tension force and Coulomb force from other parts of the jet linearly depends on the jet bending curvature $|\, k \,|$. At the initial stage of the jet bending, $|\, k \,|$ is very small and can be ignored; only the electric force is of importance. Newton's second law reads:

$$F_e \cdot dy = dm \cdot \frac{Du}{Dt} = dm \cdot \left(\frac{\partial u}{\partial t} + u\frac{\partial u}{\partial x} + v\frac{\partial u}{\partial y}\right) \tag{3.16}$$

where u is the jet horizontal velocity as a consequence of the electric force acceleration and v is the jet vertical velocity. Since u is small compared with v, the term $u\frac{\partial u}{\partial x}$ can be ignored, and noticing $v\frac{\partial u}{\partial y} = \frac{\partial y}{\partial t}\frac{\partial u}{\partial y} = \frac{\partial u}{\partial t}$, equation (3.16) reduces to:

$$a_x = \frac{\partial u}{\partial t} = \frac{F_e}{2\rho\pi R^2} = \frac{\sigma E_x}{\rho R} \tag{3.17}$$

Define the initial perturbation δx as the horizontal displacement of the jet during half the AC cycle $1/2f$ as it passes through the blade gap, noticing $V_{ac} = V_{pp}\sin(2\pi ft)$ and $z = vt$, it can be obtained by integrating Equation (3.17):

$$\begin{aligned} \delta x &= \int_0^{1/2f}\int_0^t a_x dt' dt \\ &= \int_0^{1/2f}\int_0^t \frac{2\sigma V_{pp}\sin(2\pi f t')}{\pi a \rho R\sqrt{1+(\frac{vt'}{a})^2}} dt' dt \end{aligned} \tag{3.18}$$

From Equation (3.18) one observes that the initial perturbation magnitude is proportional to jet potential and AC magnitude, inverse proportional to jet radius. The relationship between the initial perturbation magnitude and AC frequency is more complicated, generally, at lower frequency, the jet is accelerated for a longer time and thus obtains larger initial perturbation magnitude. As the jet travels downstream, the acceleration for the same liquid segment gets smaller and smaller. If the AC frequency is large enough, the spatial change of the liquid segment can be ignored during *1/2f*, and the initial perturbation is inverse proportional to frequency square. Figure 24 shows the numerical results of equation (3.18) by taking V_{pp}=300V, σ =4.37x10^{-5}C/m^2, R=75μm, v=1.52m/s, a=1494μm, ρ=800kg/m^3 ; comparison with experiment data is also shown.

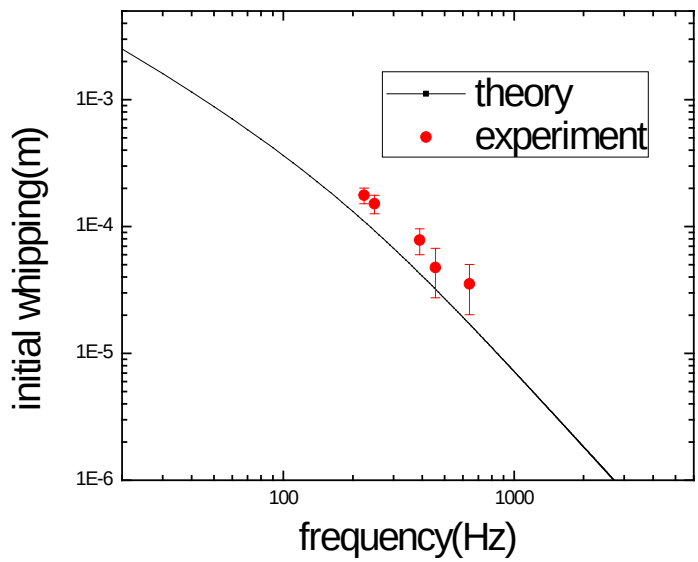

Figure 24: Initial perturbation magnitude vs. perturbation frequency (Vpp=300V, σ=4.37x10-5C/m2, R=75μm, v=1.52m/s, a=1494μm, ρ=800kg/m3).

3.2.3 Results and discussion

3.2.3.1 Basic phenomenology

We begin with showing basic phenomena for inertia jet that are intuitive to understand, with perturbation frequency set at Rayleigh frequency (i.e. largest growth rate for varicose instability). We first adjust $V_{p\text{-}p}$ at a fixed blade separation and vertical location for the exciter. Figure 25(a) and (b) shows that for more intense initial excitation caused by higher $V_{p\text{-}p}$, the breakup length is reduced, since it needs less time to develop from larger initial perturbation to a perturbation which is equal to the jet radius.

The magnitude of initial excitation can also be changed by varying the blade separation. For the same $V_{p\text{-}p}$, smaller blade separation gives rise to higher excitation magnitude and stronger initial perturbation, which leads to shorter break up length (Figure 25(c), (d)).

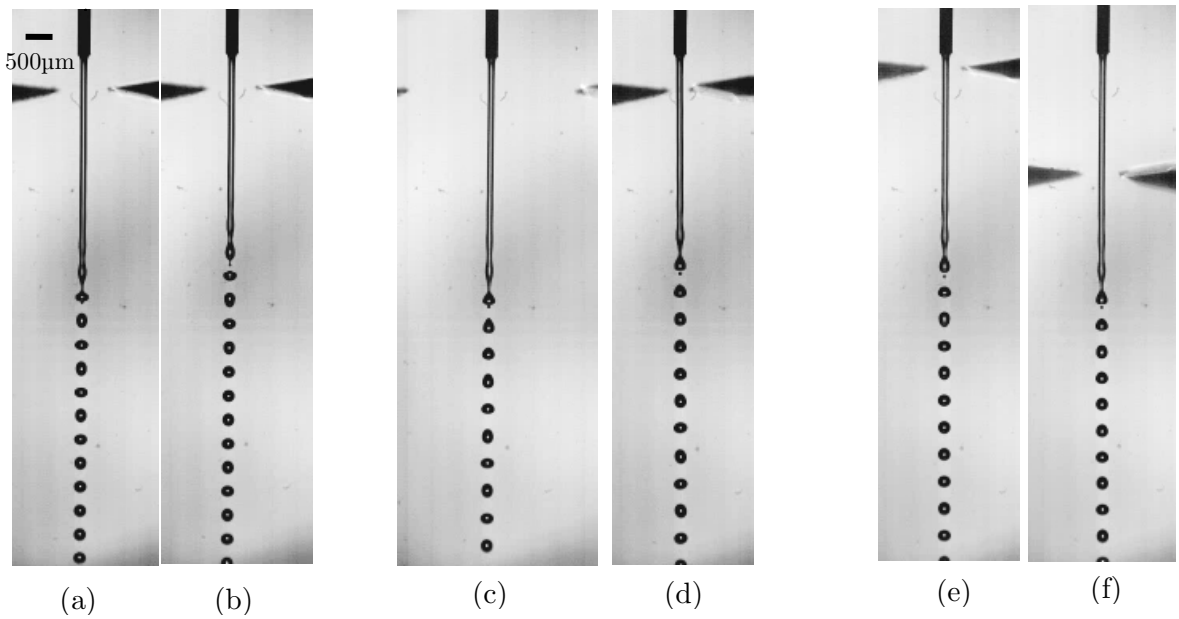

Figure 25: Jet breakup length difference when changing V_{pp}: (a) V_{pp}=204V, (b) V_{pp}=660V; Changing blade separation (c) 3.90mm (d) 0.48mm and changing blade height (e) blade at the beginning of the jet (f) blade at the midway of the jet. Q=120ml/hr, f=2320Hz, V_{jet}=500V, V_{pp}=744V.

When the blade is positioned vertically further away from the nozzle exit, the EHD perturbation is still capable to cause the jet to break up into monodispersed droplets (Figure 25(e), (f)). The difference in the heights of blades is the position of the peak AC electric field. If the blades are put at a higher position, the peak electric field also moves up and so the initial perturbation is stronger, which will lead to earlier breakup (Figure 25(e), (f)).

3.2.3.2 Frequency response for different charge levels

As shown in Section 2.3, the dispersion relationship for a charged inviscid jet largely depends on the charge level. For low charge level, only varicose instability exists; for high charge level, whipping instability is coexistent with varicose instability. The phenomenology of EHD perturbation under different charge levels and wave number is shown in this section.

For uncharged jets, the whipping mode is stable, which is predicted by Rayleigh (Eq. 2.4) and Chu's (Eq. 2.8) dispersion relationships and represented by a straight stream shown in Figure 26(a). Small amount of charge is induced by the AC field on the jet, as discussed previously, the perturbation force can be written as: $F \sim \varepsilon_0 E_{ac}^2 \sim \varepsilon_0 (V_{pp} \cos wt)^2 \sim \frac{\varepsilon_0 V_{pp}^2}{2}(1+\cos 2wt)$. The perturbation has a frequency that is twice of the applied AC frequency, so the most "effective" perturbation frequency is reduced by half compared to a jet with moderate charge density. Crowley (1982) first noticed the effects of Fourier components of the applied field. Duan (2013) studied the response of an electrically floating jet to EHD perturbations and obtained operation islands for "monodisperse" and "quasi-monodisperse" droplet generations. We can compare the charge density which is caused by the DC power supply (σ) with that induced by the AC field ($\varepsilon_0 E_{ac}$). If $\sigma > \varepsilon_0 E_{ac}$, the primary frequency ω has a more important effect, if $\sigma < \varepsilon_0 E_{ac}$, the frequency 2ω will be dominant.

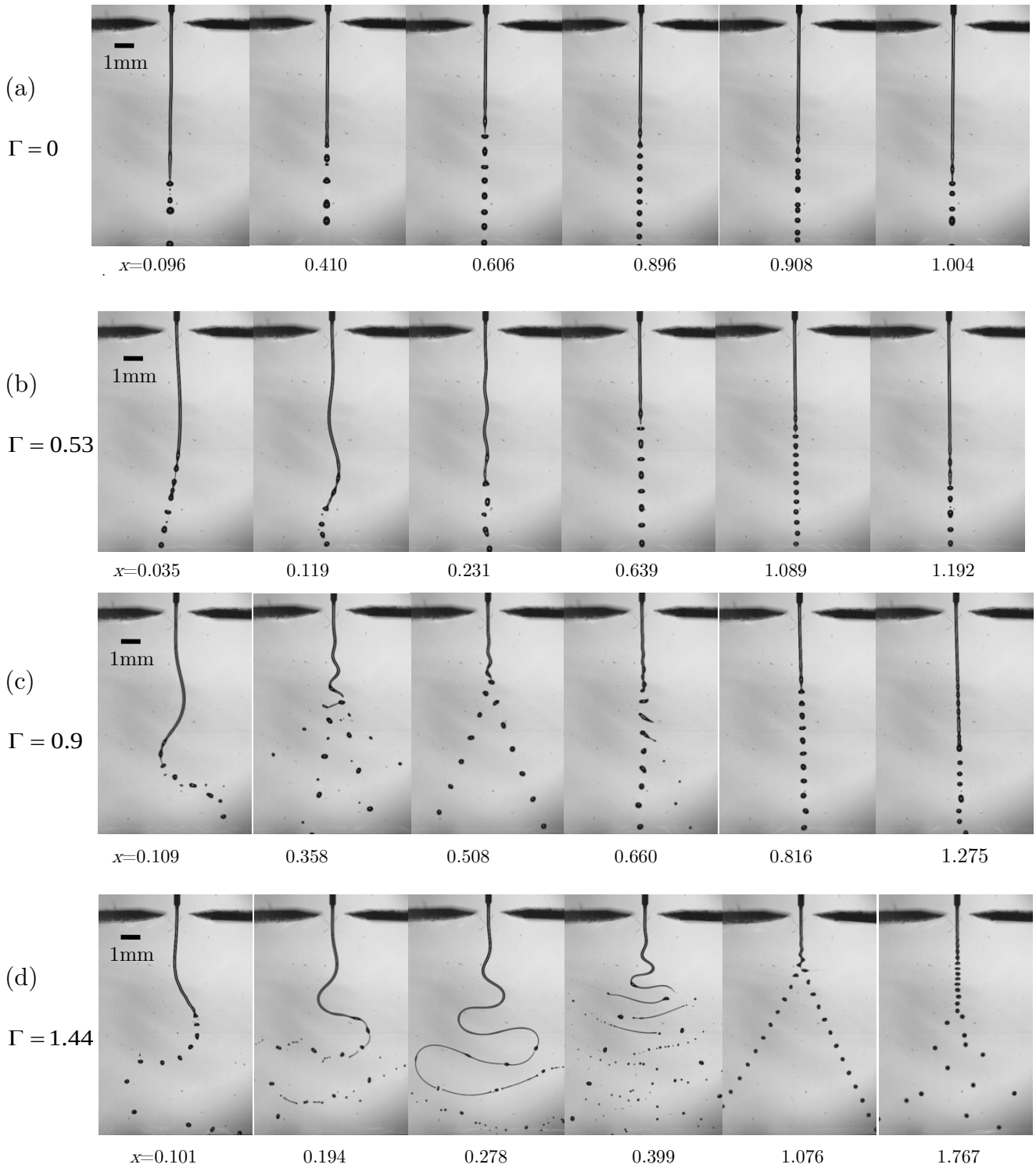

Figure 26: Frequency response of charged jet at different charge levels and perturbation wave numbers. The dimensionless charge level $\boldsymbol{\Gamma}$ is defined as the ratio of electric stress to surface tension of the jet, i.e. $\boldsymbol{\Gamma}=\boldsymbol{\sigma}^2 R/\boldsymbol{\varepsilon}_0\boldsymbol{\gamma}$, with $\boldsymbol{\varepsilon}_0$ being vacuum permittivity.

The dispersion relationship (Equation (2.8)) for $\Gamma = 0$ is shown in Figure 9(a). Typically, wave number x is related to the applied EHD frequency f through $x = 2\pi Rf / v_{jet}$ with v_{jet} being the jet axial velocity and surface charge density σ is related to the measured current i through $\sigma = i / 2\pi R v_{jet}$. However, when the induced charge on the jet is dominant over the DC charge, the actually perturbation is 2*f*, so the wave number should be expressed as $x = 4\pi Rf / v_{jet}$. As shown in Figure 26(a), when perturbation wave number is low (x=0.096), the growth rate for the prescribed perturbation is too low to compete with the natural perturbation which has a wide frequency range, the jet behaves as if no perturbation is applied. As the perturbation wave number is increased (x=0.41), so is the growth rate, the jet break up will be earlier, but the position of the break up point and the size of the resultant droplets are still not fixed, due to the competing effect of the natural perturbation. Keep increasing the frequency (x=0.606 and 0.896), the break up becomes uniform with fixed break up length and droplet size. The wave number range for this phenomena brackets x_R=*0.697*. Keep increasing the wave number and make it below 1 (x=0.908), the break up is no longer uniform, but still earlier than the natural break up since the prescribed perturbation under this wave number is still unstable. When the perturbation wave number exceeds 1 (x=1.004), it lost its effectiveness and the break up goes back to the natural situation.

At a low charge level, the jet gets an initial whipping magnitude which can be estimated by equation (3.18). This initial whipping may grow or may not depending on the perturbation wave number, as is shown in Figure 9(a) for a charge level of 0.53. The

experimental phenomena for Γ=0.53 is shown in Figure 26(b). At low perturbation wave number (x=0.035), the jet appears to be swinging and natural break up sets in before a complete AC cycle finishes. Increasing the wave number (x=0.119), the jet can exist for longer than an AC cycle and the whipping magnitude increased slightly due to the small whipping growth rate. (x=0.231) shows the initial whipping magnitude does not grow, as is predicted by the dispersion curve (Figure 9(b)). (x=0.689) and (x=1.089) shows the Rayleigh mode, when the perturbation wave number brackets the maximum growth rate for varicose instability. The break up details in Figure 26(b) (x=0.689 and x=1.089) fall in the rear-merging zone analyzed by Pimbley and Lee (1977), where the neck between two swells form a satellite droplet which is subsequently absorbed by its upper droplet as they travel downstream. At this range, the whipping growth rate vanishes, so the jet appears to be straight. (x=1.192) shows the vanishing effect of the perturbation when the wave number is larger than the varicose perturbation cutoff value, the break up is similar to natural break up.

At relatively larger charge level, both the whipping growth rate and unstable wave number range is enlarged as shown in Figure 9. The experimental phenomena for Γ=0.9 is shown in Figure 26(c). In Figure 26(c), (x=0.508) is most interesting because the jet breaks up into two monodisperse droplet streams. We call it the shearing mode because it looks as if the jet is torn apart by the AC field. In each AC cycle, the shearing mode gives two droplets, as opposed to the Rayleigh mode, where only one droplet is generated in each AC cycle. The generated droplet spins due to the non-axisymmetric break up as it travels downstream. (x=0.660) shows the phenomena

between shearing mode and Rayleigh mode, where the non developing initial jet whipping causes a zigzag jet shape, which breaks up at the same frequency as the AC perturbation. Coulomb fission (Gomez, 1994; Duft, 2003; Smith, 2002) usually happens as the liquid ligament recoils to reduce the surface area and increase the charge level. The formula of the Rayleigh limit $q=8\pi(\varepsilon_0\gamma r^3)^{1/2}$ suggests that when two identical droplets charged at β time of the Rayleigh limit merge, the newly formed droplet will have a new and increased charge level of $2^{1/2}\beta$ of the Rayleigh limit. When $2^{1/2}\beta$ is close or greater than unity, as is in Figure 26(c) (x=0.66), the newly formed droplet would immediately experience Coulombic fission, shedding small daughter droplets to bring the charge level of the main droplet below the Rayleigh limit of the droplet.

At a charge level close to Rayleigh limit of a liquid column, whipping instability can be dominant for certain wave numbers. The dispersion curve for Γ=1.44 is shown in Figure 9 and the experimental phenomena is shown in Figure 26(d). During the development of whipping instability, the jet is stretched and thinned in order to conserve mass. (x=0.101) shows natural break up happens before whipping has enough time to stretch the jet. (x=0.194 and 0.278) shows how the jet is stretched and thinned as whipping growth rate is large. The thin liquid ligament breaks up to multiple of "satellite" droplets between two main droplets. (x=0.278) is similar to "beads on string" fiber configuration commonly seen in electrospinning (e.g., Fong, 1999). Keep increasing the wave number(x=0.399), the break up becomes ordered in a way that each AC cycle generates two main droplets with a thin ligament in between them (which subsequently breaks up into multiple satellite droplets). The ligament becomes shorter as the wave

number increases. Finally the ligament vanishes and "shearing mode" is reached. Coulomb fission is observed at "shearing mode" for high charge levels, where the primary droplet ejects out progeny droplets to reduce its surface charge. The growing of whipping instability causes uneven velocity distribution and high surface curvature when it breaks up. As a consequence of high charge level and high surface curvature, charges accumulate locally and eventually caused the Coulomb fission.

3.2.3.3 Breaking up details

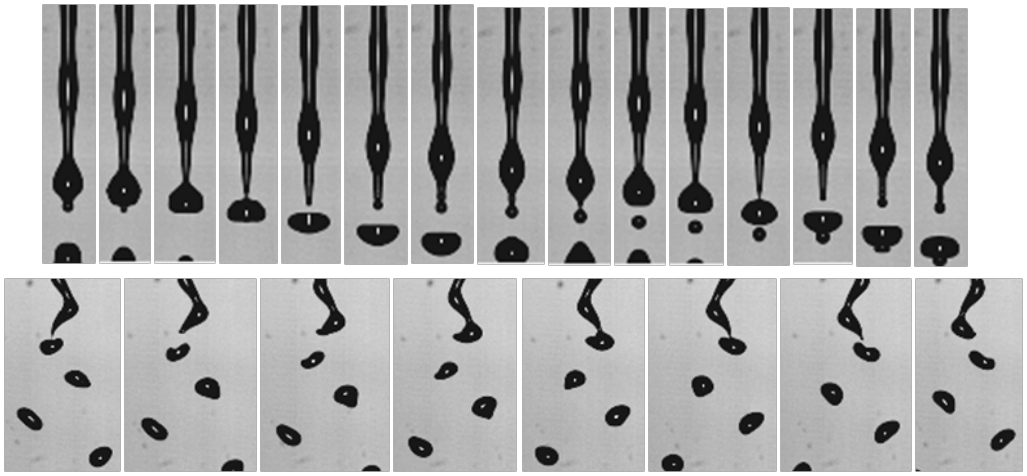

Figure 27: breaking up details.(Upper row: Rayleigh mode, interval between images: 62.5 µs. Lower row: Shearing mode, interval between images: 61.68 µs.)

The breaking up details are recorded by high speed camera and shown in Figure 27. As predicted by the nonlinear theory (Yuen, 1968) and observed by other researchers (e.g. Donnelly and Glaberson,1965), the breakup of Rayleigh mode is usually accompanied by satellite droplet formation. However, we observed during the breakup of the shearing mode, satellite droplet are usually not observed. To fully understand the physical

process of the breakup of shearing mode, one has to turn to nonlinear analysis which is not the main focus of this study.

CHAPTER 4. EHD PERTURBATION ON A FLOW FOCUSED JET

The size of the inertia jet is usually restricted due to wall resistance (pressure required is inverse proportional to jet diameter raised to the 4th power). Ganan-Calvo (1997) invented the flow focusing device which effectively eliminates the wall resistance and generates a jet with much smaller diameter (down to a few microns). In this chapter, a scalable flow focusing device inspired by (Ganan-Calvo, 1997) is established and subject to the EHD perturbation. Our new flow focusing design with EHD perturbation generates small droplets with uniform size and can be easily multiplexed. In this chapter, we first introduce the generation of the flow focused jet and then discuss the scalable flow focusing device including operation criteria and the EHD perturbation on it.

4.1 Generation of a flow focused jet

To generate droplet of micro meters size, one can employ a typical pneumatic spray device (e.g. Lee, 2013), which uses high pressure gas to force the liquid through a specially designed nozzle. At the exit of the nozzle, the liquid first form a sheet, which subsequently breaks up to threads and droplets under Kelvin-Helmholtz instability (Miles, 1959). Droplets generated this way typically has a wide size distribution. If a micro meter sized jet can be generated, the jet will break up under Rayleigh instability and forming droplets with relatively narrow size distribution. Moreover, under EHD perturbation, the droplet size distribution can be further narrowed through the controlling of the break up process.

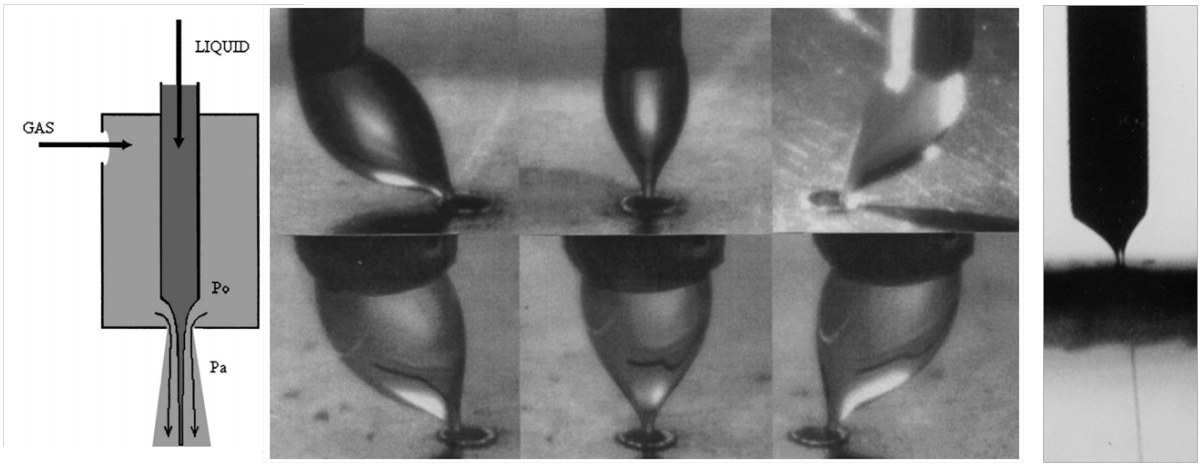

(a) (b) (c)

Figure 28: (a) Schematic of the flowing focusing device. (b) Jet formation inside the chamber (c) Overall view of jet formation (Ganan-Calvo, 1997)

The flow focusing micro-jet generator, which was first reported by Canan-Calvo (1997), can successfully generate a stable jet with diameter from below one micro meter to tens of micro meters. This device uses the highly accelerated coflowing gas stream to stretch the meniscus hanging on needle tip into a jet, which eliminates the solid-liquid friction and greatly reduces the achievable jet size. Figure 28(a) shows the working principle of the flow focusing device; liquid is fed in slowly through a needle (OD ~ 300µm), part of the needle is enclosed in a chamber with the lower end a few hundred microns above the small orifice outlet. Gas is fed in through a side wall, which only exits the orifice at the bottom of the chamber. Under suitable liquid flow rate Q and gas pressure drop ΔP (the pressure difference between inside the chamber and at the orifice), a micro jet is formed (Figure 28(c)) under the influence of the high speed flow at the exit of the chamber, this jet then breaks up and generate quasi-monodisperse droplets with size close to the jet size.

Figure 28(b) is an illustration of the stableness of this device (Ganan-Calvo,1997). Even when the orifice and the needle are not aligned, a cone and jet can still be generated. If there is any turbulence in the gas flow, the generation of a jet is only interrupted temporary, once the gas flow is restored, the cone jet will be re-established.

Two important characteristics of the flow focusing device are summarized below:

(1) The gas Weber number We should satisfy $1<We<40$ for straight jet generation.

The gas Weber number is defined as: $We = \frac{\rho_g v_g^2 d}{\gamma}$, where ρ_g is the gas density, v_g is gas velocity at the jet surface, d is jet diameter, γ is the liquid-gas interfacial tension. $We>1$ is necessary for the generation of the jet, otherwise the stretching effect of gas flow is not strong enough compared with the surface tension which tries to pull the liquid back. $We<40$ ensures that the non-symmetric perturbation does not grow, so the jet keeps straight and breaks up symmetrically, which makes analysis simpler and improves monodispersity of the generated droplets (Ganan-Calvo,1997).

(2) The jet size is determined by Q and ΔP

The jet size d_j can be expressed (Ganan-Calvo,1997) as:

$$d_j \approx \left(\frac{8\rho_l}{\pi^2 \Delta P_g}\right)^{1/4} Q^{1/2} \tag{4.1}$$

where ρ_l is the liquid density, ΔP_g is the pressure drop from inside the chamber to the orifice outlet, Q is the liquid flow rate. This expression signifies that to reduce the jet size, the flow rate should be reduced. However, jet flow rate cannot be reduced

indefinitely, there is a minimum flow rate below which the surface tension effect is too strong due to the large surface curvature and the jet could not be formed.

4.2 Experimental setup of EHD perturbation on a scalable flow focused jet

The experiment setup by Ganan-Calvo (Fig. 28) used a circular orifice as flow outlet, which is difficult to multiplex and introducing EHD perturbation. In our experiment, a narrow slit is used as flow outlet. The experimental setup is shown in Figure 29.

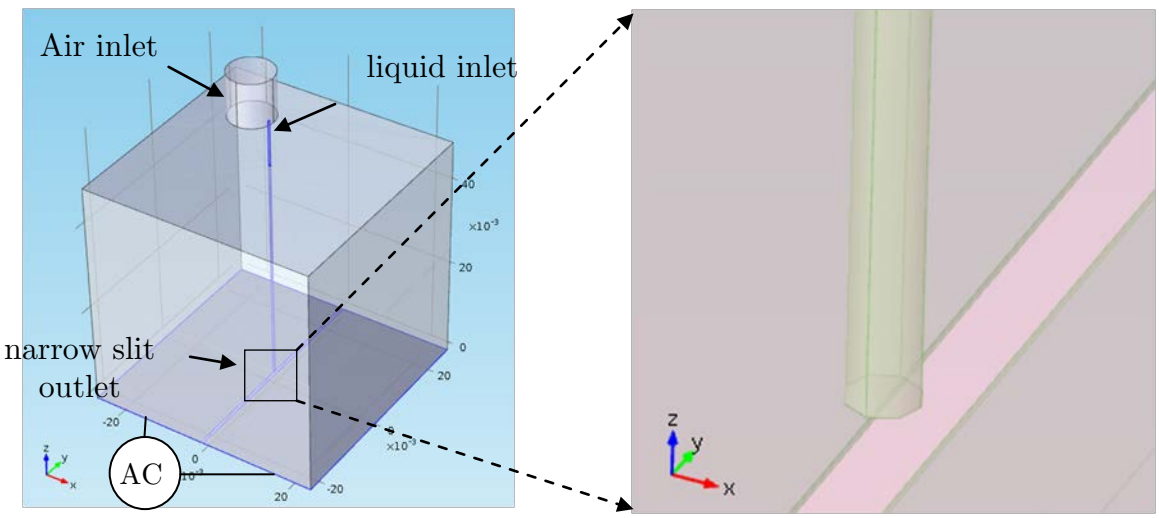

Figure 29: Experimental setup for flow focused jet EHD perturbation

In Figure 29, a nozzle is inserted into the chamber for liquid supply. The connection part is well sealed to avoid air leak. An opening at the upper wall of the chamber is used for air inlet and a narrow slit opening at the bottom of the chamber is the air and liquid outlet. The nozzle is typically placed a few hundred micro meters above the slit outlet. The bottom wall of the chamber is made of two metal plates which are connected to amplified AC voltage for introducing EHD perturbation. At suitable operating parameters (to be discussed later), the shear force and pressure drop caused

by the gas flow will stretch the liquid meniscus into a jet which easily reaches a few microns in size due to the elimination of wall resistance. This device can be easily multiplexed by placing multiple nozzles along slit direction.

4.3 Theoretical development

4.3.1 Flow field inside the chamber

Understanding the flow field inside the chamber is crucial to the designing of the device. The gas flow field for the flow focusing device can be analytically determined, using the conformal mapping method similar to the electric field calculation in Chapter 3. In this analysis, the chamber is assumed to be infinitely long and wide, thus the bottom walls of the chamber is made up of two semi-infinite plates. The needle above the center of the two semi-infinite plates is assumed to have negligible effect on the flow field. Under these assumptions, the equations describing the potential flow are:

$$\begin{aligned} &\nabla^2\psi = 0 \\ &\psi = \mp Q/2 (x = \pm a) \\ &u = \frac{\partial\psi}{\partial y}, v = -\frac{\partial\psi}{\partial x} \end{aligned} \tag{4.2}$$

where ψ is the stream function, Q is the flow rate, a is half the gap width, u and v are flow velocity in the x and y direction . Figure 30 shows 2D simplification of this problem:

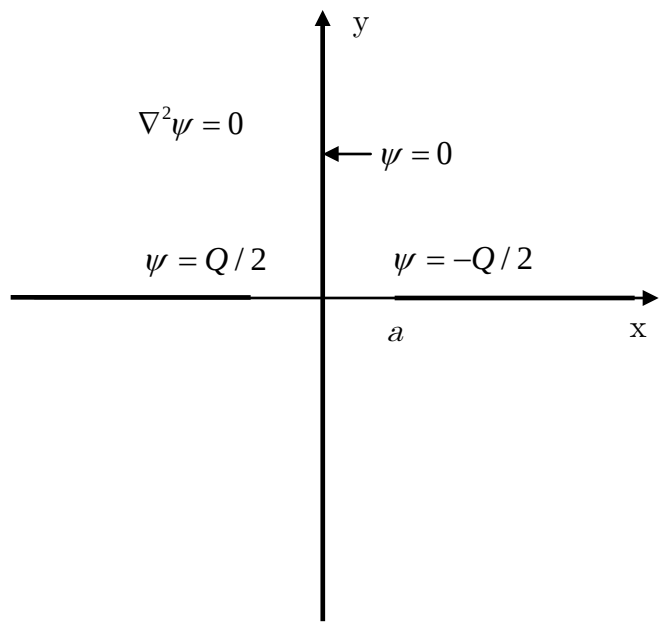

Figure 30. The simplified flow problem in flow focusing device

The derivation for flow field is similar to the derivation for the electric field (Appendix B) since the governing equation and boundary conditions are almost identical. Using conformal mapping, the dimensionless velocity distribution (*u, v* non-dimensionalized by *Q/2a*; *x, y* non-dimensionalized by *a*) are determined to be:

$$u = \pm\frac{2}{\pi}[(1-x^2+y^2)^2+4x^2y^2]^{-1/4}\sqrt{\frac{1-\dfrac{1-x^2+y^2}{\sqrt{(1-x^2+y^2)^2+4x^2y^2}}}{2}} \tag{4.3}$$

("+" corresponds to solution in 2nd quadrant, "-" corresponds to solution in 1st quadrant)

$$v = -\frac{2}{\pi}[(1-x^2+y^2)^2+4x^2y^2]^{-1/4}\sqrt{\frac{1+\dfrac{1-x^2+y^2}{\sqrt{(1-x^2+y^2)^2+4x^2y^2}}}{2}} \tag{4.4}$$

Based on the velocity distribution Eq. (4.3) and (4.4), the pressure distribution inside the chamber under 2D approximation can be determined using Bernoulli's equation $\Delta p = \frac{1}{2}\rho[V^2(x,y) - V^2(0,0)]$. Figure 31 plots the pressure distribution:

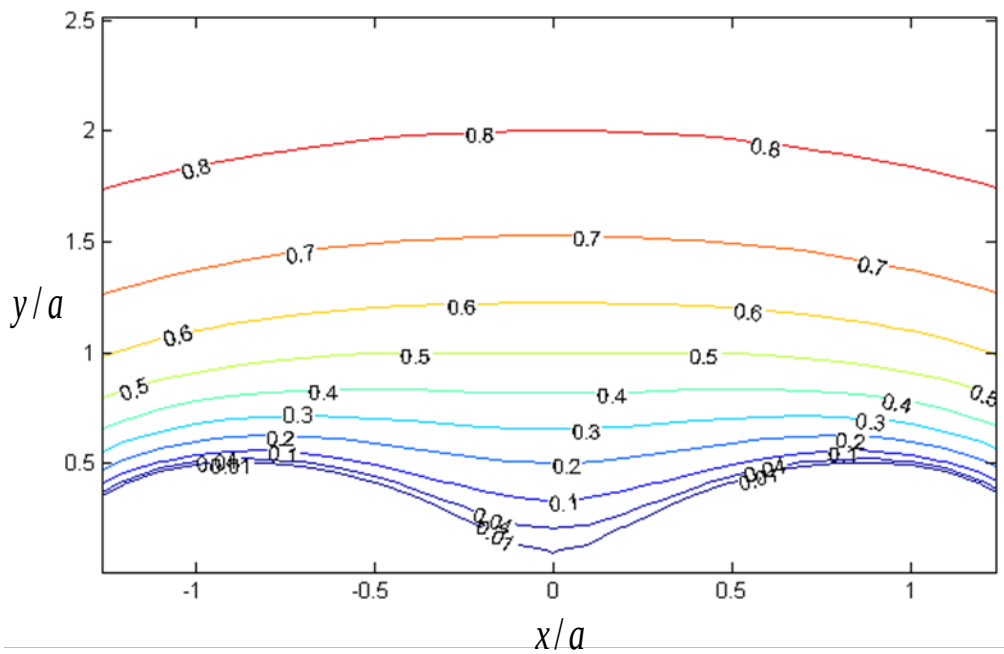

Figure 31: Equal pressure lines inside the chamber, values are non-dimensionalized by $\rho Q^2 / 2a^2\pi^2$

Next the stream lines are determined. The solution for the dimensionless stream function is:

$$\psi = -\frac{2}{\pi}\xi \tag{4.5}$$

Where ξ is the coordinate in the w plane. (x,y) is mapped to (ξ,η) through $z = \sin w$ (Appendix B), where

$$z = x + iy, w = \xi + i\eta \tag{4.6}$$

So:

$$x = \sin\xi \cosh\eta$$
$$y = \cos\xi \sinh\eta \tag{4.7}$$

A constant stream function line corresponds to a fixed ξ value, the corresponding *x, y* values in the *z* plane can be determined by setting ξ constant and varying η. The streamlines (whose values are nondimensionalized by Q/π) in the (*x,y*) plane (whose values are nondimensionalized by a) are shown in Figure 32.

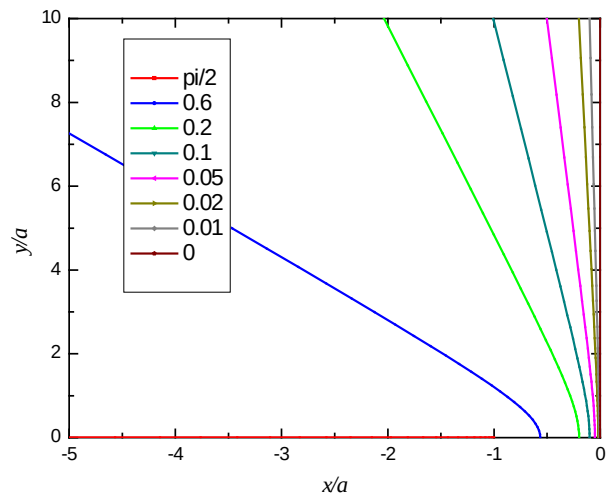

Figure 32: Streamlines, the stream function values are nondimensionalized by Q/π

At positions right above the gap center (*x*=0), the solutions are greatly simplified:

$$u = 0$$
$$v = -\frac{2}{\pi}\frac{1}{\sqrt{1+y^2}} \tag{4.8}$$

Or in its dimensional form,

$$u = 0$$
$$v/(Q/2a) = -\frac{2}{\pi}\frac{1}{\sqrt{1+(y/a)^2}} \tag{4.9}$$

At center (y axis), the pressure difference between inside the chamber and at the orifice can be expressed as:

$$\begin{aligned}\Delta p &= p(y) - p(0)\\ &= \frac{1}{2}\rho[v^2(0) - v^2(y)]\\ &= \frac{1}{2}\rho(\frac{Q}{2a})^2(\frac{2}{\pi})^2[1-\frac{1}{1+(\frac{y}{a})^2}]\\ &= \frac{\rho Q^2}{2a^2\pi^2}\frac{1}{1+(\frac{y}{a})^{-2}}\end{aligned} \tag{4.10}$$

The pressure distribution along the y axis is plotted in Figure 33:

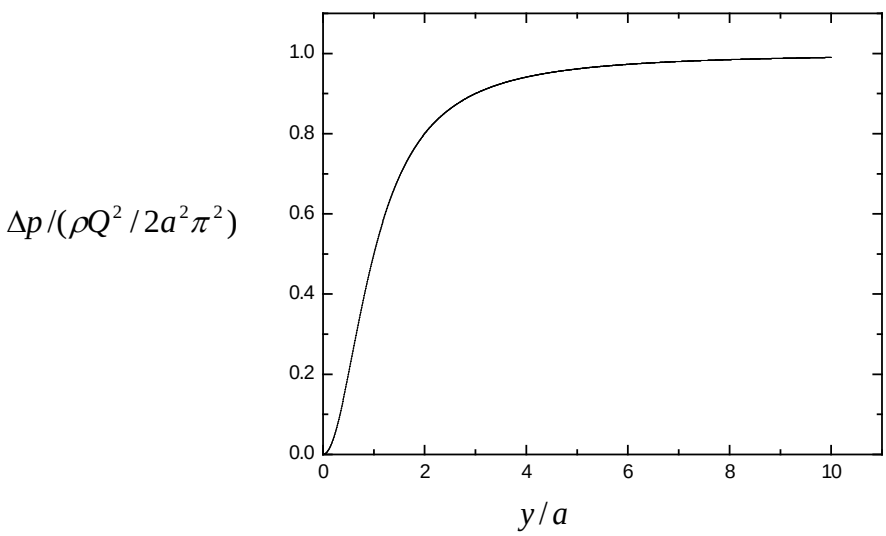

Figure 33: Pressure drop along the y axis

From Eq.(4.10) and Figure 33 it can be seen that the pressure is reduced by half when the nozzle is put at $y=a$. The pressure distribution is approximately linearly dependent with y up to $y=2a$. The horizontal pressure distribution is smooth from a to 2a according the equal pressure lines in Figure 31. The needle is typically placed above the gap center at a distance between a to $2a$ to capture most of the pressure drop caused by the gas flow. The jet direction will follow the gas flow streamlines which is perpendicular to the slit outlet (Figure 32).

4.3.2 Operation regions

The operating regions of the flow focusing device is comprehensively discussed by Si (2009). In the liquid flow rate (Q_l) and gas pressure drop (Δp_g) coordinate, the different operation regions depending on these two parameters are shown in Figure 34:

(i) Region I: Cone-shaking mode. in this region, the periodic formation of a jet is observed, as shown in Figure 34(b) for the three typical meniscus shapes in a jetting period. For a fixed pressure drop Δp_g, there is a minimum flow rate Q_{lmin} below which a steady jet cannot be maintained. The minimum flow rate requirement can be understood this way: if the flow rate is too low, according to expression (4.1), the jet radius is proportional to the square root of flow rate, when the jet radius reaches certain lower limit, the high surface tension stress caused by high surface curvature easily overcomes the gas shear stress and disrupts the jetting process. The actual outcome of this region is thus periodic jetting because of the disruption of jetting under low flow rates.

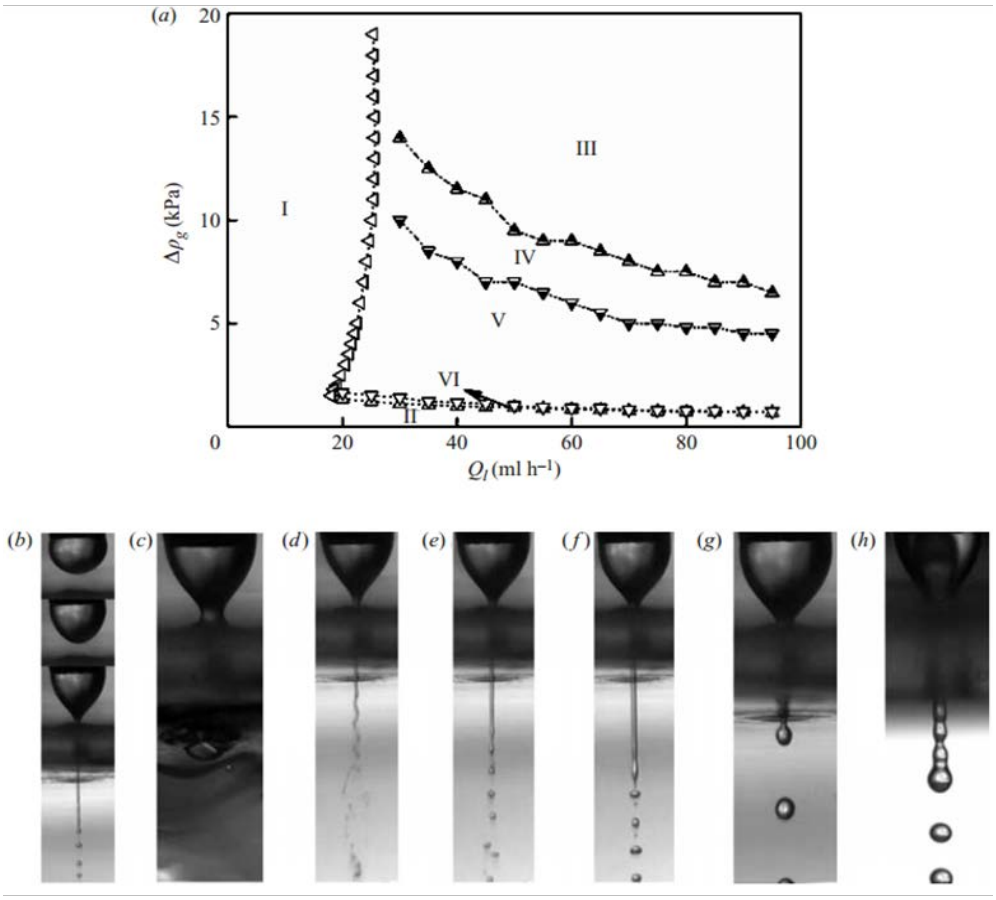

Figure 34: Operation regions for flow focusing device using water as working fluid. (Si, 2009). (a) Operation region in Q_l - Δp_g plane. (b) cone-shaking mode in region (I), (c) cone-adhering mode in region (II), (d) helical-jetting mode in region (III), (e) coexisting-jetting mode in region(IV), (f) Axisymmetric jetting mode in region (V), (g) dripping mode in region (VI), (h) dripping faucet, close to dripping mode, only observed occasionally

(ii) Region II: Cone-adhering mode. in this region, the pressure drop is not sufficient to stretch the meniscus into to a jet. For each value of Q_l, there is a minimum pressure drop $\Delta p_{g_{\min}}$ below which a jet cannot be formed, the meniscus grows and adheres to the outlet. Such a phenomena is shown in Figure 34(c). In experiment, when the starting pressure drop is low, the liquid always adheres to the outlet. In this

situation, a strong pressure drop can be applied to blow away the liquid and clean the orifice region.

(iii) Region III: Helical jetting mode. The jet has a helical shape due to the strong effect of gas flow. This mode happens at a flow rate larger than Q_{lmin} and a high enough pressure drop. At this mode, the jet's breakup is non-axisymmetric due to the strong gas flow. The jet first whips and then breaks up, the droplets formed in the high speed gas stream are elongated and split into smaller droplets. This region is shown in Figure 34(d).

(iv) Region IV: Coexisting jetting mode. A transition region between helical jetting mode and axisymmetric jetting mode (to be discussed next). In this region, both non-axisymmetric and axisymmetric perturbations exist. The droplets formed in this region moves downstream in a whipping way, and its diameter is close to the jet diameter.

(v) Region V: Axisymmetric jetting mode. This region is also called the "Rayleigh breakup region" discussed in Chapter 3. In this region, the jet breaks up axisymmetrically, and the influence of gas flow can be ignored. The dispersion relationship is Rayleigh's dispersion relationship, in which the most probable droplet size is 1.89 times the jet size. This region is shown in Figure 34(f) and is used in EHD perturbation experiment.

(vi) Region VI: Dripping mode. This region is very narrow, corresponding to the transition between axisymmetric jetting mode and cone-adhering mode, when the pressure drop reaches certain value below the axisymmetric jetting region. In this region,

the breakup length is significantly shorter, droplets are generated near the outlet and their sizes are perfectly equal but significantly larger than the axisymmetric mode. Such a region is shown in Figure 34(g). Another dripping mode is observed occasionally by Si (2009) which they call the "dripping faucet" and is shown in Figure 34(h).

Figure 34(a) shows a minimum flow rate and pressure drop must be achieved to generate a jet in the axisymmetric jetting mode. The minimum flow rate requirement can be understood in terms of jet Weber number. In the axisymmetric mode, jet radius R scales with $Q^{1/2}$ (Gañán-Calvo, 1998), jet velocity which scales with Q/R^2 is constant, as the flow rate decreases, the jet radius decreases, the Weber number $We = \rho v_j^2 R / \gamma$ which compares the relative magnitude between jet inertia and surface tension also decreases. Below a certain Weber number, jet inertia is not sufficient to overcome the confining effect of surface tension, jetting becomes dripping. From the Weber number expression it is also concluded that fluid with a smaller surface tension has smaller minimum flow rate. For example, in our experiment, ethanol is used as a working fluid, which can easily operate under a flow rate of 5ml/hr (for water, Q_{lmin} is around 20ml/hr as shown in Figure 34(a)).

From Eq. (4.1) it can be seen that if the pressure drop is too small, the jet diameter diverges, so a minimum pressure droplet must be maintained.

To sum up, in order to generate a steady jet in the axisymmetric mode, a minimum flow rate must be maintained, at each flow rate, there is a minimum pressure drop, below which no jet forms; and a maximum pressure drop, above which the jet can be helical which is not suitable for EHD perturbation experiment.

To analytically predict the operation region for axisymmetric jetting region, non-dimensionalization is required. The dimensionless groups are Reynolds number $\mathrm{Re} = \rho v_j R / \nu$ and Weber number $We = \rho v_j^2 R / \gamma$. Using the jet radius equation (4.1), Re and We can be expressed in terms of pressure drop ΔP and liquid flow rate Q:

$$\begin{aligned} We &= \frac{1}{\sigma}\left(\frac{8\rho}{\pi^2}\right)^{1/4} \Delta P^{3/4} Q^{1/2} \\ \mathrm{Re} &= \frac{2}{\mu}\left(\frac{\rho^3}{8\pi^2}\right)^{1/4} \Delta P^{1/4} Q^{1/2} \end{aligned} \tag{4.11}$$

With equation (4.11), Figure 34(a) can be re-plotted in the Re-We plane (Si, 2009). In the Re-We plane, three curves approximately encompasses the axisymmetric jetting region: (I) The lower We limit whose value corresponds to the transition from absolute instability (or dripping phenomena) to convective instability (steady jet). Such a We values depends on Re and is first discovered by Leib and Goldstein (1986). (II) The upper We limit, which corresponds to the transition between axisymmetric jet and whipping jet, when the pressure drop is too high, non-axisymmetric perturbation will grow, which makes the jet wavy and the generated droplets flow down in a whipping way, the high speed gas flow may elongate the generated droplet and make it break up into even smaller droplets. The Weber number corresponding to this transition is relatively independent to Re which is around 6 based on Si's (2009) result. (III) The minimum flow rate curve. According to Figure 34(a), the minimum flow change is not significant at various pressure drops. It can be assumed that the minimum flow rate is fixed for a certain flow focusing device. Canceling ΔP in equation (4.11) we arrive at:

$\frac{We}{\mathrm{Re}^3} = \frac{\pi\mu^3}{\gamma\rho^2 Q}$, which means the minimum flow rate curve in We-Re plane is a cubic function $We = C\,\mathrm{Re}^3$, where $C = \pi\mu^3 / \gamma\rho^2 Q_{l\,\min}$. The C value is dependent on the liquid used and the device geometrical configurations (e.g. the slit size, the ratio between nozzle exit height and slit size *H/D*). Such a curve is usually determined experimentally, for example, Vega(2010) demonstrated through experiment that the C value increases as *H/D* and surface tension decreases.

4.4 Results and discussion

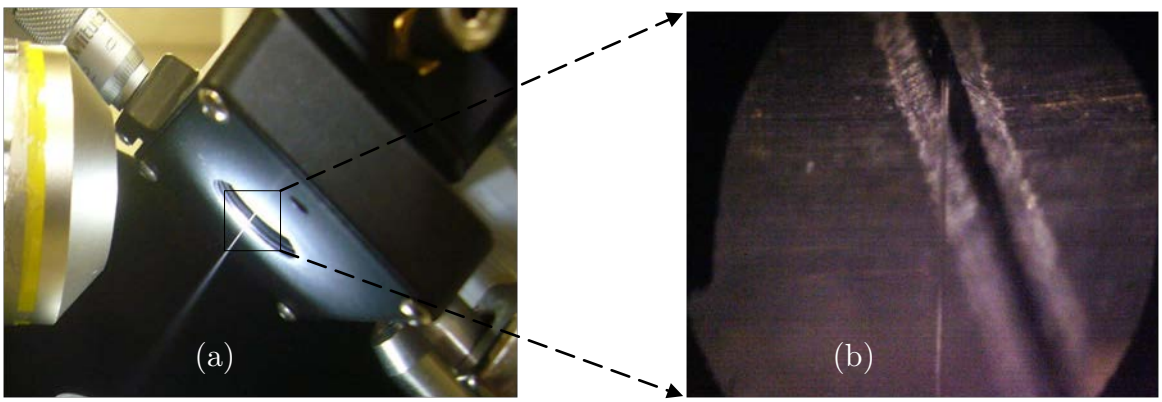

Figure 35: Generation of a flow focused jet through a slit

In this section we show the experimental results based on the scalable slit outlet flow focusing device. Figure 35 shows the jet formation at flow rate of 5ml/hr and pressure drop 3.0 psi. The chamber is made of commercially available mechanical slit with precise adjustable slit width. In experiment, the slit is wide at the start and gradually narrowed until a micro-jet is formed (Figure 35(b)).

Ganan Calvo derived the jet size (Eq. 4.1) to be only a function of flow rate and pressure drop. Next we try to verify this result by measuring the jet size under different pressure drop and flow rate situations. Figure 36 shows the jet size when one of the two parameters are varied, keeping the other fixed. The results are in accordance with Canan Calvo's prediction considering the measurement errors in this experiment.

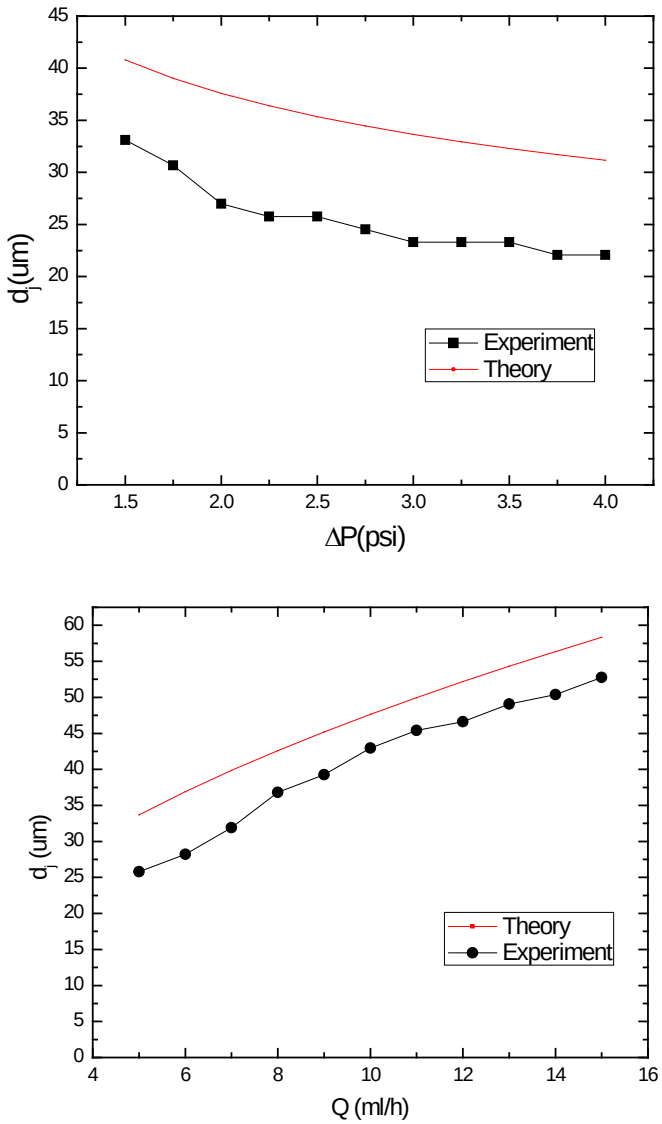

Figure 36: Jet size experimental vs. theoretical (Equation (4.1))

Such a focusing device using slit as outlet can be easily multiplexed. To demonstrate this, we generated 4 liquid jets through the slit and applied the EHD perturbation. The jet break up before and after the introduction perturbation is shown in Figure 37.

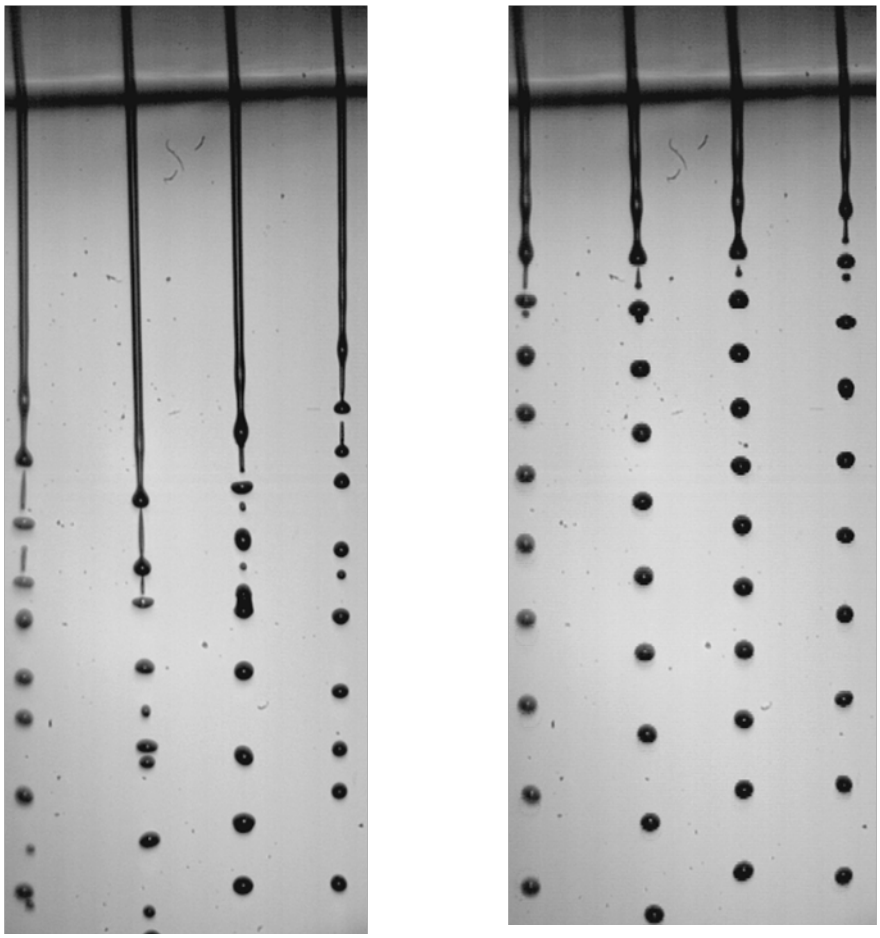

(a) Before EHD perturbation (b) After EHD perturbation

Figure 37: Jet breakup before(a) and after(b)introduction of EHD perturbation

As shown in Figure 37, after the introduction of EHD perturbation, the break up

length is fixed and significantly reduced compared with natural break up. The generation of droplets becomes uniform for each jet. The 4 jet sizes in figure 37 differ slightly, however the perturbation is still dominant for each jet which causes exactly one droplet generation in each half AC cycle. The space between the adjacent droplets is half AC period times the jet velocity. The smaler droplets seem to have higher velocity from Figure 37(b) since the space between them are larger . This is due to the acceleration of the gas flow only, smaller droplets have larger acceleration in the flow field. The initial velocity of the droplets are the same as the jet velocity is the same regardless the jet size according to jet size and flow rate relation Eq(4.1). The difference in jet size is probably due to the difference in the liquid flow rate in each nozzle, or due to the non-uniformity in pressure drop inside the chamber.

CHAPTER 5. EHD PERTURBATION ON TAYLOR CONE JET

Electrospray has gained increased application in the fields of biology, chemistry, materials science and engineering due to its unique properties. Under strong electric field, liquid meniscus will be deformed into a conical shape with a fine jet erupts the tip of the cone and breaks up into droplets. The jet is termed as Taylor cone jet (Taylor, 1964) before it breaks up to form electrospray. In this chapter, we will apply the EHD perturbation on the Taylor cone jet to control its breakup. First the fundamentals of electrospray are introduced, and then we show the experimental set up followed with experiment results and discussion.

5.1 Fundamentals of electrospray

Electrospray (ES) is a liquid atomization method that attracts growing interest in the aerosol community, mainly because of the phenomenal size range of particles it can produce, from molecular dimensions to hundreds of microns. A typical ES system can be readily implemented by feeding a liquid with sufficient electric conductivity through a small capillary which is charged to a high potential relative to a nearby ground electrode as shown by Figure 38.

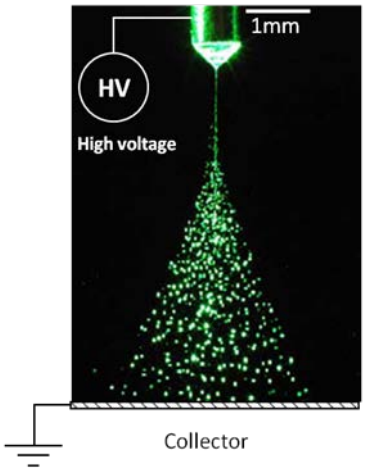

Figure 38: Typical electrospray (ES) setup (Gomez and Deng, 2008)

Depending on the operating conditions and liquid property, the liquid at the nozzle tip can be atomized in several different operation modes. Zeleny (1917) did the first systematic study on those modes and later Cloupeau and Prunet-Foch (1990) did a comprehensive phenomenological review. Among those modes, the most remarkable, widely used, and extensively studied is the *cone-jet* mode (Cloupeau and Prunet-Foch, 1990). In this mode, the liquid meniscus takes a conical shape, named Taylor-cone (Taylor, 1964), which is formed through a delicate balance between surface tension and normal electric stress at the liquid-air interface.

The key features that distinguish *cone-jet* electrospray from other atomization methods are:

(i) Quasi-monodispersity: The cone-jet mode offers the appealing feature of droplet monodispersity (Tang, 1994 and Chen, 1995). Typical relative standard

deviation of the droplet diameter for the *cone-jet* ES is 10% or less. The quasi-monodispersity brings great convenience in fundamental study, because a single ES or even a single droplet can reveal valid information for theoretical analysis or numerical simulation. The uniform droplet size also makes the creation of homogeneous, ordered, or periodic structures possible. From a thin film perspective, uniform droplet size is also attractive to enable uniform mass and heat flux upon interaction of the droplet with the substrate, in turn generating higher quality thin films. The generated droplets can be categorized as two kinds according to their size: primary droplets and satellite droplets. Due to higher charge to mass ratio and larger initial velocity, the satellite droplets are always at the outer edge of spray profile and shroud the primary droplets, we can thus use an electrode with size controllable opening to block the satellite droplets only and realize better monodispersity (Hong, 2008).

(ii) Tunable droplet and particle size in a wide range: From the *cone-jet* electrospray source, the droplet size can be controlled from nanometers to hundreds of micrometers continuously by either changing the liquid flow rate or adjusting the liquid conductivity. There are scaling laws (De La Mora, 1994 and Higuera, 2003) which relate the droplet size to these parameters. This allows us to tailor the droplet size which may be essential in applications which requires stringent droplet size distribution. In nanomanufacturing, a controlled and narrow size distribution in the nanometric range is produced by dissolving a nonvolatile solute into an electrosprayable solvent to inhibit the rapid evaporation and eventual disintegration of the droplet. In spray drying, the final particle size can be further adjusted by the solute concentration. The size of the

final solid particle product scale with $\eta^{1/3}d$, where η is the concentration of the precursor solution and d is the initial diameter of the liquid droplet. Therefore, low concentration, combined with small droplet size, may lead to very fine particles down to nanometer range.

(iii) Spray self-dispersion: Due to the same polarity of charge obtained from the power supply, the droplets repel each other under the Coulombic force, which prevents droplet coalescence and provides a way to manipulate the droplets through external electric field (Cha, 2000).

(iv) Dramatically reduced process time: Since the diffusion time for heat, mass and momentum, as well as the evaporation time, scales with d^2, a small decrease in droplet diameter leads to dramatic reductions in the characteristic time. Short heat diffusion time suggests fast and precise regulation of droplet temperature, which is crucial during thin film fabrication processes. Reduced mass and viscous diffusion time makes quick mixing of reactants possible. For heat-sensitive materials, as in OPVs, it is possible to have a reasonably fast evaporation even at modest temperatures, which avoids thermal destruction to the material.

(v) Low risk of clogging: The liquid being sprayed is fed into a relatively larger orifice (10^2-10^3μm) compared to that in inkjet printing (~30μm). The use of large bore minimizes the risk of liquid line obstruction and reduces pressure drop in the orifice.

(vi) Improved deposition efficiency due to image force: When electrically charged droplet approaches a conducting surface, an image charge is induced, generating an additional Coulombic force which tends to prevent droplet rebound from the substrate

(Deng, 2010). This mechanism can even eliminate the need for carrier gas since the charged droplet can be guided solely through electric field manipulation. This results in less material waste, and thus negative environmental impacts related to material waste is minimized.

5.2 Experimental Setup

The experimental setup for EHD perturbation on a jet issued from Taylor cone is similar to the setup of EHD perturbation on an inertia jet in Chapter 3 with slight modifications (Figure 39). The liquids used here are primary 100% ethanol; the mixture of 75 wt.% ethanol and 25 wt.% glycerol is also used to examine the effect of liquid viscosity. As shown in Figure 39, a stable Taylor cone jet is generated by charging the liquid passing a stainless needle (OD=300 μm and ID=150 μm) to about 2 kV. The liquid flow rate used here is from 1 to 20 mL/h.

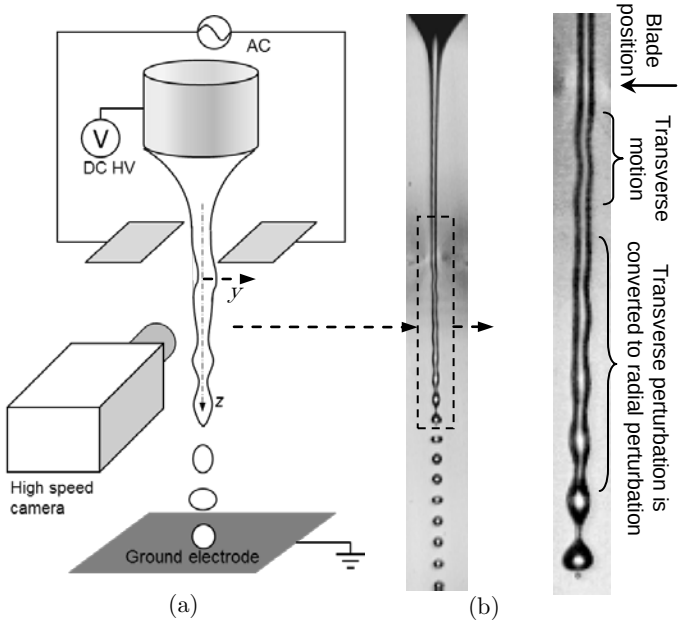

Figure 39. Taylor cone jet under EHD perturbation. The jet radius is 10 μm.

Without the high voltage, dripping is the observed phenomena under such a low flow rate. However, under suitable voltage and flow rate situations, the meniscus obtains a cone shape (Taylor cone) due to the balance of surface tension and electric stress; a thin jet erupts the tip of the cone which subsequently breaks up into small droplets . The typical current carried by the jet is tens of nA. The jet velocity is on the order of 10 m/s. Two electrodes with AC voltage is placed at both sides of the jet to provide the perturbation. Typically the two electrodes should be placed symmetrically so the jet won't skew to any side. The collector electrode is connected to a negative high voltage power supply to pull the generated small droplet to it. The break up process is recorded with high speed camera.

5.3 Results and discussion

5.3.1 Basic phenomenology

The natural oscillation frequency of a liquid meniscus (Taylor cone in this case) can be estimated by $\omega_0 = [\gamma/(\rho R_n^3)]^{1/2}$, where R_n is the nozzle radius. For a typical nozzle diameter of 300 μm, the Taylor cone oscillation frequency is below 1 kHz.

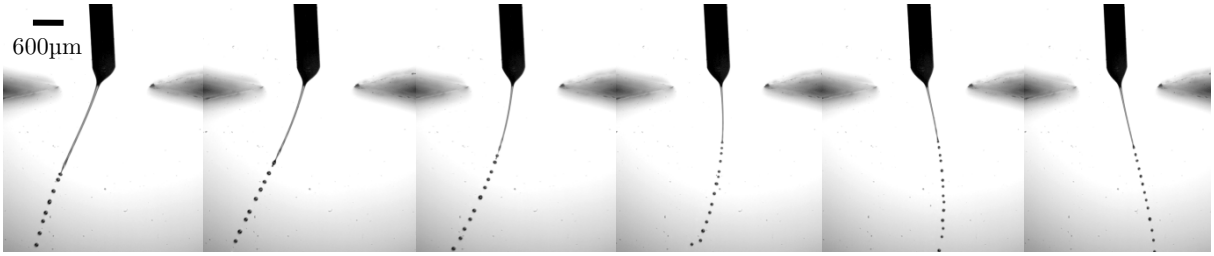

0 ms 0.44 ms 0.88 ms 1.32 ms 1.76 ms 2 ms

Figure 40: Jet swing images from a half cycle at low frequency (250 Hz)

When a low frequency (hundreds of Hz) perturbation is applied, the cone oscillates under the same frequency. Figure 40 shows high speed images when low frequency perturbation is applied, the cone oscillates in the plane where electric field has zero component perpendicular to it. The two dimensional oscillating cone leads to a plane oscillating jet which looks like a sheet by the naked eye.

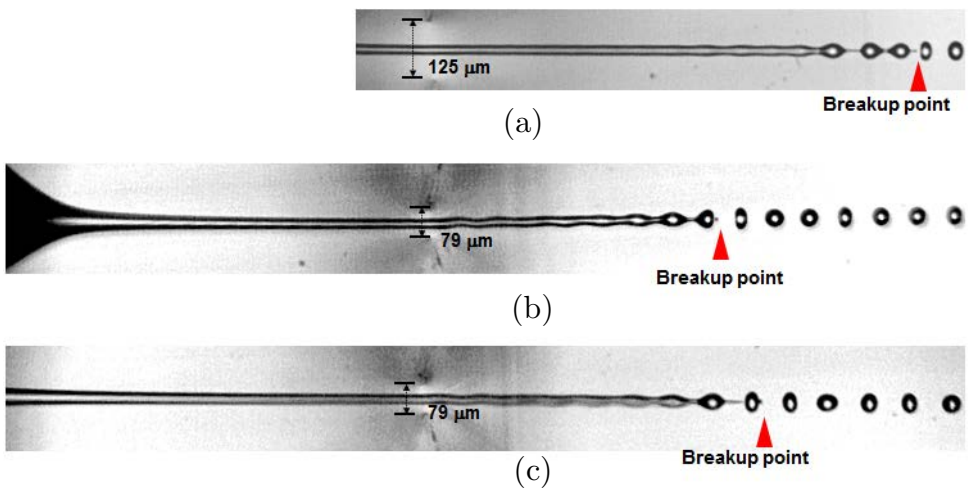

Figure 41. The effect of electrode configuration on the initial perturbation magnitude. All perturbation frequency is 80kHz, corresponding to a wavelength 125 μm. (a) gap 2a=125 μm; (b) gap 2a=79 μm; (c) same gap with case (b), but the blades are 300 μm further away from the Taylor cone

The cone oscillation natural frequency is much less than the frequency range of the AC signal applied for jet perturbation(10 kHz ~ 200 kHz). Therefore, under high perturbation frequencies (> 10kHz), despite the fact that the blade electrodes are placed just ~1mm away from the nozzle, highly stable and reproducible electrified jets are generated because the Taylor cone does not respond to the relatively high frequency AC signal. In this section we compare the effect of initial perturbation magnitude on the jet break up. Similarly as the inertia jets, we varied the blade electrodes separations and

locations to investigate their effect on initial perturbation magnitude and breakup length. Figure 41 shows the breakup length difference of such changes. Figure 41(a) and (b) shows that for the same $V_{p\text{-}p}$, reducing blade separation (from 125 μm to 79 μm) increases perturbation magnitude, which leads to shorter break up length. When the blade is positioned further away from the apex of the Taylor cone, the EHD perturbation is still capable to cause the jet to break up into monodisperse droplets (Figure 41c), however the breakup length becomes larger. The explanation is that if the blades are closer to the Taylor cone, the peak AC electric field are also closer, and the initial perturbation will be stronger, which leads to earlier breakup.

5.3.2 Jet response under sweeping frequencies

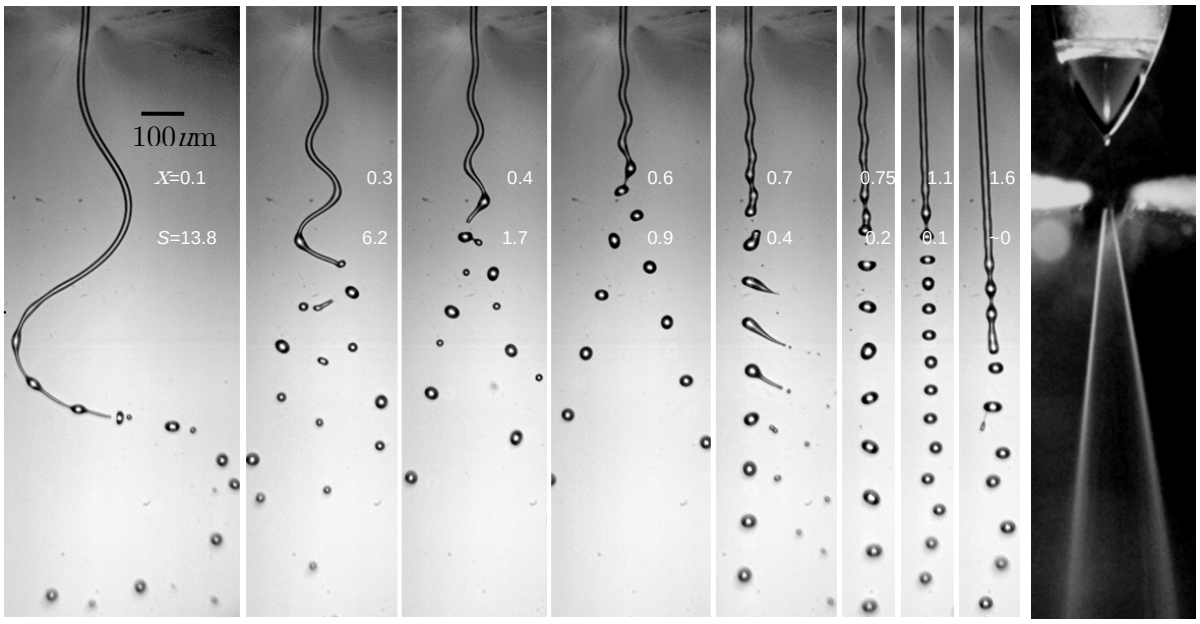

Figure 42: Typical response of the electrified jet to external EHD perturbation introduced by the AC electric field between the narrow gap of two in-plane blade electrodes.

Next the jet response under different perturbation frequencies are investigated. Shown in Figure 42 are the experimental phenomena using pure ethanol as the working fluid. The Taylor-cone is located above two blades as shown in Figure 42(i). At low frequencies, the response is varicose breakup superimposed on the swinging jet as shown in Figure 42(a), the jet swings violently while breaking up to droplets. Due to the stretching of the jet, there are long necks between two main droplets whose length is determined by the perturbation frequency. These long necks will break up into a series of smaller droplets. At a certain frequency range the jet breaks up into two stream monodisperse droplets as shown in Figure 42(d) which we call the "shearing mode" in chapter 3, because the jet looks as if it is torn apart by the electric field. From high speed image, the breakup of "shearing mode" is quite clean, with no satellite droplet generation between two primary droplets. From the naked eye, the two stream droplet generation looks like two lines as shown in Figure 42(i). Figure 42(b)(c) shows the break up before the two stream droplet generation. From Figure 42(a) to 42(b)(c), as the perturbation frequency increases, the wave number also increases, which leads to an increase in the growth rate of the varicose instability and earlier breakup. The droplet generation also becomes more regular due to the continuous reduction of neck length in this range. Figure 42(e)(f) shows a situation after the "shearing mode". The phenomenon in Figure 42(e) corresponds to the unification of a deformed ligament which would otherwise breakup into two droplets. Due to the zero growth rate of whipping, the initial whipping magnitude only causes the zigzag pattern on the jet which is finally damped by viscosity. In each AC cycle, only one primary droplet is generated compared with two in the

"shearing mode". The Rayleigh limit is $q=8\pi(\varepsilon_0\gamma r^3)^{1/2}$, this suggests that when two identical droplets charged at β time of Rayleigh limit merge, the newly merged droplet will have a charge level of $2^{1/2}\beta$ of the Rayleigh limit. When $2^{1/2}\beta$ is close or greater than unity, the newly formed droplet would immediately experience Coulombic fission (Gomez, 1994; Duft, 2003; Smith, 2002), shedding small daughter droplets to bring the charge level of the main droplet below Rayleigh limit. We can view the phenomena in Figure 42(e) as the merging of two droplets, when the charge level of the merged droplet exceeds Rayleigh limit, fission occurs. Fig 42(f) shows the transition stage before the Rayleigh mode is reached and Figure 42(g) is the Rayleigh mode, where the jet has zero whipping growth rate and maximum varicose growth rate. Under Rayleigh mode, the jet breaks up into a single stream of monodisperse droplets, with one droplet generation at each AC cycle. At even higher wave number, the varicose and whipping mode are both stable and jet does not response to the EHD perturbation, as shown in Figure 41(h). For each image in Figure 42(a)~(h), the perturbation wave number x and whipping magnitude (non dimensionalized by jet radius) S are labeled. S greater than 1 means whipping is dominant and S smaller than 1 signifies whipping does not grow (varicose dominant). Figure 42 clearly shows that the "whipping dominant" and "varicose dominant" regions are separated by the "shearing mode".

5.3.3 Effects of surface charge level

Different from the inertia jets, the surface charge density of cone-jets does not linearly depend on the DC voltage applied on the nozzle because the singular transition from

cone to jet. Nonetheless, the dimensionless charge level of cone-jets, Γ, can still be varied in two ways: either by changing the flow rate, or by changing the jet velocity. Note that σ is independent of the flow rate Q (Gañán-Calvo, 1999), while R scales with Q^{α}, where α is a scaling factor typically between 1/3 and 1/2. This suggests the charge level $\Gamma \propto Q^{\alpha}$. On the other hand, if Q is fixed, one can find that $\Gamma \propto v_j^{-2-\alpha}$, and the jet velocity v_j can be tuned by adjusting the driving field between the blades and the collector.

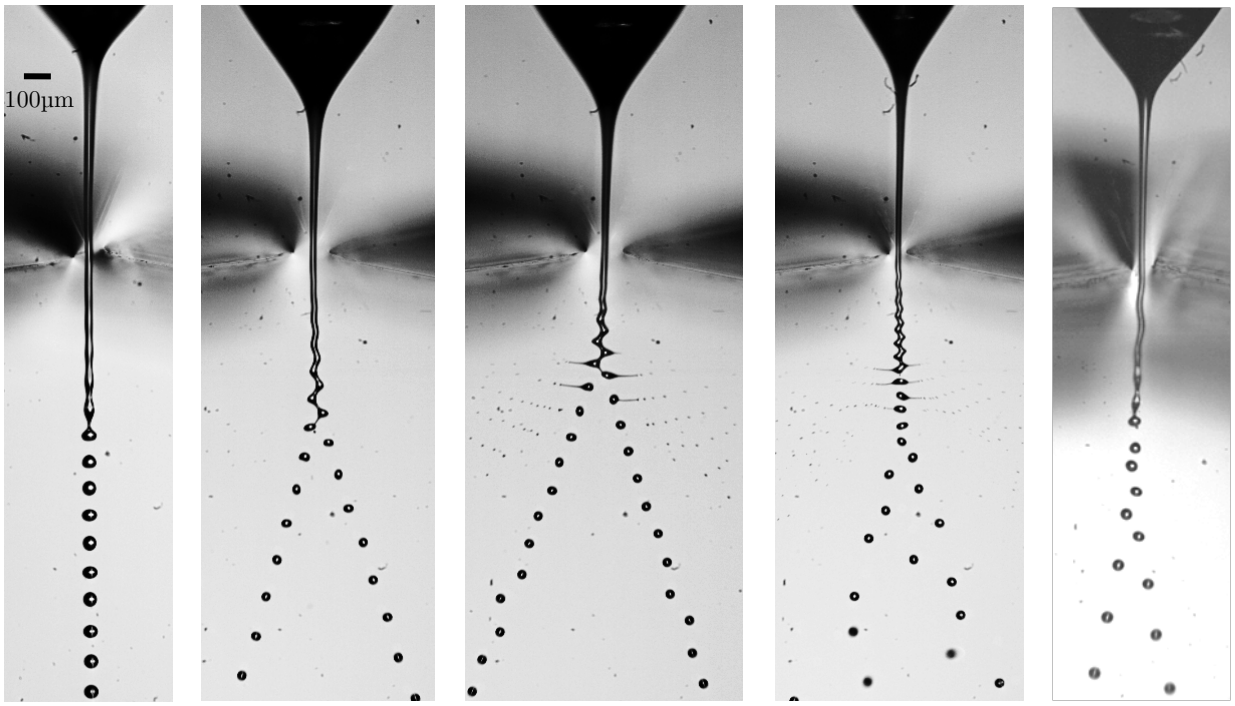

(a) (b) (c) (d) (e)

Figure 43: Representative images for x-$\mathbf{\Gamma}$ diagram (a) varicose mode, Q=16 ml/h, E_d=2 kV/cm, x=0.98; (b) whipping assisted bifurcation, Q=12 ml/h, E_d=2.5 kV/cm, x=0.69, $\mathbf{\Gamma}$=1.32; (c) overcharged whipping assisted bifurcation, Q=16 ml/h, E_d=1.25 kV/cm, x=0.69, $\mathbf{\Gamma}$=1.74; (d) overcharged varicose mode, Q=12 ml/h, E_d=1 kV/cm, x=1.21, $\mathbf{\Gamma}$=1.63; (e) varicose assisted bifurcation, Q=14 ml/h, E_d=2.5kV/cm, x=0.45, $\mathbf{\Gamma}$=0.56

The phenomenology of cone-jet response under EHD perturbation with different charge levels and perturbation wave numbers can be summarized in the x-Γ diagram (Figure 44). The boundaries that define the different behaviors include the Rayleigh limit ceiling ($\Gamma \geq 1.5$) and a few cut-off curves derived from the dispersion relationship. Here the "cut-off" refers to the zero growth rate of the corresponding instability. In other words, below the cut-off curve, the corresponding instability will not grow. Several modes of jet response can be identified in the x-Γ diagram:

(I) Varicose or Rayleigh mode (zone I and Fig.43a), which is at the proximity of the maximum growth rate of the varicose mode (dashed curve). Stronger perturbation (i.e. larger V_{p-p}/a) will expand the area of the domains of the varicose mode. In principle, the domain is bound by the 2nd harmonic cut-off, whipping cut-off, and varicose cut-off curves. A sub-mode can be identified as the overcharged varicose mode (Fig.43b), which is above the Rayleigh limit ceiling, and generated droplets experiences Coulombic fission.

(II) Whipping assisted bifurcation mode (zone II and Fig.43c), which is bound by the 3rd harmonic and whipping cut-off curves. In this domain, the whipping has non-zero growth rate and tears the jet in an alternating fashion that assists jet bifurcation. Again, above the Rayleigh limit ceiling, the generated droplets experiences Coulombic fission (Fig.43d). In addition, stronger perturbation also will push the data points closer to the boundary of cut-off curves.

(III) Varicose assisted bifurcation mode (zone III and Fig.43e), which is bound by cut-off curves of the 2nd harmonics, 3rd harmonics, and whipping instabilities. In this mode, the jet charge levels are low and the jet wavy patterns from initial transverse

perturbation will not be amplified because of zero growth rate of whipping. It is the varicose instability that drives the wavy jet breakup. Bifurcation happens because the formed droplets are off from center line due to initial wavy jet pattern. We note that jet bifurcation similar to the behavior in zone III has been reported by Lin and Webb (1994). In Lin and Webb (1994), the liquid jet is charge neutral (Γ=0), and the perturbation was introduced through the transverse vibration of a slender glass nozzle. Despite the different source of perturbation, the jet breakup behavior in Lin and Webb (1994) can still be categorized as varicose assisted bifurcation which falls into zone III of the x-Γ diagram.

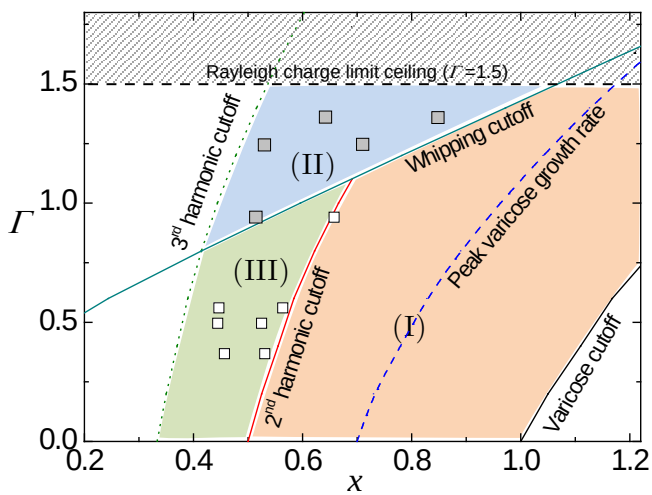

Figure 44: Jet response phenomenon mapped in the x-$\mathbf{\Gamma}$ diagram. Scattered data points are experimental data.

5.3.4 Effects of viscosity

In order to investigate the effect of viscosity on jet response under EHD perturbation, pure ethanol is replaced with mixture of 75% ethanol + 25% glycerol, the viscosity is increased by 10-fold compared with pure ethanol. Viscosity can dissipate energy and thus has a stabilizing effect. Noticeably, the growth of varicose mode is significantly suppressed and the jet can exist for much longer without breakup (Fig.45a) compared to pure ethanol jet.

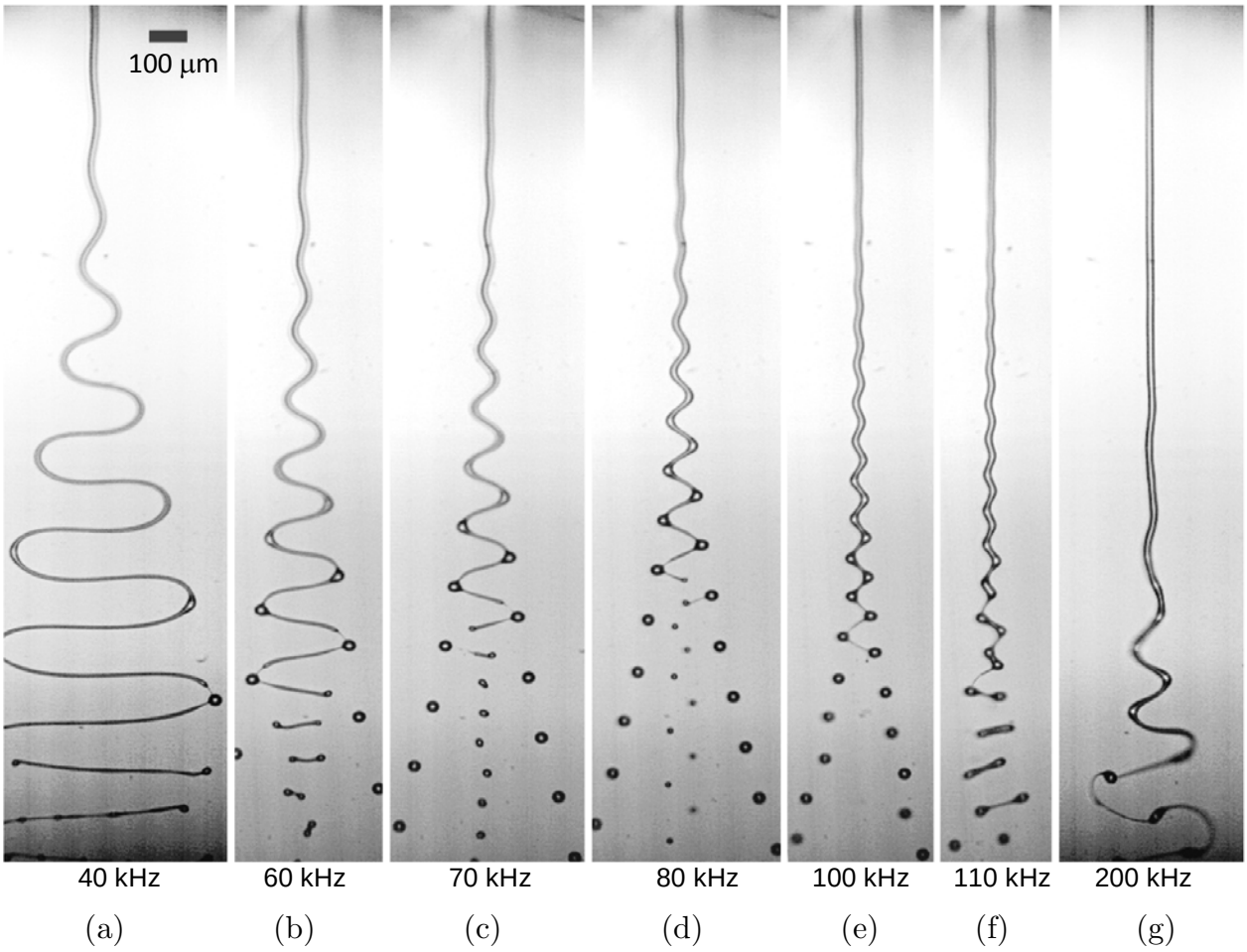

Figure 45: Perturbation response of more viscous liquid (75% ethanol + 25% glycerol, 8ml/h).

As wavenumber increases, varicose mode becomes more prominent. Noticeably, thin and long liquid threads between two droplets form the zigzag pattern (Fig.45 b and c). The breakup of the thread leads to satellite droplets that are much smaller than the primary droplets. At certain wavenumber corresponding to a large growth rate for the second harmonic of varicose instability and non-zero growth rate for whipping instability(Fig.45c), the volume of the connecting filament reaches minimum and the jet breaks up into droplets with good monodispersity even for viscous liquids. In other words, "shearing mode" is still observed for high viscous liquids, the reason is at certain perturbation wave number, whipping instability stretches the jet which is converted to large magnitude varicose perturbation; when the varicose growth rate at this wave number is large, the viscous jet breaks up into two clean streams with good monodispersity. At even higher perturbation wavenumbers, whipping mode is stable, no Rayleigh mode is observed due to the suppression of varicose instability for high viscous liquids.

CHAPTER 6. CONCLUSIONS

This dissertation investigated the breakup phenomena and mechanism of neutral and electrified jets under transverse EHD perturbations. Three different jetting mechanisms are used to generate jets with various ranges of jet diameters: ~150 micrometer inertial jets from liquid pressurized through a small orifice, ~50 micrometer flow focused jets from the same in-plane exciter, and ~20 micrometer electrified Taylor-cone jets. Two designs of EHD exciter are used: a one-side capacitor type asymmetrical exciter and a symmetric in-plane exciter. The transverse perturbations enable systematic triggering of varicose and whipping instabilities, and consequently a wide range of remarkable phenomena emerge. For inertia jets with zero or low charge levels, only varicose instability is observable due to suppressed whipping instability. At modest charge levels, inertia jets can respond to the fundamental perturbation frequency as well as the second harmonic of the perturbation frequency. Highly charged jets such as fine jets generated from Taylor cones exhibit distinct behavior for different perturbation wavenumber x. Typical behavior include: whipping jets with superimposed varicose instability at small x, jet bifurcation from crossover of whipping and varicose instability instabilities at x~0.5, Coulombic fission owing to the surge of surface charge density as the slender liquid segments recover spherical shapes at x~0.7, and simple varicose mode near wave numbers of unity. The phenomena observed in this work may be explained by a linear

model and rationalized by the phase diagram in the space of wave number and dimensionless charge levels.

The experimental apparatus used in this dissertation is simple, non-intrusive, and scalable to a linear array of jets. The well-controlled, systematic triggering and co-development of the two most common jet instabilities (varicose and whipping) significantly expands the breakup possibilities of electrified jets. The rich yet rationalizable phenomena may spawn new fundamental and applied discoveries such as regulated electrospinning, strictly monodisperse micro/nano droplets, and manufacturing of high aspect ratio fine particles from drying droplets that undergo highly reproducible Coulombic fissions.

APPENDIX A: RAYLEIGH DISPERSION RELATIONSHIP (ADAPTED FROM P.G.DRAZIN AND W.H.REID:*HYDRODYNAMIC STABILITY*)

Consider an infinitely long inviscid liquid within the cylinder r=R, the liquid has surface tension γ and is stationary initially. The initial velocity and pressure is expressed as:

$$U = 0, P = p_\infty + \frac{\gamma}{R}(0 \le r \le R) \tag{A.1}$$

Euler's equation of motion for an inviscid fluid gives

$$\rho(\frac{\partial \vec{u}}{\partial t} + \vec{u} \cdot \nabla \vec{u}) = -\nabla p \tag{A.2}$$

And continuity condition gives:

$$\nabla \cdot \vec{u} = 0 \tag{A.3}$$

Denote $\vec{n}$ as the outward normal from the liquid surface, $\nabla \cdot \vec{n} = R_1^{-1} + R_2^{-1}$, if the surface is disturbed the surface becomes $r = \xi(z, \theta, t)$ in terms of cylindrical polar coordinates (z, r, θ), the dynamic boundary condition at the surface is:

$$p = p_\infty + \gamma \nabla \cdot \vec{n}(r = \xi) \tag{A.4}$$

where

$$\vec{n} = (-\frac{\partial \xi}{\partial z}, 1, -\frac{\partial \xi}{r \partial z})\{(\partial \xi / \partial z)^2 + 1 + (\partial \xi / r \partial z)^2\}^{-1/2} \tag{A.5}$$

The kinematic condition that each particle on the surface remains there gives:

$$u_r = D\xi / Dt(r = \xi) \tag{A.6}$$

Linearization of these equations and boundary conditions by neglecting products of the increments $\vec{u}' = \vec{u}, p' = p - P, \xi' = \xi - R$ gives:

$$\rho \partial \vec{u}' / \partial t = -\nabla p' \tag{A.7}$$

$$\nabla \cdot \vec{u}^{'} = 0 \tag{A.8}$$

$$p^{'} = -\gamma(\xi^{'} / R^2 + \partial^2 \xi^{'} / \partial z^2 + \partial^2 \xi^{'} / R^2 \partial \theta^2)(r = R) \tag{A.9}$$

$$u_r^{'} = \partial \xi^{'} / \partial t (r = R) \tag{A.10}$$

By the method of normal modes we consider only a typical wave component with:

$$(\vec{u}^{'}, p^{'}, \xi^{'}) = (\hat{u}(r), \hat{p}(r), \hat{\xi}) e^{\omega t + i(sz + m\theta)} \tag{A.11}$$

where $s = \dfrac{2\pi}{\lambda}$ is the axial wavenumber and m an integer. Equation (A.7) and (A.8)give:

$$\Delta p^{'} = -\rho \partial (\nabla \cdot \vec{u}^{'}) / \partial t = 0 \tag{A.12}$$

The Laplacian in cylindrical system is given by:

$$\Delta = \partial^2 / \partial r^2 + \partial / r \partial r + \partial^2 / r^2 \partial \theta^2 + \partial^2 / \partial z^2 \tag{A.13}$$

Therefore:

$$\frac{d^2 \hat{p}}{dr^2} + \frac{d\hat{p}}{rdr} - (s^2 + m^2 / r^2) \hat{p} = 0 \tag{A.14}$$

This is the modified Bessel equation of the first kind, the solution which is bounded when r~0 is given by:

$$\hat{p} = A I_m (kr) \tag{A.15}$$

where A is a constant, equation (A.7) then gives:

$$\hat{u} = -A(\rho\omega)^{-1} (isI_m(sr), sI_m^{'}(sr), imr^{-1} I_m(sr)) \tag{A.16}$$

Finally, the boundary condition (A.9)(A.10) gives:

$$A I_m(x) = -\gamma(1 - x^2 - m^2) \hat{\xi} / R^2 \tag{A.17}$$

and

$$-A(R\rho\omega)^{-1} x I_m^{'}(x) = \omega\hat{\xi} \tag{A.18}$$

where $x = Rs = \frac{2\pi R}{\lambda}$. Equation (A.17) and (A.18) then gives:

$$\omega^2 = \frac{\gamma}{R^3\rho}\frac{xI_m^{'}(x)}{I_m(x)}(1 - x^2 - m^2) \tag{A.19}$$

which is the final form of Rayleigh dispersion relationship.

APPENDIX B: ELECTRIC FIELD BETWEEN TWO HORIZONTAL BLADES WITH EDGE FACING EACH OTHER

In the jet EHD perturbation experiment, we have two sharp blades separated by a distance $2a$ with edge facing each other. The two sharp blades are connected to AC electrical field. Assuming the two plates are semi infinite; the problem becomes a 2D problem as shown in Figure 46. It can be seen as a steady state problem with the left edge has potential $-V_0$ and right edge has potential V_0. By symmetry the y axis has zero potential. Our problem is to solve the Laplace equation $\nabla^2\phi = 0$ with the specified boundary condition as shown in Figure 46.

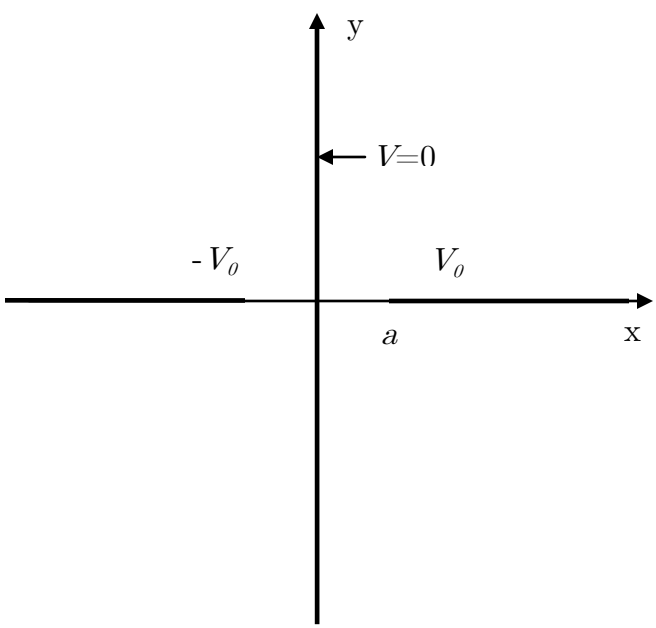

Figure 46: 2D problem of electric field for the experiment setup

Using $x^* = x/a$, $y^* = y/a$ and $\phi^* = \phi/V_0$ to non-dimensionalize the problem, the problem becomes solving Laplace equation $\nabla^2\phi^* = 0$ with the boundary condition

specified in Figure 47 (we only consider the right half plane since the problem is symmetric).

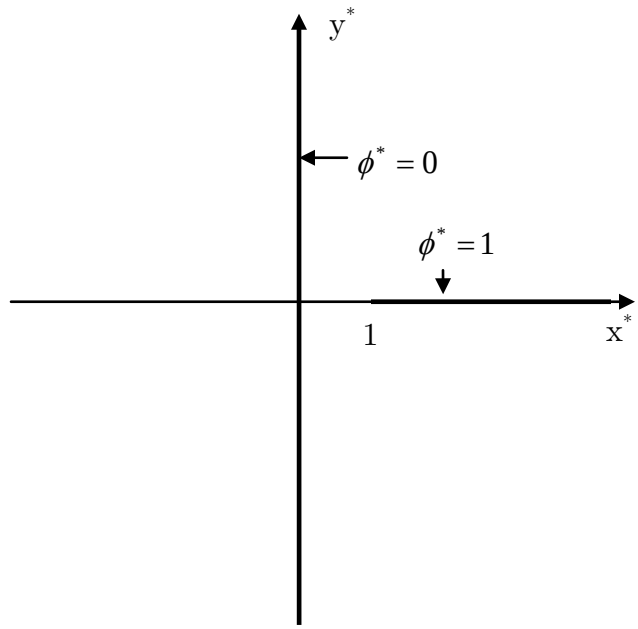

Figure 47: 2D problem of electric field after non-dimensionalizing

The electric field on the jet surface is strongest at the location closest to the blade and it determines the initial perturbation magnitude. To analytically determine the electric field and hence the initial perturbation magnitude, consider the 2D problem shown in Figure 47. In the (x,y) coordinate, y axis has a dimensionless potential 0, x axis with $x>1$ has a dimensionless potential 1, which is similar to our jet-blade configuration. The electric field in the right side of the (x,y) plane can be analytically determined through a conformal mapping $w = \sin^{-1} z$ (Zill, 2006) which maps the shaded area (Fig 48(a)) in the (x,y) plane to the shaded strip in the (ξ, η) plane.

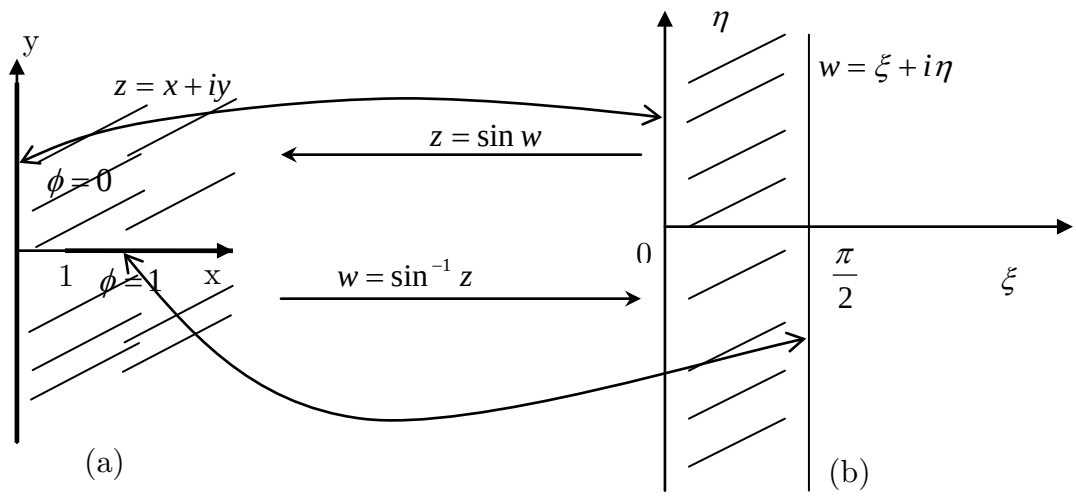

Figure 48: Conformal mapping of z domain (a) to w domain (b), where the geometry has been transformed to a strip.

After the conformal mapping, our problem is now in a strip domain (w plane) shown on the left of Figure 48. The boundary condition for $\xi = \frac{\pi}{2}$ is $\phi = 1$ and for $\xi = 0$ is $\phi = 0$. The solution for potential in the strip in w domain is thus $\phi(\xi,\eta) = \frac{2}{\pi}\xi$ and the complex potential at the w domain is: $F = \phi(\xi,\eta) + i\psi(\xi,\eta) = \frac{2}{\pi}\xi + i\frac{2}{\pi}\eta = \frac{2}{\pi}w$.

The electric field calculated using the complex potential is:

$$-E_x + iE_y = \frac{dF}{dz} = \frac{dF}{dw}\cdot\frac{dw}{dz} = \frac{2}{\pi}\frac{1}{\sqrt{1-z^2}}$$

$$= \frac{2}{\pi}[(1-x^2+y^2)^2 + 4x^2y^2]^{-1/4}[\sqrt{\frac{1+\frac{1-x^2+y^2}{\sqrt{(1-x^2+y^2)^2+4x^2y^2}}}{2}} - i\sqrt{\frac{1-\frac{1-x^2+y^2}{\sqrt{(1-x^2+y^2)^2+4x^2y^2}}}{2}}]$$

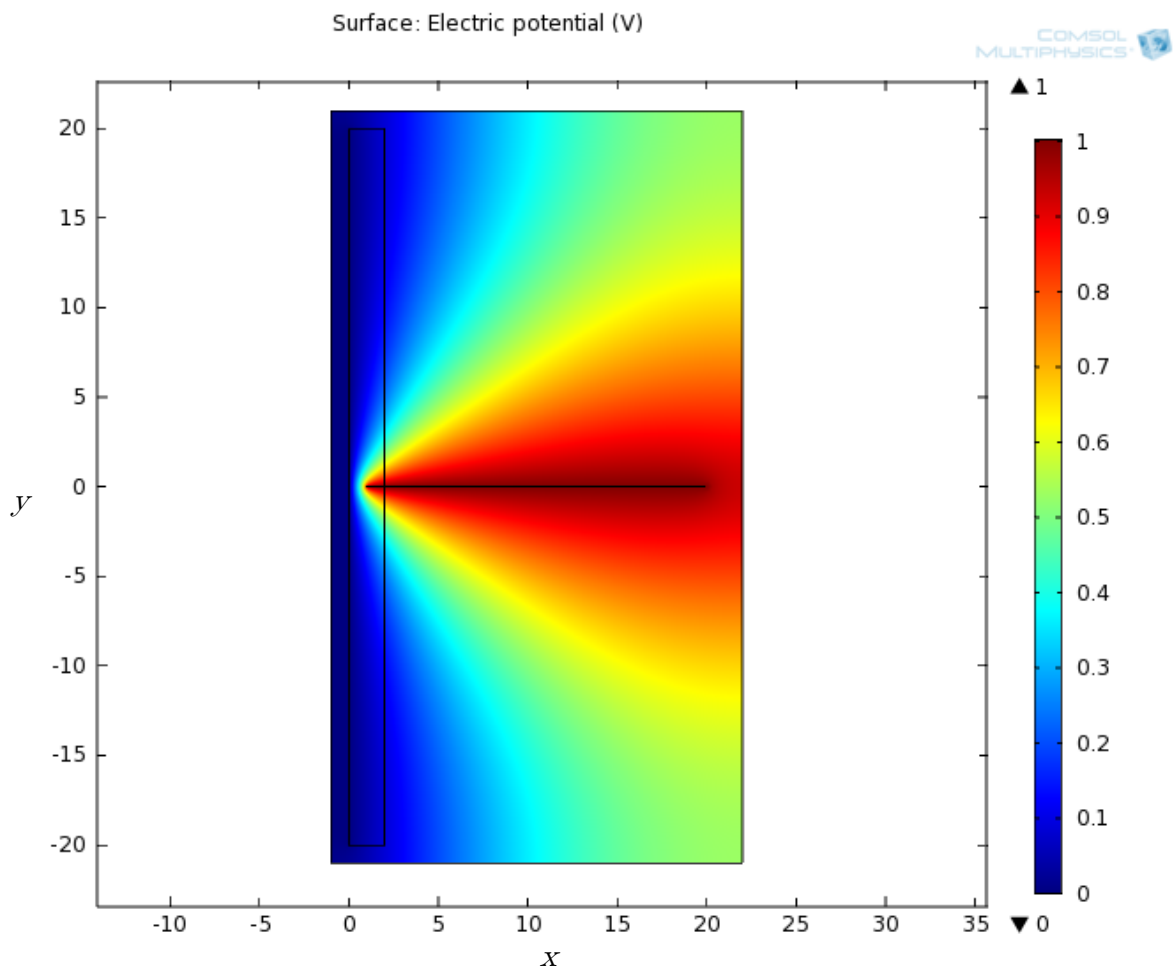

Figure 49: COMSOL simulation for the dimensionless electric potential for a problem shown in Figure 48(a).

Figure 49 shows the numerical simulation of the electric potential. The comparison between numerical simulation and analytical solution for E_x at two locations: x=0 and x=1/2 are shown in Figure 50, which agree with each other.

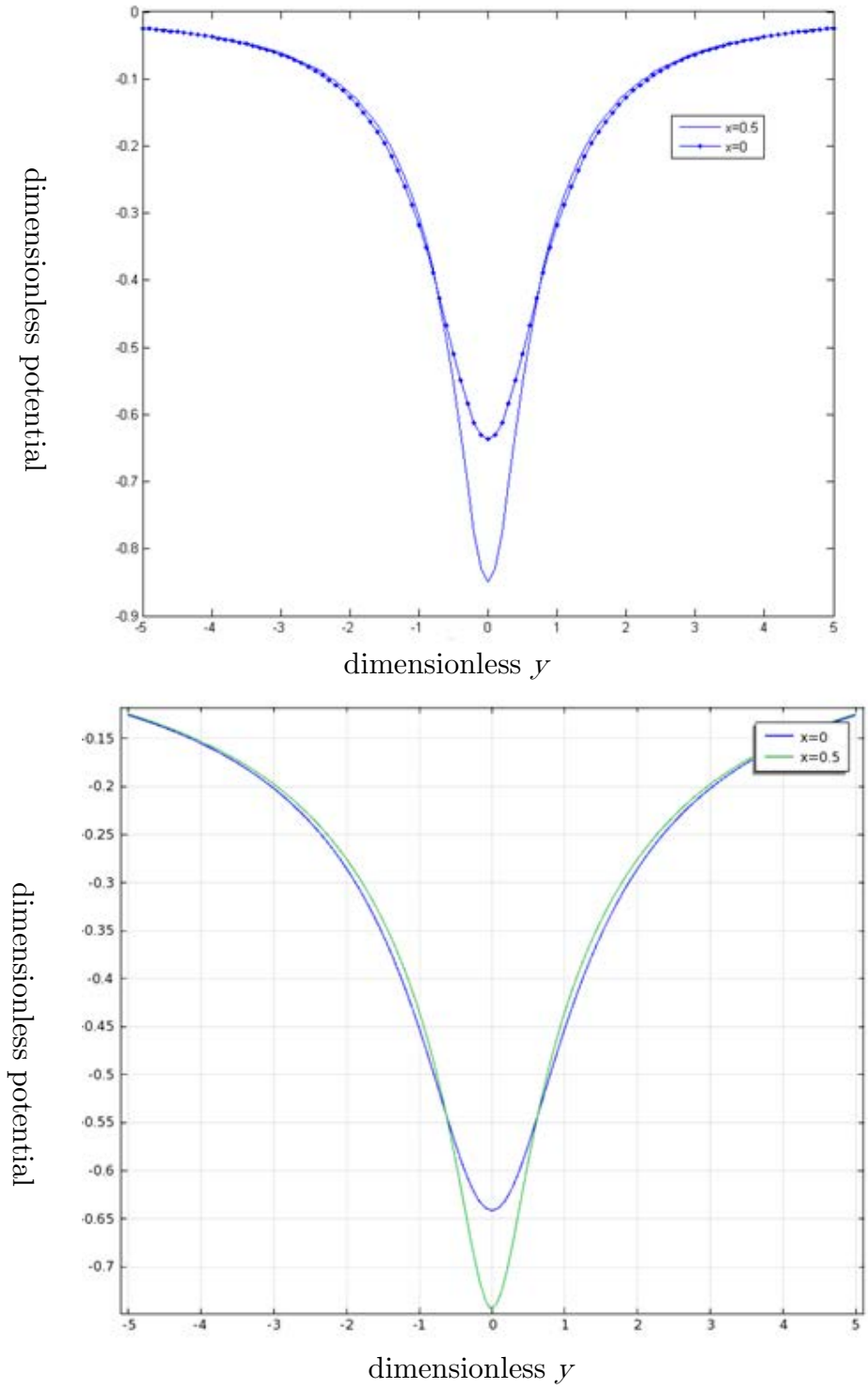

Figure 50: Analytical (top) and numerical (bottom) solutions for Ex at x=0 and x=1/2 (for problem shown in Figure 48(a)).

Finally, in its dimensional form, E_x and E_y are expressed as:

$$E_x = -\frac{2V}{\pi a}[(1-(\frac{x}{a})^2+(\frac{y}{a})^2)^2+4(\frac{x}{a})^2(\frac{y}{a})^2]^{-1/4}\sqrt{\frac{1+\frac{1-(\frac{x}{a})^2+(\frac{y}{a})^2}{\sqrt{(1-(\frac{x}{a})^2+(\frac{y}{a})^2)^2+4(\frac{x}{a})^2(\frac{y}{a})^2}}}{2}} \quad \text{(B.1)}$$

$$E_y = \pm\frac{2V}{\pi a}[(1-(\frac{x}{a})^2+(\frac{y}{a})^2)^2+4(\frac{x}{a})^2(\frac{y}{a})^2]^{-1/4}\sqrt{\frac{1-\frac{1-(\frac{x}{a})^2+(\frac{y}{a})^2}{\sqrt{(1-(\frac{x}{a})^2+(\frac{y}{a})^2)^2+4(\frac{x}{a})^2(\frac{y}{a})^2}}}{2}} \quad \text{(B.2)}$$

where the "+" sign in (B.2) corresponds to solution in the first quadrant and "-" corresponds to fourth quadrant, V is the potential of the x axis ($x>a$).

We will only consider the x component of the electric field since only transverse perturbation is of importance here. Another reason is that closest to the blade, where the electric field is strongest, the y component of the electric field vanishes. By setting x=0, the x component of the electric field is greatly simplified:

$$E_x = \frac{-2V}{\pi a\sqrt{1+(\frac{y}{a})^2}} \quad \text{(B.3)}$$

REFERENCES

Berglund RN, Liu BYH. 1973. Generation of monodisperse aerosol standards. *Environ. Sci. Technol.* 7(2):147–53

Bogy DB. 1979. Drop formation in a circular liquid jet. *Annual Review of Fluid Mechanics*. 11(1):207–28

Cha B, Blades M, Douglas DJ. 2000. An interface with a linear quadrupole ion guide for an electrospray-ion trap mass spectrometer system. *Anal. Chem.* 72(22):5647–54

Chandrasekhar, S., 1961. Hydrodynamic and Hydromagnetic Stability. Courier Dover Publications.

Chaudhary KC, Redekopp LG. 1980. The nonlinear capillary instability of a liquid jet. part 1. theory. *Journal of Fluid Mechanics*. 96(02):257–74

Chauhan A, Maldarelli C, Rumschitzki DS, Papageorgiou DT. 2003. An experimental investigation of the convective instability of a jet. *Chemical Engineering Science*. 58(11):2421–32

Chen D-R, Pui DYH, Kaufman SL. 1995. Electrospraying of conducting liquids for monodisperse aerosol generation in the 4 nm to 1.8 μm diameter range. *Journal of Aerosol Science*. 26(6):963–77

Cline HE, Anthony TR. 2008. The effect of harmonics on the capillary instability of liquid jets. *Journal of Applied Physics*. 49(6):3203–8

Cloupeau M, Prunet-Foch B. 1990. Electrostatic spraying of liquids: main functioning modes. *Journal of Electrostatics*. 25(2):165–84

Collicott SH, Zhang S, Schneider SP. 1994. Quantitative liquid jet instability measurement system using asymmetric magnification and digital image processing. *Experiments in Fluids*. 16(5):345–48

Crowley JM. 1983. Electrohydrodynamic droplet generators. *Journal of Electrostatics*. 14(2):121–34

De Gans B-J, Duineveld PC, Schubert US. 2004. Inkjet printing of polymers: state of the art and future developments. *Adv. Mater.* 16(3):203–13

De La Mora JF, Loscertales IG. 1994. The current emitted by highly conducting taylor cones. *Journal of Fluid Mechanics*. 260:155–84

Deng W, Gomez A. 2010. The role of electric charge in microdroplets impacting on conducting surfaces. *Physics of Fluids (1994-present)*. 22(5):051703

Deng W, Gomez A. 2011. Electrospray cooling for microelectronics. *International Journal of Heat and Mass Transfer*. 54(11–12):2270–75

Donnelly RJ, Glaberson W. 1966. Experiments on the capillary instability of a liquid jet. *Proc. R. Soc. Lond. A*. 290(1423):547–56

Duan H, Li C, Yang W, Lojewski B, An L, Deng W. 2013a. Near-field electrospray microprinting of polymer-derived ceramics. *Journal of Microelectromechanical Systems*. 22(1):1–3

Duan H, Yang W, Li C, Lojewski B, Deng W. 2013b. Scalable generation of strictly monodisperse droplets by transverse electrohydrodynamic excitations. *Aerosol Science and Technology*. 47(11):1174–79

Duft D, Achtzehn T, Müller R, Huber BA, Leisner T. 2003. Coulomb fission: rayleigh jets from levitated microdroplets. *Nature*. 421:128

Eggers J. 1997. Nonlinear dynamics and breakup of free-surface flows. *Rev. Mod. Phys.* 69(3):865–930

Eggers J, Villermaux E. 2008. Physics of liquid jets. *Rep. Prog. Phys.* 71(3):036601

Fenn JB, Mann M, Meng CK, Wong SF, Whitehouse CM. 1989. Electrospray ionization for mass spectrometry of large biomolecules. *Science*. 246(4926):64–71

Fong H, Chun I, Reneker DH. 1999. Beaded nanofibers formed during electrospinning. *Polymer*. 40(16):4585–92

Fujimoto M, Kado T, Takashima W, Kaneto K, Hayase S. 2006. Dye-sensitized solar cells fabricated by electrospray coating using tio2 nanocrystal dispersion solution. *J. Electrochem. Soc.* 153(5):A826–A829

Gañán-Calvo AM. 1998. Generation of steady liquid microthreads and micron-sized monodisperse sprays in gas streams. *Phys. Rev. Lett.* 80(2):285–88

Gañán-Calvo AM. 1999. The surface charge in electrospraying: its nature and its universal scaling laws. *Journal of Aerosol Science*. 30(7):863–72

Gañán-Calvo AM, Barrero A. 1999. A novel pneumatic technique to generate steady capillary microjets. *Journal of Aerosol Science*. 30(1):117–25

Goedde EF, Yuen MC. 1970. Experiments on liquid jet instability. *Journal of Fluid Mechanics*. 40(03):495–511

Gomez A, Tang K. 1994. Charge and fission of droplets in electrostatic sprays. *Physics of Fluids (1994-present)*. 6(1):404–14

González H, García FJ. 2009. The measurement of growth rates in capillary jets. *Journal of Fluid Mechanics*. 619:179–212

Hartman RPA, Brunner DJ, Camelot DMA, Marijnissen JCM, Scarlett B. 2000. Jet break-up in electrohydrodynamic atomization in the cone-jet mode. *Journal of Aerosol Science*. 31(1):65–95

Heston SF. 2005. *Linear Quadrupole Focusing for High Resolution Microdroplet-Based Fabrication*. http://d-scholarship.pitt.edu/9947/

Higuera FJ. 2003. Flow rate and electric current emitted by a taylor cone. *Journal of Fluid Mechanics*. 484:303–27

Hohman MM, Shin M, Rutledge G, Brenner MP. 2001. Electrospinning and electrically forced jets. i. stability theory. *Physics of Fluids (1994-present)*. 13(8):2201–20

Hong Y, Li Y, Yin Y, Li D, Zou G. 2008. Electrohydrodynamic atomization of quasi-monodisperse drug-loaded spherical/wrinkled microparticles. *Journal of Aerosol Science*. 39(6):525–36

Huebner AL, Chu HN. 1971. Instability and breakup of charged liquid jets. *Journal of Fluid Mechanics*. 49(02):361–72

Jaworek A. 2007a. Electrospray droplet sources for thin film deposition. *J Mater Sci*. 42(1):266–97

Jaworek A. 2007b. Micro- and nanoparticle production by electrospraying. *Powder Technology*. 176(1):18–35

Jr GCW. 2008. Capillary oscillations on liquid jets. *Journal of Applied Physics*. 51(7):3586–92

Kalaaji A, Lopez B, Attané P, Soucemarianadin A. 2003. Breakup length of forced liquid jets. *Physics of Fluids (1994-present)*. 15(9):2469–79

Keller JB, Rubinow SI, Tu YO. 2003. Spatial instability of a jet. *Physics of Fluids (1958-1988)*. 16(12):2052–55

Khan S, Doh YH, Khan A, Rahman A, Choi KH, Kim DS. 2011. Direct patterning and electrospray deposition through ehd for fabrication of printed thin film transistors. *Current Applied Physics*. 11(1, Supplement):S271–S279

Kim J-S, Chung W-S, Kim K, Kim DY, Paeng K-J, et al. 2010. Performance optimization of polymer solar cells using electrostatically sprayed photoactive layers. *Adv. Funct. Mater.* 20(20):3538–46

Kulkarni P, Baron PA, Willeke K. 2011. *Aerosol Measurement: Principles, Techniques, and Applications*. John Wiley & Sons. 904 pp.

Kyritsis DC, Coriton B, Faure F, Roychoudhury S, Gomez A. 2004. Optimization of a catalytic combustor using electrosprayed liquid hydrocarbons for mesoscale power generation. *Combustion and Flame*. 139(1–2):77–89

Lafrance P. 2008. Nonlinear breakup of a laminar liquid jet. *Physics of Fluids (1958-1988)*. 18(4):428–32

Lee D-Y, Shin Y-S, Park S-E, Yu T-U, Hwang J. 2007. Electrohydrodynamic printing of silver nanoparticles by using a focused nanocolloid jet. *Applied Physics Letters*. 90(8):081905–081905–3

Lee J, Basu S, Kumar R. 2013. Comparison and cross-validation of optical techniques in different swirl spray regimes. *Atomization and Sprays*. 23(8):697–724

Leib SJ, Goldstein ME. 1986. The generation of capillary instabilities on a liquid jet. *Journal of Fluid Mechanics*. 168:479–500

Lenses: basic optics. 2008. In *Applied Charged Particle Optics*, pp. 1–43. Springer Berlin Heidelberg

Lin SP, Reitz RD. 1998. Drop and spray formation from a liquid jet. *Annual Review of Fluid Mechanics*. 30(1):85–105

Lin SP, Webb RD. 1994. A branching liquid jet. *Physics of Fluids (1994-present)*. 6(8):2671–75

Lojewski B, Yang W, Duan H, Xu C, Deng W. 2013. Design, fabrication, and characterization of linear multiplexed electrospray atomizers micro-machined from metal and polymers. *Aerosol Science and Technology*. 47(2):146–52

Melcher JR, Taylor GI. 1969. Electrohydrodynamics: a review of the role of interfacial shear stresses. *Annual Review of Fluid Mechanics*. 1(1):111–46

Melcher, James R. *Field-coupled surface waves*. MIT-Pr., 1963.

Miesse CC. 1955. Correlation of experimental data on the disintegration of liquid jets. *Ind. Eng. Chem.* 47(9):1690–1701

Miles JW. 1959. On the generation of surface waves by shear flows part 3. kelvin-helmholtz instability. *Journal of Fluid Mechanics*. 6(04):583–98

Nayfeh AH. 2003. Nonlinear stability of a liquid jet. *Physics of Fluids (1958-1988)*. 13(4):841–47

Park J-U, Hardy M, Kang SJ, Barton K, Adair K, et al. 2007. High-resolution electrohydrodynamic jet printing. *Nat Mater*. 6(10):782–89

Parker GW. 2002. Electric field outside a parallel plate capacitor. *American Journal of Physics*. 70(5):502–7

Pimbley WT, Lee HC. 1977. Satellite droplet formation in a liquid jet. *IBM Journal of Research and Development*. 21(1):21–30

Plateau, J., 1849, Acad. Sci. Bruxelles Mem. 23. 5

Qian S-X, Snow JB, Tzeng H-M, Chang RK. 1986. Lasing droplets: highlighting the liquid-air interface by laser emission. *Science*. 231(4737):486–88

Rayleigh, Lord. 1882. Xx. on the equilibrium of liquid conducting masses charged with electricity. *Philosophical Magazine Series 5*. 14(87):184–86

Rayleigh, Lord, J.W.S., 1879. On the instability of jets. Proc. London Math. Soc. 10,4.

Reneker DH, Yarin AL, Zussman E, Xu H. 2007a. Electrospinning of nanofibers from polymer solutions and melts. In *Advances in Applied Mechanics*, ed Hassan Aref and Erik van der Giessen. Volume 41:43–346. Elsevier

Reneker DH, Yarin AL, Zussman E, Xu H. 2007b. Electrospinning of nanofibers from polymer solutions and melts. In *Advances in Applied Mechanics*, ed Hassan Aref and Erik van der Giessen. Volume 41:43–346. Elsevier

Sansdrap P, Moës AJ. 1993. Influence of manufacturing parameters on the size characteristics and the release profiles of nifedipine from poly(dl-lactide-co-glycolide) microspheres. *International Journal of Pharmaceutics*. 98(1–3):157–64

Saville DA. 2003. Stability of electrically charged viscous cylinders. *Physics of Fluids (1958-1988)*. 14(6):1095–99

Shimoda T, Morii K, Seki S, Kiguchi H. 2003. Inkjet printing of light-emitting polymer displays. *MRS Bulletin*. 28(11):821–27

Si T, Li F, Yin X-Y, Yin X-Z. 2009. Modes in flow focusing and instability of coaxial liquid–gas jets. *Journal of Fluid Mechanics*. 629:1–23

Smith JN, Flagan RC, Beauchamp JL. 2002. Droplet evaporation and discharge dynamics in electrospray ionization†. *J. Phys. Chem. A*. 106(42):9957–67

Sterling AM, Sleicher CA. 1975. The instability of capillary jets. *Journal of Fluid Mechanics*. 68(03):477–95

Su B, Choy KL. 2000a. Microstructure and properties of the cds thin films prepared by electrostatic spray assisted vapour deposition (esavd) method. *Thin Solid Films*. 359(2):160–64

Su B, Choy KL. 2000b. Microstructure and optical properties of cdse thin films by electrostatic assisted aerosol jet deposition method. *Journal of Materials Science Letters*. 19(20):1859–61

Tang K, Gomez A. 1994. On the structure of an electrostatic spray of monodisperse droplets. *Physics of Fluids (1994-present)*. 6(7):2317–32

Taylor G. 1964. Disintegration of water drops in an electric field. *Proc. R. Soc. Lond. A*. 280(1382):383–97

Tepper G, Kessick R, Pestov D. 2007. An electrospray-based, ozone-free air purification technology. *Journal of Applied Physics*. 102(11):113305

Uhrich KE, Cannizzaro SM, Langer RS, Shakesheff KM. 1999. Polymeric systems for controlled drug release. *Chem. Rev.* 99(11):3181–98

Vega EJ, Montanero JM, Herrada MA, Gañán-Calvo AM. 2010a. Global and local instability of flow focusing: the influence of the geometry. *Physics of Fluids (1994-present)*. 22(6):064105

Vega EJ, Montanero JM, Herrada MA, Gañán-Calvo AM. 2010b. Global and local instability of flow focusing: the influence of the geometry. *Physics of Fluids (1994-present)*. 22(6):064105

Wang DP. 1968. Finite amplitude effect on the stability of a jet of circular cross-section. *Journal of Fluid Mechanics*. 34(02):299–313

Wang DZ, Jayasinghe SN, Edirisinghe MJ. 2005. High resolution print-patterning of a nano-suspension. *J Nanopart Res*. 7(2-3):301–6

Weber, C., 1931, Z. Angew. Math. Mech. 11, 136.

Xu Q, Hashimoto M, Dang TT, Hoare T, Kohane DS, et al. 2009. Preparation of monodisperse biodegradable polymer microparticles using a microfluidic flow-focusing device for controlled drug delivery. *Small*. 5(13):1575–81

Yin Y-X, Xin S, Wan L-J, Li C-J, Guo Y-G. 2011. Electrospray synthesis of silicon/carbon nanoporous microspheres as improved anode materials for lithium-ion batteries. *J. Phys. Chem. C*. 115(29):14148–54

Yuen M-C. 1968. Non-linear capillary instability of a liquid jet. *Journal of Fluid Mechanics*. 33(01):151–63

Zhang Y, Wu L, Xie E, Duan H, Han W, Zhao J. 2009. A simple method to prepare uniform-size nanoparticle tio2 electrodes for dye-sensitized solar cells. *Journal of Power Sources*. 189(2):1256–63

Zhao X, Lojewski B, Yang W, Zhu T, Mi B, et al. 2012. Electrospray as a fabrication tool in organic photovoltaics. *Reviews in Nanoscience and Nanotechnology*. 1(3):172–86